The Study of Positive-Ion Mass Spectrometry of 5-Fluorouracil Using Low-Energy Electron Impact

Presented by

Michael A. Brown, B.Sc.

A thesis submitted for the degree of Masters of Science

Maynooth University
National University of Ireland Maynooth

Department of Experimental Physics
National University of Ireland Maynooth
Maynooth
Co. Kildare

Head of Department:

Professor J. Anthony Murphy

Research Supervisor:

Dr Peter J. M. van der Burgt

May 2018

Abstract

The aim of the experiment described within this thesis was to generate a molecular beam of 5-fluorouracil and to investigate the fragmentation processes that were induced by low-energy electron impact. The apparatus is contained in a vacuum chamber with three main compartments: the expansion chamber, the collision chamber and the flight-tube. The expansion chamber is where the molecular beam is produced by a resistively heated oven containing 5-fluorouracil powder. The molecular beam enters the collision chamber through a skimmer where it is crossed with a pulsed electron beam. The electron beam has a pulse width of 0.5 μs providing good time-of-flight resolution. Positive ions produced by electron collisions with the molecules are extracted into a reflectron time-of-flight mass spectrometer. The field-free region and the reflector of the time-of-flight mass spectrometer are both located in the flight-tube. The reflector is positioned at the end of the flight-tube and directs the ions back into the field-free region towards the detector. A multichannel scaler triggered synchronously with the electron pulse is used to accumulate time-of-flight spectra.

Using computer-controlled data acquisition, mass spectra were measured for electron impact energies from 5 eV - 100 eV in 0.25 eV steps. Ion yield curves for most fragment ions were determined by fitting groups of peaks in the mass spectra with sequences of normalised Gaussians. The appearance energies for these ions were determined by fitting onset functions to the ion yield curves. By comparing the mass spectra and the appearance energies with those of uracil, new information about fragmentation processes is obtained.

Acknowledgements

First of all, I would like to express my special appreciation and gratitude to my supervisor, Dr Peter J. M. van der Burgt, whose guidance and knowledge was invaluable to me throughout my research over the past two years. I would like to thank you for the time you have spent proof reading, what seemed to be, an infinite amount of draft copies of my thesis, it has been greatly appreciated. I wish to thank Dr Marcin Gradziel for his contribution to the LabVIEW programs that were used in this experiment.

I would also like to thank the head of the department, Professor J. Anthony Murphy and the rest of the Experimental Physics academic and technical staff, who have been incredibly kind in helping me whenever I needed it. A huge thank you must go to my office-mate Melissa, for the amazing company you brought every day, and for all the times you shared your food with me. To all of my fellow postgrads: thank you for making this masters a hugely enjoyable and memorable experience.

I want to thank my girlfriend Aoife, for the unwavering support and constant encouragement you have given me throughout my masters, and to Gavin, for pretending to listen to me whenever I would discuss my research with you. Finally, The biggest thank you of all goes to my Mam and Dad, who have been there for me and helped me throughout my six years in Maynooth University and continue to do so today, something I am very grateful for.

List of Figures

List of Tables

Contents

Chapter 1

Introduction

1.1 Why study electron collisions with 5-fluorouracil?

In recent years many studies of electron collisions with molecules have focused on biomolecules such as the nucleobases in the gas phase. Radiation induced processes in the DNA bases have been the focus of many studies, aiming at a better understanding of the fundamental reaction mechanisms leading to DNA strand breaks. When high-energy ionising radiation passes through biological tissue, a large amount of secondary electrons are produced along the tracks of the ionising radiation, mostly with energies below 30 eV, and these electrons are very effective in causing DNA strand breaks. Even electrons with energies below the ionisation energies of the DNA bases are capable of breaking bonds via dissociative electron attachment. For this reason, many recent studies have focused on collisions with DNA bases in the gas phase. Reviews of this field of molecular physics research are given by [Alizadeh et al., 2015], [Baccarelli et al., 2011b], [García Gómez-Tejedor and Fuss, 2012] and [Sanche, 2005].

Previous studies in Maynooth University have focused on electron impact fragmentation of the nucleobases of cytosine [van der Burgt, 2014], thymine [van der Burgt et al., 2014], adenine [van der Burgt et al., 2015] and uracil [Diskin, 2015]. These studies have been performed using time-of-flight mass spectrometry of the positive ions generated by electron impact fragmentation. The focus of the research presented in this thesis is 5-fluorouracil, (see Figure 1.1). The halo-uracils are important in radiation treatment therapy as radiosensitizers, because cancer tissues doped with these sensitizer molecules will be destroyed preferentially under exposure to ionising radiation. Because secondary

electrons play an important role in radiation damage processes on the molecular scale, low-energy electron impact studies of radiosensitizers are of relevance.

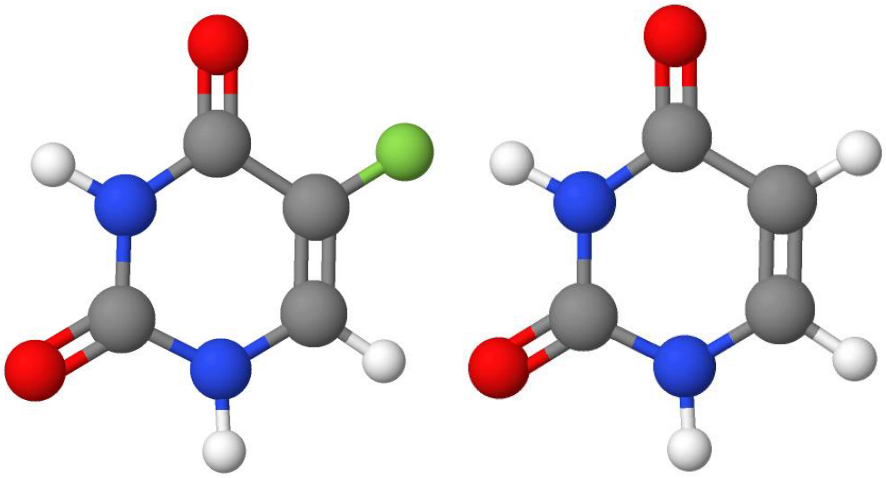

Figure 1.1: The 5-fluorouracil and uracil molecules.

The chemical formula for 5-fluorouracil and uracil are $C_4H_3FN_2O_2$ and $C_4H_4N_2O_2$, with a mass number of 130 u and 112 u respectively. The structure of the 5-fluorouracil molecule can be seen in Figure 1.1. The purpose of this thesis is to present new results for low-energy electron impact to 5-fluorouracil in the gas phase leading to the formation of positively charged fragments. We have obtained ion yield curves and appearance energies for most of the positively charged fragments. These results are compared with other research on uracil and the 5-halo-uracils, and provide new information about the appearance energies of the positive fragments and the fragmentation pathways initiated by electron impact.

In the following sections we briefly review the structure of DNA and RNA, the collision processes involving biomolecules, and research that has been performed on the halo-uracils.

1.2 Structure of DNA and RNA

DNA is composed of two poly-nucleotide chains that form the shape of a double helix. Each nucleotide consists of a phosphate group, a sugar and a heterocyclic base. The backbone of DNA is made up from alternating phosphate units and the sugar 2-deoxy-D-

ribose, with nucleobases connected via the glycosidic C-N bond, [Baccarelli et al., 2011a]. There are four heterocyclic bases: thymine (T), adenine (A), cytosine (C) and guanine (G) that each connect to the DNA backbone, see Figure 1.3. These bases attach to the backbones in pairs. Adenine and thymine form one base pair, with cytosine and guanine forming the second base pair.

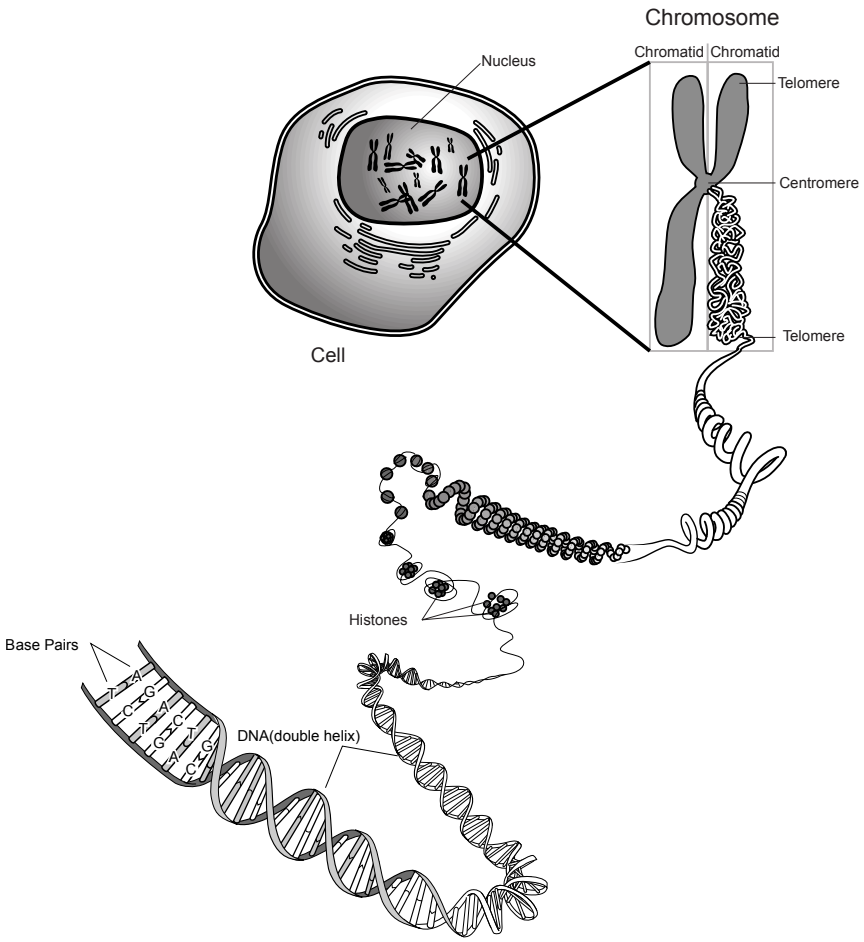

Figure 1.2: The structure of a biological cell, [National Human Genome Research Institute].

The two backbone chains of DNA are held together through hydrogen bonding between the base pairs. RNA differs from DNA in their molecular structure. While DNA has two strands, RNA consists of a single strand. The RNA molecule does not contain thymine bases; instead they are replaced by uracil (U). RNA does not form a double helix, but 3-dimensional structures - similar to that of DNA - are formed by base pairing. The base

pairs in RNA include: uracil pairing with adenine, and guanine pairing with cytosine.

The interchangeability of thymine with both uracil and 5-fluorouracil allow research groups to investigate the radiation induced fragmentation processes of modified DNA, which will result in the enhancement on radiosensitization techniques, briefly discussed later in this chapter. Prior to this discussion, I will introduce the effects that high-energy radiation has on biomolecules, primarily focussing on DNA molecules, and introduce the secondary species produced from this interaction.

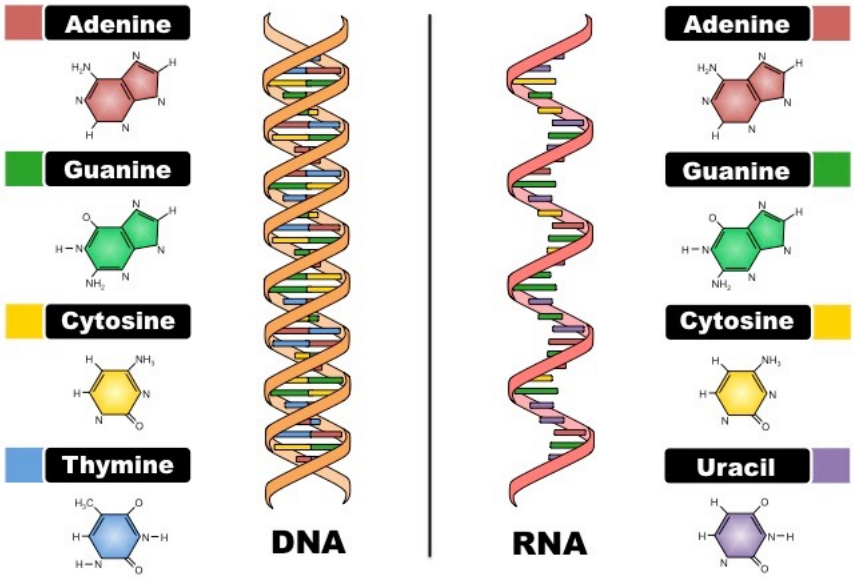

Figure 1.3: The structure of DNA compared with the structure of RNA, [Bio].

1.3 Electron - molecule collisions

1.3.1 Introduction

The following section begins with a summary of the resulting affects from the interaction of high-energy radiation with biomolecules by mentioning the devastating affects it causes (primarily how it interacts with DNA). The importance of researching this interaction is apparent as it supplies information regarding the dissociative processes that cause chemical and structural modification of DNA molecules (single- and double-strand breaks) which are prevalent is radiotherapy.

In recent years there has been a lot of research regarding the interaction of high-energy radiation with biomolecules, primarily DNA. DNA is the genetic material, most sensitive to radiation damage. When high-energy radiation interacts with DNA molecules, it can result in damage to the genome which generally leads to cell death. This is why high-energy radiation is used in radiotherapy, to interact with and kill cancerous cells. However, exposure to ionising radiation can cause irreversible damage to living tissue, and can result in mutation, radiation sickness, cancer, and death (see [Alizadeh et al., 2015], [Baccarelli et al., 2011b], [García Gómez-Tejedor and Fuss, 2012], [Sanche, 2005]).

Section 1.3.2 will discuss the processes behind electron induced ionisation. Understanding how the resulting secondary species are produced will give insight into how they act under various conditions, see Section 1.3.3. In addition, I will discuss how electron - molecule interactions can induce internal structure modifications of the atoms and molecules involved. Potential energy wells are presented to show the position at which fragmentation occurs within the molecule as the electron energy increases.

1.3.2 Principles of electron induced ionisation

This section will discuss the principles of electron induced ionisation and dissociation. The ionisation energy can be defined as the amount of energy that an atom needs to absorb in its vibrational and electronic ground states in order to discharge an electron to form an ion, [Ball et al., 2012]. High-energy radiation is composed of particles that individually carry enough kinetic energy to liberate an electron from an atom or molecule, ionizing it. If the electron energy is sufficiently high, there is a probability that doubly charged ions may be formed.

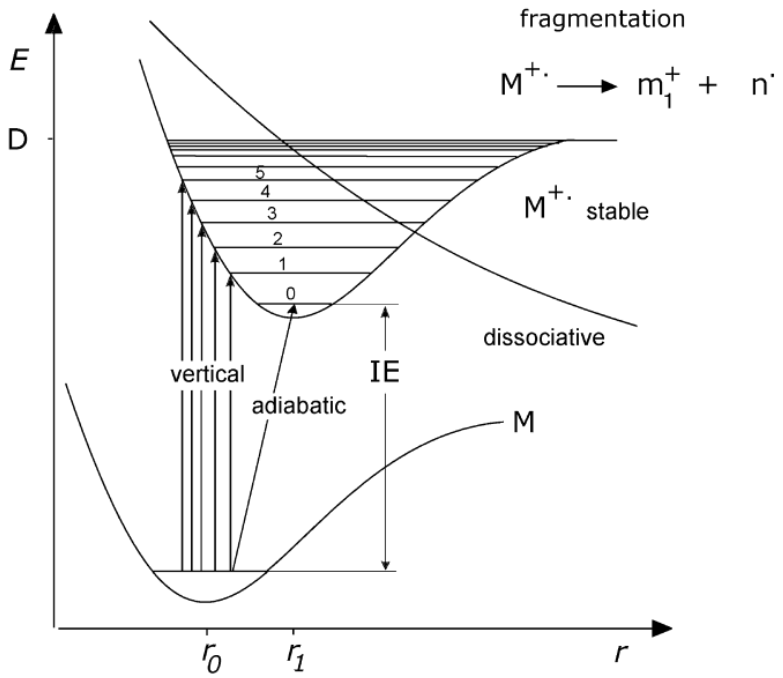

Figure 1.4: A graph showing the transition from a neutral to an excited state for a diatomic molecule, [Gross and Roepstorff, 2011].

When an electron interacts with a molecule, the molecules electronic excitation occurs much faster than the time is takes for the bond lengths of the molecule to find their new position of equilibrium, also known as the *Franck-Condon principle*, [Gross and Roepstorff, 2011].

Figure 1.4 shows that the minimum of the potential energy curve of molecule M, is located at the shorter bond length r_0, whereas the minimum of the potential energy curve for M^{+*} is located at a longer bond length, given as r_1. Figure 1.4 also shows the vertical transition of molecule M into an excited state M^{+*}. Two excited M^{+*} ions are shown, one with an internal energy below the dissociation energy (this ion will remain stable), and the second with an internal energy greater than the dissociation energy (this ion is unstable). If the internal energy of the ion is greater than the dissociation energy D, fragmentation of molecule $M^{+*} \rightarrow m_1^+ + n^*$ will occur. Moreover, if a resulting fragment formed by dissociation possesses enough internal energy, a second dissociation can occur, forming additional products, see Figure 1.5.

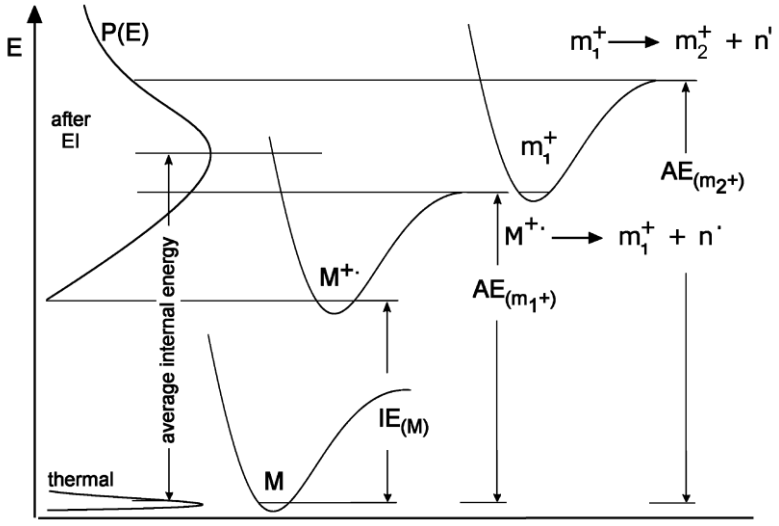

Figure 1.5: This Figure shows the change in a molecules internal energy P(E) upon electron ionisation, the potential energy curves for various fragments, and defines the appearance energy (AE) of subsequent fragmentations, [Gross and Roepstorff, 2011].

Figure 1.5 shows the location of subsequent fragmentations caused by electron induced ionisation, and thus shows the position of their corresponding appearance energy. Three potential energy curves are shown for molecules M, M^{+*} and m_1^+ where M is a neutral molecule, M^{+*} is the excited ion caused by electron ionisation of M, and m_1^+ is a resulting fragment formed due to the dissociation of excited molecule M^{+*}. It should also be noted that the ions are not produced with a single internal energy value that applies for every ion, but with a broad energy distribution, given by P(E) in Figure 1.5.

When an ion dissociates into fragments, the lowest energy at which this occurs is known as the *appearance energy*. Figure 1.5 shows the positions of appearance energies $AE_{(m_1^+)}$ and $AE_{(m_2^+)}$ for fragments m_1^+ and m_2^+. Each of these resulting fragments will appear as a peak on a mass spectrum.

For this experiment, the appearance energies for various fragments of 5-fluorouracil were determined. Figure 1.6 shows the time scale of events regarding various electron ionisation processes.

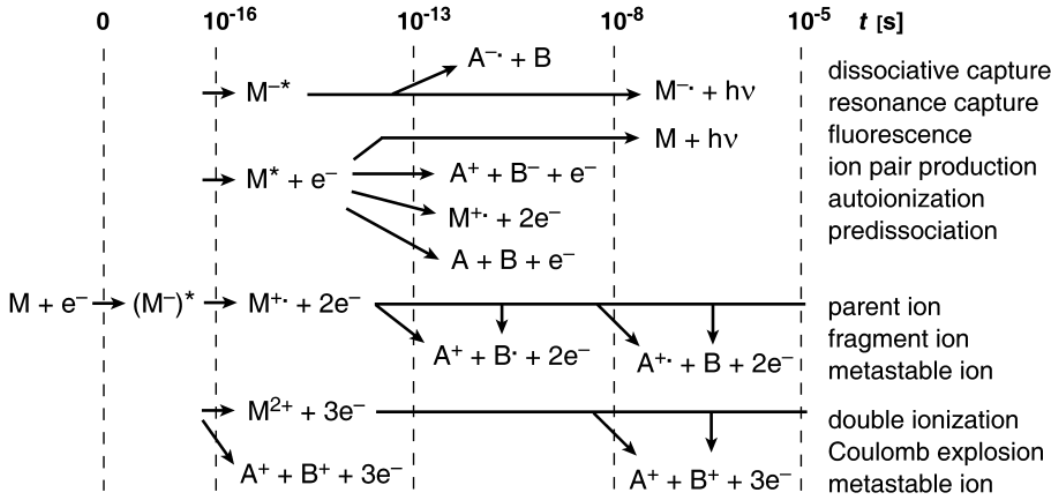

Figure 1.6: Time scale of events for various electron ionisation processes, [Gross and Roepstorff, 2011].

1.3.3 The role of low-energy electrons in radiation damage processes

Ionisation can lead to molecular bond breaking through a number of processes discussed below. When ionising radiation passes through a cell, it releases its energy along its track by interacting with the electrons of nearby molecules. The probability of ionisation and excitation from a collision are similar, but a larger amount of the energy flows into ionisation, [Sanche, 2005]. The released energy is absorbed by molecules near the track, resulting in excitation, ionisation, the formation of radicals, and the generation of low-energy secondary electrons. For reviews see [Balog et al., 2004], [Hotop et al., 2004] and [McConkey et al., 2008]. The processes are listed on the following page.

Ionisation and dissociation:

$$e + M \longrightarrow M^+ + e + e_{sc}$$

$$e + M \longrightarrow X^+ + Y + e + e_{sc}$$

$$e + M \longrightarrow X^+ + Y^+ + 2e + e_{sc}$$

Excitation and dissociation:

$$e + M \longrightarrow M^* + e_{sc} \longrightarrow M + e_{sc} + hv$$

$$e + M \longrightarrow M^* + e_{sc} \longrightarrow X + Y + e_{sc}$$

$$e + M \longrightarrow M^* + e_{sc} \longrightarrow X^* + Y \longrightarrow X + Y + e_{sc} + hv$$

$$e + M \longrightarrow M^* + e_{sc} \longrightarrow X^+ + Y + e + e_{sc}$$

Dissociative electron attachment:

$$e + M \longrightarrow M^{-*} \longrightarrow X + Y + e$$

$$e + M \longrightarrow M^{-*} \longrightarrow X^- + Y$$

where M is a molecule, X and Y are atoms or groups of atoms, e represents an electron, and e_{sc} represents a scattered electron. Dissociation mechanisms are of vital importance to radiotherapy research as the risks involved with irradiating biomolecules with high-energy radiation are great, therefore a clear understanding of the mechanisms involved in these interactions is needed.

The following paragraph will briefly discuss the dissociative electron attachment (DEA) process that induces single- and double-strand breaks in DNA. A more thorough discussion is found in Section 1.5.1 where the results obtained by various research groups with regard to the dissociative electron attachment process on 5-halo-uracils are presented.

Dissociative electron attachment (DEA) refers to the process of a low-energy free electron attaching itself to a molecule, causing it to eventually fragment itself - through an understood process described below. Equation 1.1 depicts a simple representation of this process that can be modelled with molecules A and B, and low-energy electron e^-:

$$AB + e^- \longrightarrow AB^{-*} \longrightarrow A + B^- \textit{ or } A^- + B \tag{1.1}$$

where AB^{-*} is a super-excited molecule that is transitioned into a higher energy state but does not exceed the excited state potential curve that would cause dissociation. Instead, the super-excited molecule AB^{-*} is brought into a vibrational state with the same energetic make-up of a repulsive state, meaning that AB^{-*} will spontaneously decay. Dissociation occurs by tunnelling to a repulsive electronic state when the excited vibrational state matches that of a repulsive state. Section 1.5.1 deals with the results obtained from different research groups into how various halo-uracil molecules fragment due to dissociative electron attachment.

As mentioned, when high-energy radiation interacts with biological tissue it can produce severe chemical and structural modifications that can affect biological function, [García Gómez-Tejedor and Fuss, 2012]. DNA molecules can be damaged by means of either direct or indirect interaction with high-energy radiation. In the case of direct interaction, the radiation causes damage as it collides and deposits energy to the DNA molecules directly. An indirect interaction refers to a high-energy particle colliding with the biomolecules that surround the DNA (e.g. water, protein and oxygen molecules), which then produce the secondary species that damage the DNA molecules, [Desouky and Zhou, 2016].

Low-energy secondary electrons are the most abundant product produced with $\approx$ 5 x 10^4 being produced per megaelectron volt of deposited energy within nanoscopic volumes along ionization tracks, [Alizadeh et al., 2015]. Secondary electrons possess most of the kinetic energy of the incident radiation and are the secondary species that inflict the most damage to biomolecules, [Sanche et al., 2000]. These electrons can cause single- and double-strand breaks in DNA even if their energy is below the ionisation energy, through processes such as dissociative electron attachment. Other secondary products include: super-excited molecules, ions (cations and anions), and radicals. Ions and radicals that are formed can trigger further damage through energy deposition to surrounding molecules. Sanche et al. [2000] discovered that low-energy electrons can induce single- and double-strand breaks in DNA due to the secondary species that are generated by the incident high-energy radiation, discussed below.

The paper that birthed this field of research was published in the year 2000 and was titled '*Resonant Formation of DNA Strand Breaks by Low-Energy (3 to 20 eV) Electrons*' by Sanche et al. [2000]. They discovered that low-energy secondary electrons can induce single- and double-strand breaks in DNA. Prior to this finding, it was thought that the harmful effects of ionising radiation in living cells was caused by direct impact of the high-energy particles.

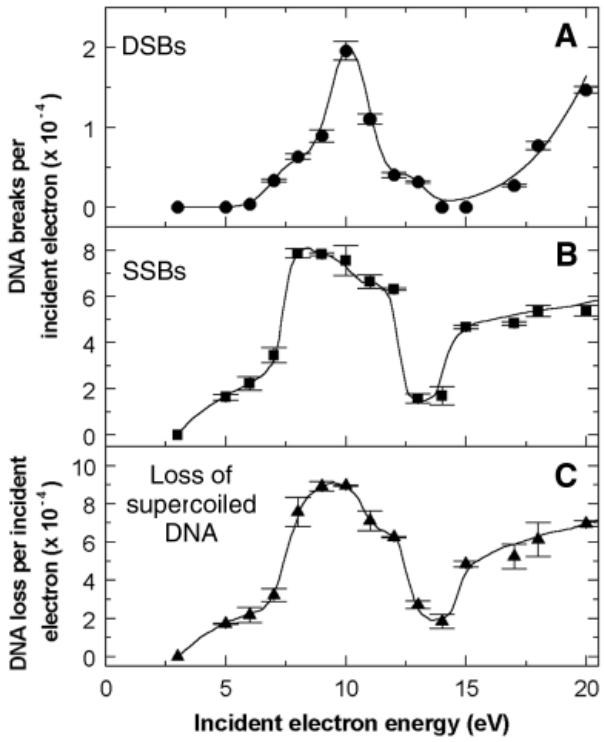

Figure 1.7: Induced single- and double-strand breakage in DNA with increasing electron energy (3 - 20 eV), [Sanche, 2005].

Figure 1.7 shows that single-strand breaks and double-strand breaks can be induced in DNA by electron energies below the ionisation threshold of DNA. It was shown that the high yield of single-strand breaks and double-strand breaks is caused by electron attachment to a molecule within the DNA. This induces bond rupture which initiates the resulting fragmentation processes.

The structural modifications caused by single- and double-strand breaks can result in errors in their repair resulting in gene mutations and alterations in the chromosome. Chromosomes are responsible for the reproduction of each cell, and if one cell is damaged (single- and double-strand breaks), this can result in the reproduction of damaged cells.

1.4 The role of low-energy electrons in radiosensitization and radiation therapy

1.4.1 Background

The use of radiation to treat cancer patients had been around since the early twentieth century. In 1901, a German physicist Wilhelm Conrad Roentgen was awarded the Nobel Price for his work, using x-rays as a diagnostic tool. Back then, radiation therapy began with the use of radium and diagnostic machines with low voltage. It is well known that most of the advances made in curing cancer in recent times, have been due to successful combination of chemotherapy doses with radiation therapy.

Further improvement in radiation therapy will depend greatly on understanding the underlying mechanisms of single- and double-strand breaks in DNA caused by the interaction of secondary species such as low-energy secondary electrons (produced by the interaction of high-energy radiation with biomolecules), with DNA molecules.

Low-energy electrons play a vital role in radio-biology research including techniques to improve radiosensitization with the use of molecules such as 5-fluorouracil. A useful attribute of low-energy electrons is their short range penetrability within biological tissue. Having a short range of penetration means that the damage induced by the secondary electrons is confined to a few biomolecules (e.g., to the DNA of cancer cells, nearby water and proteins), [García Gómez-Tejedor and Fuss, 2012].

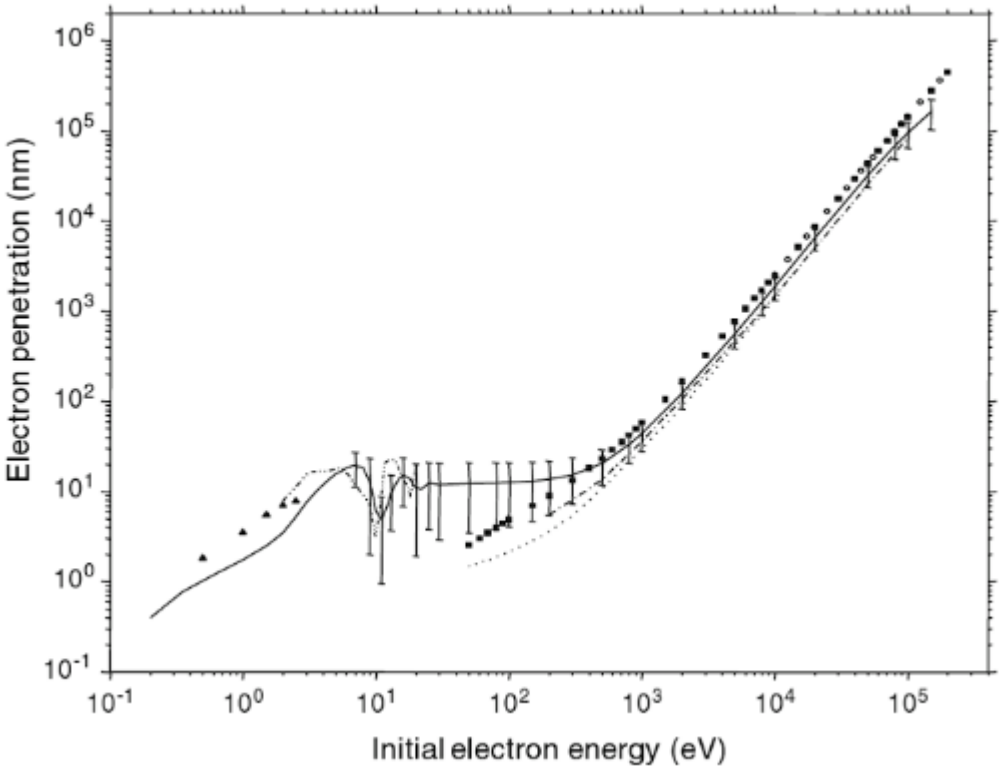

Figure 1.8: The penetrability of electrons in 25°C liquid water as a function of initial electron energy, [García Gómez-Tejedor and Fuss, 2012].

Figure 1.8 shows the penetrability of electrons in 25°C liquid water as a function of initial electron energy. The depth of penetration from electrons with an energy between 0 - 30 eV is of the order of 10 nm in H_2O and DNA. Electrons with this energy are very efficient in causing single- and double-strand breaks.

Denifl et al. [2003] conducted studies on electron attachment to 5-chloro-uracil. Electron attachment initiates a dissociation process that cause single- and double-strand breaks in DNA, discussed in more detail in Section 1.5.1. Figure 1.9 shows the relationship between incident electrons of varying energy and the abundance of single-strand breaks and double-strand breaks induced in DNA.

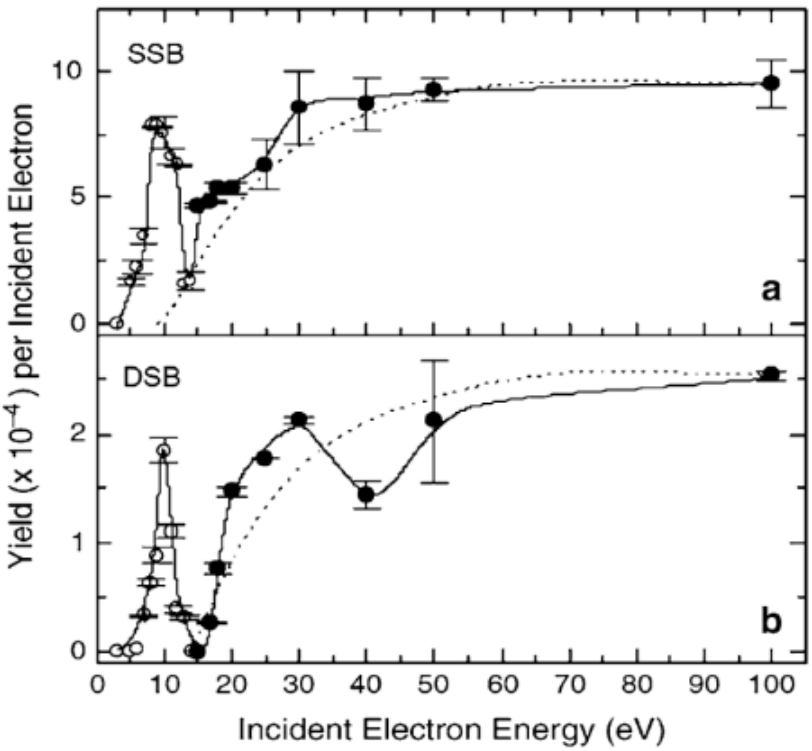

Figure 1.9: The yield of single-strand breaks (SSB) and double-strand breaks (DSB) with an increase of incident electron energy, [García Gómez-Tejedor and Fuss, 2012].

Figure 1.9 shows the single- and double-strand break yield as a function of 0 - 100 eV electron impact. It can be seen that electrons with energies as little as 10 eV are very efficient at causing single- and double-strand breaks in DNA. The electrons with an energy of 10 eV carry almost the same probability as the 100 eV electrons when it comes to breaking DNA strands. Researchers have utilised low-energy electrons in radiosensitization due to low-energy electrons having only a small range of penetrability within biological tissue. This fact, coupled with the ability to cause single- and double-strand breaks in DNA, make low-energy electrons effective at disrupting and killing dangerous cells. Suppose there exists a location where there are numerous cancer cells within a human body. Electrons with an energy range of 1 - 30 eV which have short penetrability, can be used to confine the damage sites they create to a few biomolecules (i.e. targeting the cancerous cells without inflicting damage on surrounding healthy cells).

There are different techniques used to enhance radiosensitization. One method is to increase the number of low-energy electrons surrounding the targeted DNA, [García Gómez-Tejedor and Fuss, 2012]. Gold nanoparticles (GNP) are used to increase the

absorption of ionising radiation which will result in a higher production of low-energy secondary electrons. Seeing as low-energy secondary electrons have a short range of penetrability and are produced in large amounts during ionisation, GNP's have the potential to focus radiation energy to the dangerous cancer cells, [Xiao et al., 2011]. The results obtained from Xiao et al. [2011] provide additional evidence that low-energy electrons enhance radiosensitization of DNA using GNP's.

A second method to enhance radiosensitization involves making the targeted DNA more susceptible to low-energy electrons with the use of radiosensitizers. 5-fluorouracil is a molecule that is used to enhance radiosensitization and is the molecule investigated in this experiment. It increases the effectiveness of radiation treatment which is discussed in Section 1.4.2. The development of chemo-radiation therapy techniques is a very important field of research that is attempting to improve the efficiency of current cancer treatments. As mentioned above, the main advances in cancer treatment have come from successfully combining chemotherapy agents with radiation therapy. The simultaneous use of chemotherapy and radiotherapy means that lower doses of chemotherapy may be used on a patient making it a safer alternative, [Ferreira da Silva et al., 2011].

1.4.2 5-fluorouracil and its role as a radiosensitizer

5-fluorouracil is capable of increasing radiation sensitivity through the killing of cells that are in their S-phase, as these cells are radio-resistant, thus increasing the rate of cell death in tumours. The S-phase period of a cells cycle is when the DNA is replicated. The onset of DNA replication marks a cells entry into S-phase, [Stein and Pardee, 2004]. Accurate DNA replication is important for the cells survival, as it prevents any harmful genetic abnormalities that could lead to cell death.

Research into the fragmentation processes of 5-fluorouracil, as well as other 5-halouracils, is becoming more widespread due to the potential of 5-fluorouracil as a radiosensitizer. The halogen atom in the 5-halo-uracils replaces the methyl group in thymine, and replaces the corresponding hydrogen atom in uracil (see Figure 1.1). Because of their structural similarities, 5-halo-uracil can be substituted for thymine in DNA in vivo, and be substituted for uracil in RNA in vivo. Cells that contain modified halo-uracil DNA are significantly more sensitive to ionisation radiation,[Abdoul-Carime et al., 2003]. The

study of the fragmentation processes of 5-fluorouracil and the other halo-uracils therefore provides relevant information about the radiation damage mechanisms happening within radiosensitized cells.

1.5 Experimental research of low-energy electron impact with 5-halo-uracils (and uracil)

1.5.1 Dissociative electron attachment (DEA) studies

This section discusses the measurements recorded by various research groups, regarding dissociation by DEA with 5-halo-uracils and uracil. Abdoul-Carime et al. [2003] published their research findings for the formation of negative ions from gas phase halo-uracils by low-energy electron impact, using a standard crossed beam apparatus. The ion yield for fragments of various halo-uracils, including 5-fluorouracil can be seen in Figure 1.10.

Abdoul-Carime et al. [2003] propose that the presence alone of a halo-uracil in DNA is not the entire picture regarding the sensitization of the halo-uracil modified DNA. Rather, the location of the halo-uracil within the DNA is also of great importance. When the free secondary electrons surround the halo-uracil molecules within the DNA, the probability of them interacting increases, which will cause the decomposition process to begin.

Figure 1.10 shows the yield from various fragments of 5-fluorouracil being produced from electron impact energies below their ionisation energy. In this scenario, the electron impact energy refers to the energy associated with a beam of electrons that interact with the molecules. The electron impact energy required to produce the parent ion (the initially ionised molecule before subsequent fragmentations) of 5-fluorouracil, through dissociative electron attachment, was 0.1 ± 0.2 eV, 0.7 ± 0.2 eV and 1.8 ± 0.2 eV (clear peaks in the ion yield graph). It was concluded that these fragmentations were generated by dissociative electron attachment. Halo-uracils are quite susceptible to this process, as they have a large dipole moment increasing the chance of a low-energy electron getting trapped by the multipolar forcefield.

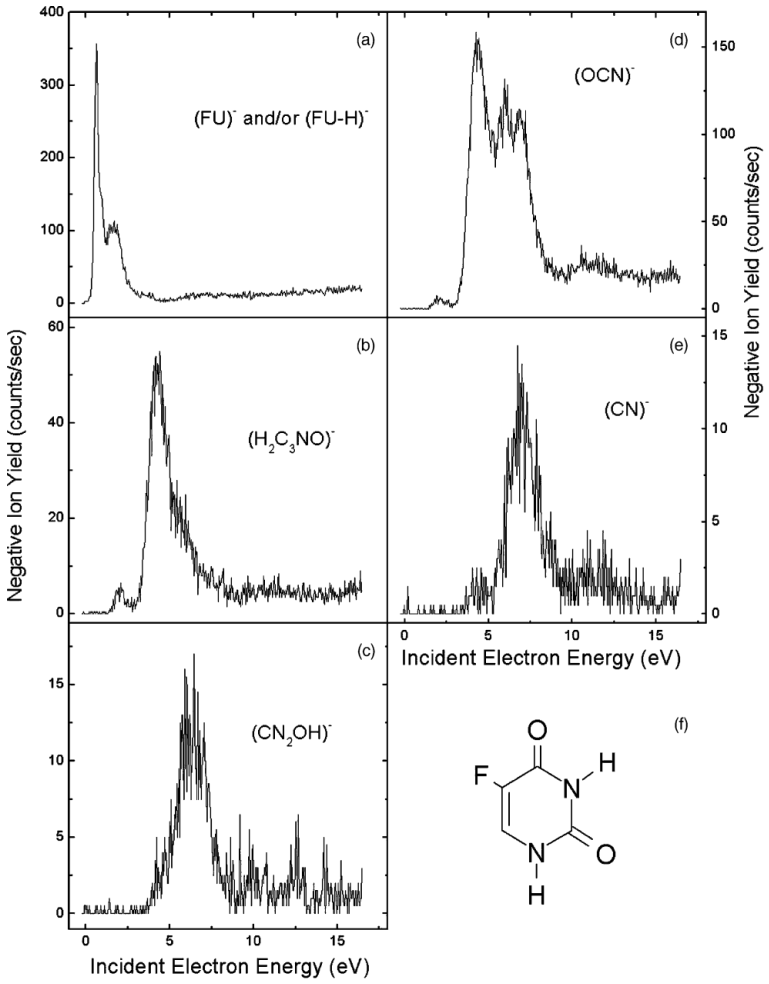

Figure 1.10: These results are taken from Abdoul-Carime et al. [2003] and show the electron energy dependence for the ion yields of a) 5-FU$^-$ and/or (5-FU - H)$^-$, (b) $H_2C_3NO^-$, (c) CN_2OH^-, (d) OCN^-, and (e) CN^-. These results were produced by electron impact to gaseous 5-fluorouracil.

Another example of this research was carried out by Denifl et al. [2003], who investigated the effects of electron attachment and dissociative electron attachment to 5-chlorouracil in the gas phase. A hemispherical electron monochromator (including a quadrupole mass spectrometer) was used, which enabled an electron energy resolution of between 90 - 120 meV. Very similar to the study discussed above, the electron impact energy required to produce the parent ion, this time the parent ion of 5-chlorouracil, was well below the ionisation energy.

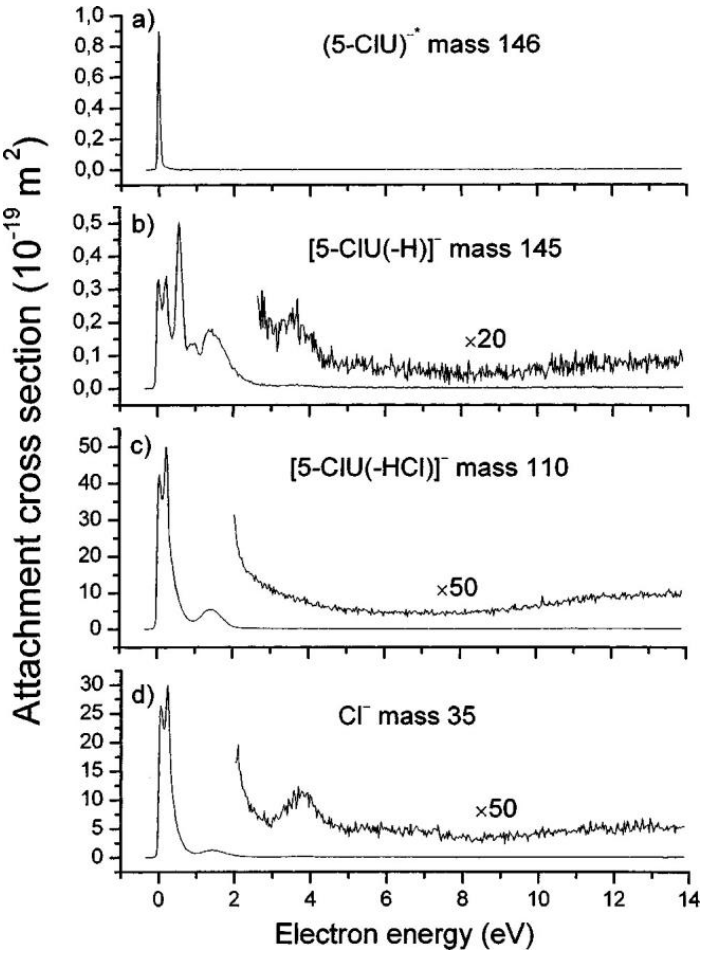

Figure 1.11: Absolute cross section function for the DEA to 5-ClU, [Denifl et al., 2003].

Figure 1.11 shows the attachment cross sections for various masses with low electron impact energy. The parent ion, $(5\text{-ClU})^-$ (146 u) had a resonant electron voltage of 0 eV which agrees well with the 0.1 ± 0.2 result obtained for the $(5\text{-FU})^-$. Fragments $(5\text{-ClU(-H)})^-$ (145 u) that underwent hydrogen loss, $(5\text{-ClU(-HCl)})^-$ (110 u) that underwent hydrogen and chlorine loss, and $(\text{Cl})^-$ (35 u) were generated at an electron impact energy of 0.57 eV, 0.23 eV and 0.23 eV respectively.

Abouafa and Dunet [2005] investigated the structures in dissociative electron attachment cross-sections in thymine, uracil and halo-uracils. The apparatus used for their experiment was an electrostatic electron spectrometer using two hemispherical energy analysers. The

(5-FU - H)$^-$ fragment occurred initially at an energy of 0.560 eV and was then found to appear at 0.85 eV and 1.28 eV. Their result for the 5-ClU$^-$ was found to be 0.00 eV. This agrees with the results found by Denifl et al. [2003], see Figure 1.11.

Abdoul-Carime et al. [2000] reported dissociative electron attachment to gaseous 5-bromouracil with a 0 - 16 eV incident electron energy range. They found that low-energy electron impact can produce various anion fragments that are caused from endo- and exo-cyclic bond ruptures. The parent ion BrU$^-$ resulted from resonant electron capture by the parent molecule at 0, 0.5 and 1.3 eV, [Abdoul-Carime et al., 2000]. The yield peaks for the Br$^-$ or (U-yl)$^-$ (U-yl referring to an anion fragment existing through exo-cyclic bond rupture) fragments were found to exist at 0, 1.4 and a weak structure at 6 eV. These results indicate that they were formed through dissociate electron attachment.

Abouaf et al. [2003a] compared the negative ion production processes in thymine (T) and 5-bromouracil (BrU) after impact of low-energy electrons (0-2 eV). The experimental apparatus used in this research included an electrostatic electron spectrometer using hemispherical energy analysers in tandem. The cross-section for the BrU$^-$ fragment displayed a peak located at 0.02 $\pm$ 0.02 eV alongside a smaller peak located at 0.6 eV. Regarding the Br$^-$ and Uyl$^-$ fragments, they observed three peaks close to 0 eV. These peaks were located at 0.02 $\pm$ 0.02, 0.09 $\pm$ 0.02 and 0.28 $\pm$ 0.02 eV. They concluded their study by verifying large cross-sections for negative ion production close to 0 eV in bromouracil.

Denifl et al. [2004a] investigated the process of electron attachment to chlorouracil, comparing the results of 5-chlorouracil with 6-chlorouracil. The experiment was carried out using a crossed electron/molecular beam apparatus. They found that the most dominant DEA channel is the formation of (M-HCl)$^-$ - which implies the loss of a neutral HCl molecule. (Note that M refers to ClU.) The reaction cross-sections are 9 x 10^{-18} m^2 and 5 x 10^{-18} m^2 for 6-chlorouracil and 5-chlorouracil respectively.

Scheer et al. [2004] describe the dipole bound and valence anion states in these compounds and present assignments for the two types of structure appearing in the cross-sections.

Winstead and McKoy [2006] studied low-energy electron collisions with gas-phase

uracil in the attempt to understand the resonant structure of the scattering cross section. They calculated the first resonance to appear at 0.32 eV which agrees relatively well with 0.22 eV, which is the result obtained from electron-transmission experiments. Their symmetry-resolved results for elastic scattering provide locations for the expected π^* shape resonances as well as indicating the possibility of a low-energy σ^* resonance.

1.5.2 Other electron impact studies

Many recent studies have focussed on low-energy electron collisions with the nucleobases (adenine, cytosine, guanine, thymine and uracil) in the gas phase. This section discusses the measurements recorded by various research groups, regarding electron impact with 5-halo-uracils and uracil.

Herve du Penhoat et al. [2004] studied the anion fragment formation in 5-halo-uracil (5-XU, U = uracil, X = fluorine, chlorine, bromine, and iodine) films induced by 1 - 20 eV electron impact. A heated oven raised each compound to a temperature below the evaporation onset temperature. Each 5-halo-uracil was raised to a different temperature (103 ° C for 5-fluorouracil). The electron gun operated with an energy range of 1 - 40 eV. A quadrupole mass spectrometer was used to measure the yield of fragments produced from the condensed phase target molecules.

	5-FU		5-ClU		5-BrU		5-IU	
anion	E_0^{onset}	E_0^{max}	E_0^{onset}	E_0^{max}	E_0^{onset}	E_0^{max}	E_0^{onset}	E_0^{max}
H^-	4.9	7.7	4.9	8.9	4.7	8.6	5.0	8.5
X^-	4.7	7.2	3.0	7.2	3.3	6.4	3.0	5.7
	(3.5)		(2.0)		(2.3)			
		12.1		8.7				
CN^-	5.0	8.4	5.0	8.4	5.6	8.3	5.2	8.4
	(4.6)				(4.8)		(4.4)	
OCN^-	4.0	8.7	4.0	9.1	5.3	8.7	4.3	8.8
					(4.7)			
O^-	-	-	-	-	-	-	5.8	8.1*
								12.3
OH^-	-	-	-	-	-	-	5.0	8.2
								12.2

Figure 1.12: Onset energies and positions of maxima (eV $\pm$ 0.5 eV) of yields produced by low-energy electron bombardment, [Herve du Penhoat et al., 2004]. X refers to the chemically related halogen elements.

Figure 1.12 is a table of results that show the onset energies for various 5-halo-uracils fragments. The onset energy for the halogen atom fragment of 5-ClU, 5-BrU and 5-IU was 3.0 ± 0.5, 3.3 ± 0.5 and 3.0 ± 0.5 eV respectively, while the halogen atom fragment of 5-FU (fluorine) had a larger onset energy of 4.7 ± 0.5 eV. Their studies found that ions H^- and X^- fragments were most abundant for all 5-halo-uracils.

Denifl et al. [2004b] determined the appearance energy of fragments produced through electron impact ionisation of 5- and 6-chlorouracil. The apparatus used in their experiment was a hemispherical electron monochromator coupled with a quadrupole mass spectrometer. An oven was heated to temperatures of 180°C and 160°C for 5-chlorouracil and 6-chlorouracil respectively. The appearance energies were determined by fitting a threshold function to the ion yield curves (for more details see Section 4.6.2). Mass spectra were recorded with an electron impact energy of 70 eV.

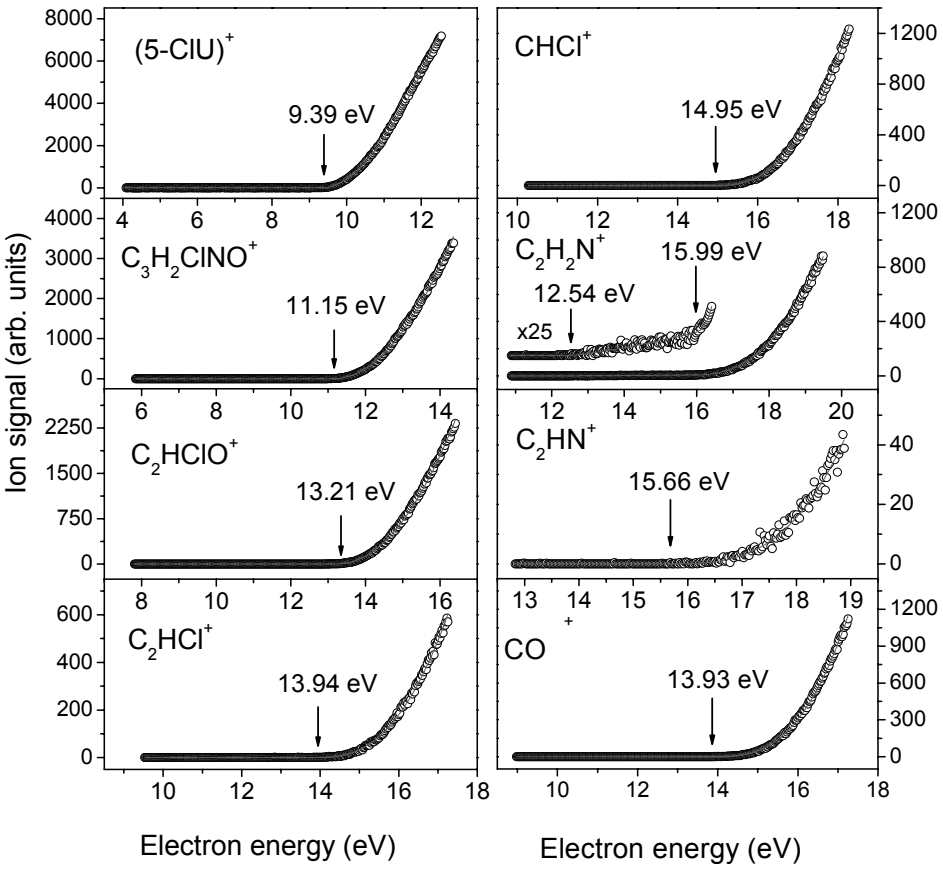

Figure 1.13: Appearance energy graphs for chosen fragments generated from neutral 5-chlorouracil by electron impact, [Denifl et al., 2004b].

The ionisation energy for 5-chlorouracil was determined to be 9.39 ± 0.05 eV. The most

abundant fragment in the mass spectrum was the $(C_3H_2ClNO)^+$ which had an appearance energy of 11.12 $\pm$ 0.03 eV. Denifl et al. [2004b] compared the appearance energies for all 5-halo-uracil molecules with that of thymine. All the compared appearance energies were within $\approx$ 0.5 eV of one another.

Denifl et al. [2004c] studied the threshold electron impact ionisation of uracil using a high resolution hemispherical electron monochromator combined with a quadrupole mass spectrometer. Mass spectra were recorded at an electron impact energy of 70 eV. The appearance energies were determined using a non-linear least square fitting procedure based on a Wannier type power law. The ionisation energy of uracil was found to be 9.59 $\pm$ 0.08 eV.

Abouaf et al. [2003b] investigated the excitation of the lowest electronic and vibrational excitation in gas phase thymine and 5-bromouracil by electron impact. The apparatus that was used for this research was an electrostatic electron spectrometer that used two hemispherical energy analysers, both in the electron gun and the analyser sections. Resonant vibrational excitation for both thymine and 5-bromouracil appeared in the 1 - 2 eV range as well as in the 4 - 5 eV range. There is an indication that they detected a triplet electronic state for both thymine at 3.6 $\pm$ 0.08 eV and 5-bromouracil at 3.35 $\pm$ 0.8 eV. Abouaf et al. [2003b] state that electronic and vibrational excitations do not appear to be involved in explaining the different behaviour of these molecules under ionising radiation.

Imhoff et al. [2007] investigated the formation channels and chemical composition of charged fragments of uracil (U) and 5-bromouracil (BrU) produced by 70 eV electron impact in gas phase and 10 - 200 eV Ar^* ion irradiation in condensed phase are investigated in parallel with that of thymine (T). The apparatus used in this research consisted of an ion beam system and a quadrupole mass spectrometer. They found that the fragmentation pattern of 5-bromouracil is quite different when compared with that of thymine and uracil with a lot less heavy fragments. Major anion fragments were produced by ion irradiation and they included H^-, O^-, CN^- and OCN^-. These fragments were the major ion fragments produced by ion irradiation for all three molecules.

Ulrich et al. [1969] conducted a study on the fragmentation processes of uracil (U) and thymine (T) derivatives. Their original mass spectra are presented. The fragmentation

of thymine derivatives confirm the *Diels-Alder mechanism* (in the first mass spectra series). *Diels-Alder mechanism* involves combining a diene (a molecule that possesses two alternating double bonds) and a dienophile (an alkene) to make rings and bicyclic compounds. The second mass spectra series includes dihydro 5,6-fragmentations of uracil. These molecules behave differently, as they are more sensitive to the substituents.

Rahman and Krishnakumar [2015] measured absolute partial and total electron ionization cross-sections of uracil in the gas phase as a function of energy that reached 500 eV. The relative flow technique was used to normalize the ion yield curves to the partial ionisation cross-sections. The relative flow technique for a target gas relates the differential cross-section of that gas, at a specific scattering angle and energy, to that of a reference gas under identical conditions, [Ehrhardt and Morgan, 2013]. A time-of-flight mass spectrometer was used to mass select the ions. The appearance energies for most fragments were determined. The appearance energy for the parent ion of uracil (112 u) was found to be 9.5 ± 0.7 eV.

1.5.3 Photon impact studies

This section discusses the measurements recorded by various research groups, regarding photon impact with 5-halo-uracils and uracil. Photoionisation refers to the ionisation of a molecule or atom caused by the absorption of a photon.

Jochims et al. [2005] used synchrotron radiation as an excitation source, in a 6 - 22 eV photon energy range, to perform photoionisation on uracil (as well as thymine and adenine). A quadrupole mass spectrometer was used to measure the fragments formed by photoionisation of the molecules. The entire chamber was heated to a temperature between 120 - 140°C. This temperature was sufficient to supply target molecules but also low enough that the thermally fragile nucleic acid bases did not dissociate when in the gas phase. Mass spectra were generated at 20 eV and ion yield curves were obtained through photon energy scans. The appearance energy of most photoions was determined and compared with the corresponding electron impact results. The parent ion of uracil and thymine were found to have an appearance energy of 9.15 ± 0.03 eV and 8.82 ± 0.03 eV respectively.

Itälä et al. [2010] investigated the photofragmentation of thymine and 5-bromouracil following core ionisation by soft x-rays using photoelectron-photoion-photoion coincidence techniques. Once the energy of the incident photons are resonant, electrons can be excited from a specific atomic core orbital. This experiment used a time-of-flight detector with a 400 mm drift tube and an electron energy analyser. The electronics for the ion detection system is based on a 1 GHz waveform digitiser card. Once the targets are irradiated with photons, a 1s core hole is created in one of the carbon atoms. An advantage of this method is that it provides an opportunity to study site selected fragmentation.

Itälä et al. [2011] researched the molecular fragmentation of pyrimidine derivatives following site-selective carbon core ionisation. The biomolecules investigated were 5-bromouracil, uracil and thymine. The apparatus used in this study was a hemispherical analyser and a ion time-of-flight mass spectrometer.

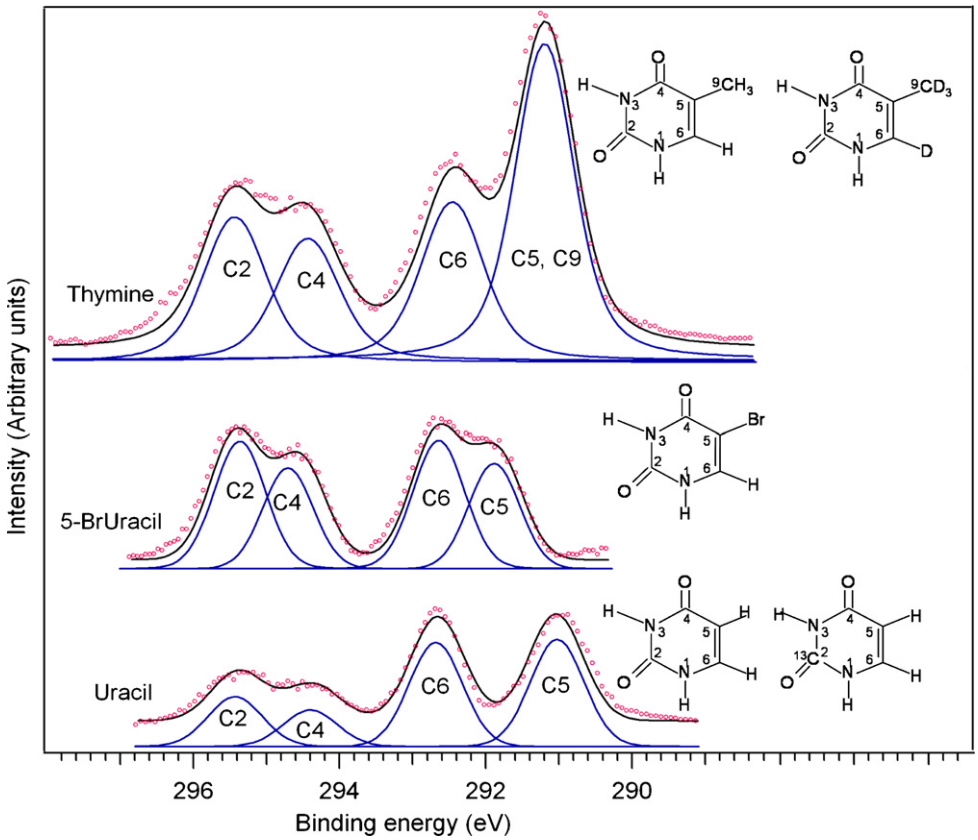

Figure 1.14: C 1s photoelectron spectrum of 5-bromouracil, thymine and uracil, [Itälä et al., 2011].

Figure 1.14 shows a photoelectron spectrum of 5-bromouracil, thymine (where 330 eV

photons were used), and of uracil (where 315 eV photons were used). It was found that, generally speaking, the surrounding bonds of a molecule that was ionised have a higher probability of undergoing bond cleavage. However, in some cases, it was found that some fragmentation pathways result in bond breakages that are not dependant on the site of the initial ionisation.

Barc et al. [2013] investigated multi-photon ionisation of uracil in a wavelength range 220–270 nm, and the resulting fragmentations were then analysed. The main components of equipment used in this experiment were a time-of-flight mass spectrometer, a molecular beam, electron gun and a supersonic expansion chamber (where the uracil molecules were heated to sublimation). The appearance energies were determined for most fragments and compared with other studies. Their results showed that hydrogen bonding to water will stabilise uracil with respect to neutral excited-state ring opening as they showed that hydration enhances particular fragmentation pathways but also suppresses the production of other fragments.

Radisic et al. [2011] studied the negative parent ions of 5-chlorouracil (UCl^-) and 5-fluorouracil (UF^-) using anion photoelectron spectroscopy. Low-energy electrons were directed using magnetic fields, into a gas expansion, producing the negative ions. The ions were transferred into a flight-tube of a 90° magnetic sector mass spectrometer with a mass resolution of 400. The determined vertical detachment energy measurements of the ions are consistent with the observation of DNA being more sensitive to radiation when the thymine molecule is replaced with a halouracil.

1.5.4 Ion impact studies

Maclot et al. [2014] have presented a study regarding the stability of the glycine cation in the gas phase after interaction with multiply charged ions. Their paper presents both an experimental and theoretical analysis. A crossed beam device and a linear time-of-flight mass spectrometer were the main apparatus used in this experiment. They found the primary fragmentation pathways consist of a bond cleavage of the C_α - $C_{carboxyl}$ bond. This primary bond cleavage led to the 28, 29, 30 and 45 amu masses. The most stable single charged glycine conformers show a geminal diol form.

In 2016, Markush et al. [2016] investigated the role of the environment in the ion induced fragmentation of uracil. An ion beam was used to induce fragmentation and the resulting fragments were extracted into a time-of-flight mass spectrometer and then detected with a Daly-type detector. They obtained mass spectra for both the pure and nano-hydrated fragments and made a comparison between them. They discovered that when the uracil is surrounded with the environment, the resulting peaks on the mass spectrum are much broader when compared to that of the uracil molecule that is not surrounded by the environment. They found that the environment plays a pivotal role in the molecular fragmentation process, as the presence of an environment acts as a protector, resulting in a lower yield for the low mass fragments.

There are several review papers regarding ion impact on uracil. The following is a list of additional research groups that have studed ion impact on uracil: [Afrosimov et al., 2015], [Agnihotri et al., 2013], and [Ferreira da Silva et al., 2011] (A comparison of the results from Ferreira da Silva et al. [2011] with results obtained in this experiment is found in Section 5.4.2).

1.6 Research presented in this thesis

The research presented in this Masters of Science thesis involves the study of positive-ion mass spectrometry of 5-fluorouracil using low-energy electron impact. The apparatus in Maynooth University is designed to investigate the results obtained from electron impact with molecules and clusters.

In chapter 2, an overview is given of varius techniques used in mass spectrometry.

Chapter 3 describes the experimental apparatus used in this work, including the creation of a suitable vacuum within the system, the testing of the efficiency and collimation of the electron gun, and the calibration of the electron energy.

Chapter 4 discusses the interfacing, data acquisition and data analysis of the experiment. This involves the calibration of the multichannel scaler and the acquisition of mass spectra. The LabVIEW programs for data acquisition and data analysis are also discussed.

Chapter 5 presents the results we have obtained for 5-fluorouracil. The mass spectrum of 5-fluorouracil is compared with that of uracil. The results from the Gaussian peak fitting are discussed and analysed, followed by the analysis of the appearance energy results that were obtained from the appearance energy fitting program. Finally, we investigate the fragmentation processes for most of the 5-fluorouracil fragments.

Chapter 2

Principles and Instrumentation of Mass Spectrometry

2.1 What is mass spectrometry?

The basic principle of mass spectrometry is to generate ions from either inorganic or organic compounds by any suitable method, to separate these ions by their mass-to-charge ratio *m/q* and to detect them qualitatively and quantitatively by their respective *m/q* and abundance, [Gross and Roepstorff, 2011]. Mass spectrometry is used to investigate the fragmentation patterns, chemical composition and the structure of molecules. Mass spectrometers are used in many fields of research including: pharmaceutical, environmental and biotechnology research, [Hassan, 2012].

A mass spectrometer consists of three primary components held under vacuum: an ion source where the molecules in their gas phase are converted into ions, a mass analyser that separates the ions based on their mass-to-charge ratio by applying electromagnetic fields, and (finally) a detector that detects the newly formed ions. This chapter will discuss the various equipment used to perform mass spectrometry including: time-of-flight mass spectrometers (which is used in this experiment), mass analysers, and mass spectrometers using ion traps.

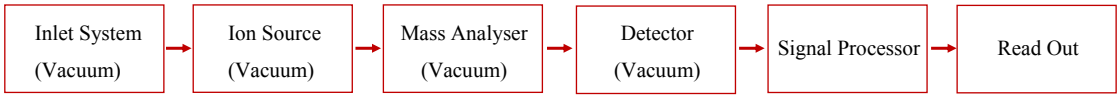

Figure 2.1: Components of a mass spectrometer.

Figure 2.1 shows the components that comprise a mass spectrometer. All mass spectrometers use an ion formation component, a component to mass analyse and an ion detection component. The procedure begins with the inlet system where the compound of interest is placed. A small quantity of the compound is introduced from the inlet system into the ion source as a gas. The ion source used in this experiment is an electron impact source but there exist other ion sources that are widely used. These ion sources include: photon ionisation, chemical ionisation, and fast atom bombardment ionisation. Most mass analysers use electric or magnetic fields to apply a force on the ions. The difference in the mass of the ions allows the mass analyser to separate the ions depending on their *m/q* ratio. In the following sections, we will briefly discuss mass analysers, mass spectrometry using traps and time-of-flight mass spectrometry. There are essential differences between the different techniques of mass spectrometry. Mass analysers filter and detect a single *m/q* at a time, ion traps are used to store and selectively release individual masses and a time-of-flight mass spectrometer - which uses a pulsed source - that detects and analyses all ions that are produced.

2.2 Mass analysers

2.2.1 Single-focusing mass spectrometer

A single-focussing mass spectrometer uses a single magnetic sector to differentiate between the *m/q* value of the ions but as the ions leaving the ion source will have different levels of kinetic energy, their velocities will not be the same. This causes a limitation on the resolution of the single-focusing mass spectrometers. The magnetic sector generates a perpendicular magnetic force onto the ions which does not effect the velocity of the ions, only their direction. The magnetic sector is a momentum analyser as opposed to one that analyses mass directly. The Lorentz Force F_L can be used to describe the effects on a charged particle inside a magnetic field:

$$F_L = qvB \tag{2.1}$$

where q is the charge of an ion, v is its velocity and B is the magnetic field. An ion of mass m travelling perpendicular to a homogeneous magnetic field will follow a circular trajectory of radius r_m implying:

$$F_L = qvB = \frac{m_i v^2}{r_m} \tag{2.2}$$

Rearranging equation 2.2 the radius r_m becomes:

$$r_m = \frac{m_i v}{qB} \tag{2.3}$$

implying that the radius r_m depends on the momentum mv of an ion and therefore the momentum depends on the ions *m/q* value, implying:

$$\frac{m_i}{q} = \frac{r_m B}{v} \tag{2.4}$$

Equation 2.4 shows the relationship between an ions *m/q* value and the magnetic field through which it is travelling, [Gross and Roepstorff, 2011]. Once the ions pass through the magnetic sector and travel through a collector aperture, they will produce a signal once they reach the detector. Single-focusing analysers fail to account for the difference in kinetic energies of ions with equal *m/q* ratio exiting the ion source.

2.2.2 Double-focusing mass spectrometer

A double-focusing mass spectrometer combines a magnetic sector and an electric sector bringing ions with differing kinetic energy distributions but equal *m/q* ratio to a focus, [Gross and Roepstorff, 2011]. The electric sector consists of two concentrically curved parallel plates. A voltage is applied to these plates to generate an electric field that will bend the trajectory of the ion beam as it travels through the mass analyser. The electric sector is used to minimise the kinetic energy distribution of the ions which increases the mass resolution of the magnetic sector, [Skoog et al., 2017]. The radius of an ions trajectory is dependent on the kinetic energy of that ion and the voltage applied across the two deflecting plates. The equation that describes the radius of an ions trajectory can be defined as $r = 2V/E$. This equation shows that the radius of an ions trajectory is independent of its *m/q* ratio. The electric sector brings ions with differing kinetic energies to a focus whereas the magnetic sector separates the ions depending on their *m/q* ratio.

The ions are accelerated into the magnetic sector with uniform energy. The magnetic sector separate the ions depending on their mass by analysing their momentum. The

deviation of trajectory for ions that are too heavy and too light will not traverse the magnetic sector toward the detector slit positioned at the end of the mass spectrometer. This causes an ion optical system that focuses ions on a single image position. These slits can be narrowed which will increase mass resolution but will decrease the count rate of ion detection. The slits define the energies and locations of the ions, [Dass, 2007]. The benefits of double focusing include: much higher mass resolution, high dynamic range, high sensitivity and very high reproducibility.

2.2.3 Quadrupole mass spectrometer

A linear quadrupole mass analyser consists of four cyclindrically or hyperbolically shaped rod electrodes that are assembled in a square configuration, [Gross and Roepstorff, 2011], as shown in Figure 2.2.

Two opposite rod electrodes have an applied potential of $+(U + V\cos\omega t)$ with the other two having an applied potential of $-(U + V\cos\omega t)$, where U represents the DC voltage and the AC voltage is given by $V\cos\omega t$. If a positive AC potential is applied to the x-rods, for example, a positive ion would move towards the centre axis between the two x-rods. When the potential became negative, the ion would then accelerate towards the x-rods due to the attractive force. If the attractive force was sufficient so that the ion came into contact with either rod, it would result in that ion being removed from the system. There are a few factors that determine whether an ion will be removed from the system when the potential is negative, and they include: the charge of the ion, the frequency regarding the AC potential and the mass of the ion.

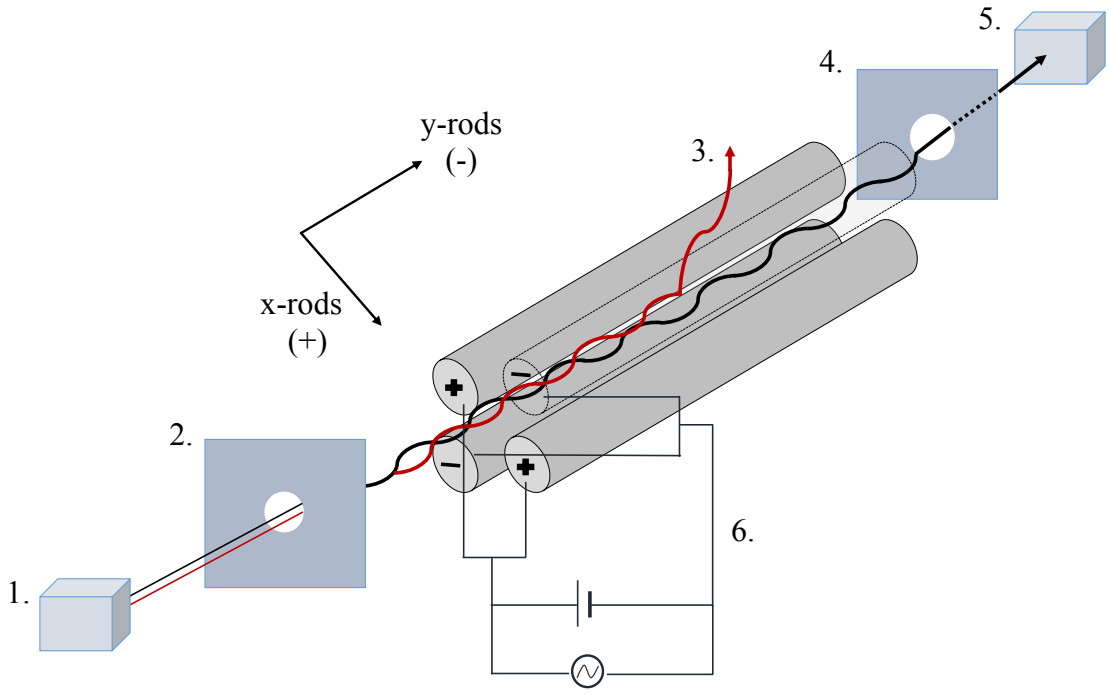

Figure 2.2: Image of a linear quadrupole mass analyser adapted from Project [b].

Figure 2.2 shows a linear quadrupole mass analyser with the different components numbered. Component 1 is the ion source, 2 is the ion optics component to accelerate and focus the ions through an aperture into the quadrupole mass filter, 3 shows the trajectory of a non-resonant ion that will not be detected, 4 shows the trajectory of a resonant ion that will be detected once it has travelled through the exit aperture, 5 is the ion detector that detects ions that have traversed the mass filter, and 6 shows the DC and AC voltage configuration. The DC and AC voltages generate a potential that will only allow ions with a specified *m/q* value to pass through the quadrupole toward the detector. The ions are separated in a quadrupole based on the stability of their trajectories when travelling through the oscillating field. Ions that have unstable trajectories will be removed from the system when they collide with the quadrupole rods or escape from the quadrupole.

Ions with different masses can be detected by varying the voltages so that an ion traverses the quadrupole to the detector. Conventionally, the x-rods of the quadrupole represent a high-pass mass filter allowing ions with large mass to be transmitted through the quadrupole and reach the detector (without hitting the x-rods). The y-rods of the quadrupole represent a low-pass mass filter, allowing low mass ions through (without

hitting the y-rods), see Figure 2.2. The benefits of using a linear quadrupole include: classical mass spectra, low cost systems and good reproducibility.

2.3 Trap mass spectrometry

An ion trap uses electric and magnetic fields to capture charged particles. The Paul trap and the Penning trap are the two most common types of trap used to capture ions. A Penning trap uses a homogeneous magnetic field and a quadrupole electric field to contain ions within a given region. The Penning trap combines electric and magnetic fields to confine the ions whereas the Paul trap forms a potential via a combination of static and oscillating electric fields. Ion trapping mass spectrometers such as the Fourier transform ion cyclotron resonance mass spectrometer and a quadrupole ion trap, capture the ions within a confined region of space where they are subject to time dependant fields, [March and Todd, 1995]. A Fourier transform ion cyclotron resonance mass spectrometer uses a Penning trap to confine the ions.

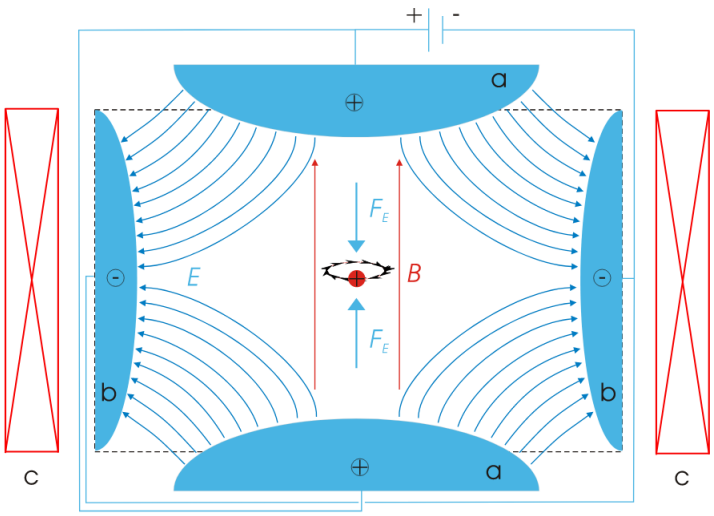

Figure 2.3: Image of a Penning trap, [Arian Kriesch Akriesch]

Figure 2.3 shows the homogeneous electric field that is generated by two end caps denoted as 'a' and a ring electrode denoted as 'b', with a superimposed magnetic field B that is generated with a surrounding cylindrical magnet 'c'. The measurement of the mass of the ion is carried out via the determination of the characteristic cyclotron frequency given by $v_c = qB/2\pi m$, [Eitel et al., 2008].

A quadruple ion trap, or *Paul Trap* named after its inventor, stores ions within defined boundaries for a defined period in time, [March and Todd, 2005]. A quadrupole ion trap consists of two hyperbolic electrodes with their foci facing each other that are used as end caps, as well as a ring electrode, see Figure 2.4. The two hyperbolic electrodes are electronically connected and a potential is generated between them and the ring electrode. The ring electrode and the two endcap electrodes are supplied with suitable AC voltages, [Gross and Roepstorff, 2011].

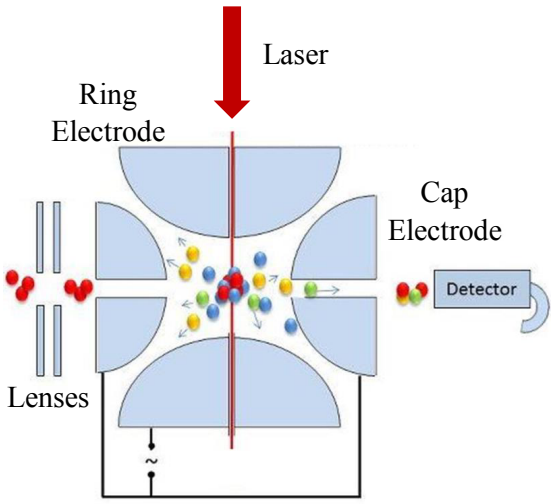

Figure 2.4: Image of a quadruple ion trap, [Pinimg].

Figure 2.4 shows the configuration of the quadrupole ion trap and the resonance AC voltage being applied to the two endcap electrodes. These are used to create stable trajectories for ions with a specified *m/q* while removing other ions. The unwanted ions are removed from the system when they collide into the walls of the mass analyser, or by axial ejection, [Gross and Roepstorff, 2011]. An issue with using ion traps to perform mass spectrometry is that the captured ions could eventually spontaneously fragment, known as unimolecular decomposition, which would result in unexpected peaks in the mass spectrum. Space-charge effects (ion-ion repulsion) limit the dynamic range of the ion trap. The benefits of quadrupole ion trapping include: they can achieve high sensitivity as well as being a relatively compact analyser.

2.4 Time-of-flight mass spectrometry

A time-of-flight mass spectrometer is a type of mass spectrometer that measures the time it takes for ions of varying *m/q* values to travel from the ion source to a detector. The first commercial time-of-flight mass spectrometer was the linear time-of-flight mass spectrometer, designed and published in 1955 by Wiley and McLaren [de Hoffmann and Stroobant, 2013]. This instrument was of vital importance to Curl, Kroto and Smalley, [Smalley, 1997], when they shared the Nobel Prize in Chemistry in 1966 for their discovery of fullerenes. It was the availability of time efficient data acquisition with fast working electronics and processing of data, alongside the capability of using pulsed ion sources that pushed the time-of-flight mass spectrometer to the forefront of atomic and molecular research.

In time-of-flight mass spectrometry, the ions are created from a pulsed laser or pulsed electron source. They are extracted from the ion source and directed into a field-free time-of-flight tube by a potential that is applied to an extraction grid. The mass-to-charge ratio of an ion is determined by analysing the time taken for an ion to reach the detector once it has been extracted into the flight-tube. The time taken for a singly charged ion to travel down the flight-tube is proportional to their *m/q* value assuming that the ions all receive the same level of kinetic energy. The time measurements and ion abundance measurements are recorded by the detector. Mass spectra are accumulated by collecting the ions from the electron pulses and laser pulses. Two types of time-of-flight mass spectrometry include: linear time-of-flight mass spectrometry and reflectron time-of-flight mass spectrometry, see Figure 2.5. Both types of time-of-flight mass spectrometer are discussed below, beginning with a brief discussion of the linear time-of-flight mass spectrometer.

2.4.1 Linear time-of-flight mass spectrometry

In a linear time-of-flight mass spectrometer, the ions are accelerated in two stages and extracted into a field free region where they drift towards a detector situated at the end of the flight-tube, [Wiley and McLaren, 1955]. A spectrum can be generated by analysing the flight time of each ion. The linear time-of-flight mass spectrometer has some limitations, arising from space charge effects and the kinetic energy distribution. Space charge defects refers to the issues caused by the size of the volume where the ions are formed (ions

entering the field free region at different times). Molecules within the ion source receive different levels of energy from the electron pulse or laser pulse resulting in the formation of ions with varying kinetic energies. The varying levels of kinetic energy broaden the peaks in the mass spectrum decreasing the mass resolution.

Figure 2.5 shows the difference in the arrangement of a linear time-of-flight mass spectrometer and a reflectron time-of-flight mass spectrometer. The main difference between a linear time-of-flight mass spectrometer and a reflectron time-of-flight mass spectrometer is that a reflectron time-of-flight mass spectrometer uses a reflector component to perform second order focussing in flight time of ions with the same *m/q* ratio, whereas a linear time-of-flight mass spectrometer only provides first order focussing.

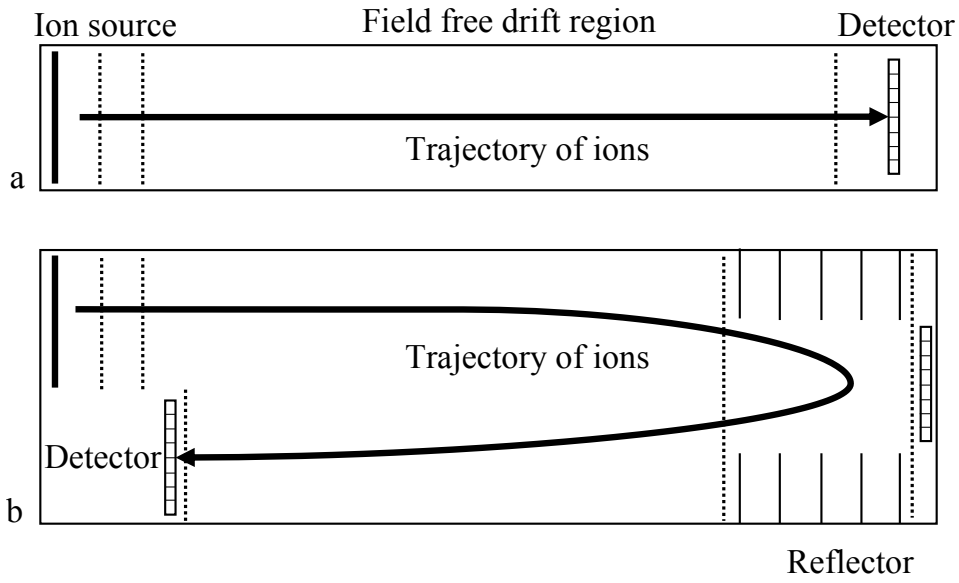

Figure 2.5: Basic configuration of a linear time-of-flight mass spectrometer (a), and a reflectron time-of-flight mass spectrometer (b).

2.4.2 Reflectron time-of-flight mass spectrometry

A reflectron time-of-flight mass spectrometer consists of an ion source, a time-of-flight tube, a reflector that acts as an ion mirror, and a detector. Mamyrin was the first person to propose a second order focussing *reflectron* or *reflector*, [Boesl, 2016]. To supply second order focussing, the reflector uses a static electric field with the same polarity as the ions, to focus the ions toward the detector. This retarding electrostatic field is produced inside

the reflector which is positioned at the end of the field free flight-tube. The distance in which an ion penetrates the retarding field within the reflector depends on the *m/q* ratio and the kinetic energy of the ion. Ions that have high levels of kinetic energy will penetrate the electric field more deeply than ions with low kinetic energy. This increase in path length causes ions with varying levels of kinetic but equal *m/q* to arrive at the detector at the same time.

For this experiment, a reflectron time-of-flight mass spectrometer by R.M. Jordan Company was used to detect the ions, see Section 3.4 for a detailed description. A *Mamyrin design* [Mamyrin, 2001] time-of-flight mass spectrometer tilts the reflector off at a small angle with respect to the ion source, so the detector can be placed adjacent to the ion source. In this experiment we use a set of deflection plates. An Einzel lens is used to provide a certain amount of focussing of the ions extracted into the mass spectrometer. An Einzel lens focuses the ions without changing their energy. The ions are then reflected towards a detector located underneath the entry to the flight-tube. The reflector corrects for a small dispersion in the initial energy of the ions with the same *m/q* ratio.

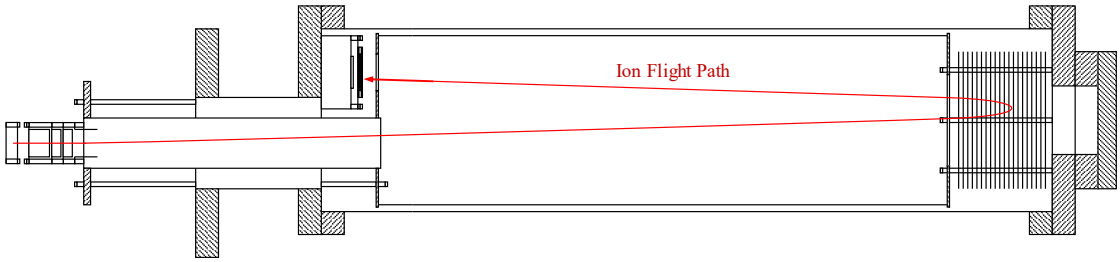

Figure 2.6: Reflectron time-of-flight mass spectrometer.

The flight time of an ion in a reflectron time-of-flight mass spectrometer can be described as: [Mamyrin, 2001]

$$t = A_0\left[\frac{A_1}{\sqrt{k}} + A_2(\sqrt{k} - \sqrt{(k-p)}\right] = A_0 F \tag{2.5}$$

where $k = \frac{U}{U_0}$ and $p = \frac{U_b}{U_0}$. qU_0 describes the average energy of the ion and qU is

the energy of the ion corresponding to the ion velocity components. Quantities A_0, A_1 and A_2 are now defined as:

$$A_0 = \frac{4d_r}{\sqrt{\frac{2qU}{m}}}\frac{U_0}{U_r}$$

$$A_1 = \frac{L_1+L_2}{4d_rU_0}$$

$$A_2 = \frac{d_b}{d_r}\frac{U_r}{U_b}$$

A_1 and A_2 being independent of mass and charge, U_b refers to the potential difference inside the deceleration gap d_b. U_r is the potential difference in the reflecting gap d_r. L_1 and L_2 are the lengths of the flight paths that span the reflecting field and the field-free drift region, see Figure 2.6. A_0 can be manipulated to yield:

$$A_0 = \frac{4d_r}{\sqrt{\frac{2qU}{m}}}\frac{U_0}{U_r} = \frac{4d_r}{\sqrt{2U}}\frac{U_0}{U_r}\sqrt{\frac{m}{q}}$$

When the equations for A_0, A_1 and A_2 are inserted into equation 2.5 we are left with a flight time of:

$$t = A\sqrt{\frac{m}{q}} + B \tag{2.6}$$

with $A = \frac{4d_r}{\sqrt{2U}}\frac{U_0}{U_r}\left[\frac{A_1}{\sqrt{k}} + A_2(\sqrt{k} - \sqrt{(k-p)}\right]$

B is a term used to accommodate for the delay of the extraction pulse and the multi-channel scaler card, discussed in Section 4.1. Using equation 2.6, the relationship between time and an ion *m/q* value is:

$$\frac{m}{q} = (Ct + D)^2$$

where $C = \frac{1}{A}$ and $D = -\frac{B}{A}$.

Chapter 3

Experimental Apparatus

3.1 Overview of the molecular beam experiment

This chapter describes the apparatus used for the research carried out in this thesis. This chapter will discuss in detail the different parts of the apparatus as well as any modification made for this study. The molecular beam experiment consists of three interconnected vacuum chambers as shown in Figure 3.1: the expansion chamber, the collision chamber and the flight-tube. The experiment consists of a differentially pumped vacuum. The system is kept under a suitable vacuum using a combination of forepumps and turbopumps discussed in Section 3.1.1. A vacuum lessens the probability of unwanted collisions within the system.

The oven, bracket and a skimmer are all situated within the expansion chamber. The bracket is a part of a top-hat arrangement that provides alignment between the aperture of the skimmer and the capillary of the oven. The top-hat arrangement is used to separate the expansion chamber and the collision chamber. The 5-fluorouracil is vaporised inside the oven. The electron gun, Faraday cup and the ion extraction grids are situated inside the collision chamber. The molecules are ionised and undergo fragmentation within the collision chamber. The reflectron time-of-flight spectrometer and the microchannel plate detector are situated inside the flight-tube. The total length of the system is approximately 2 m. The vacuum chambers are supported by an aluminium frame. The primary sections of the reflectron time-of-flight mass spectrometer can slide along the structure of the aluminium frame, allowing access into the various compartments of the system.

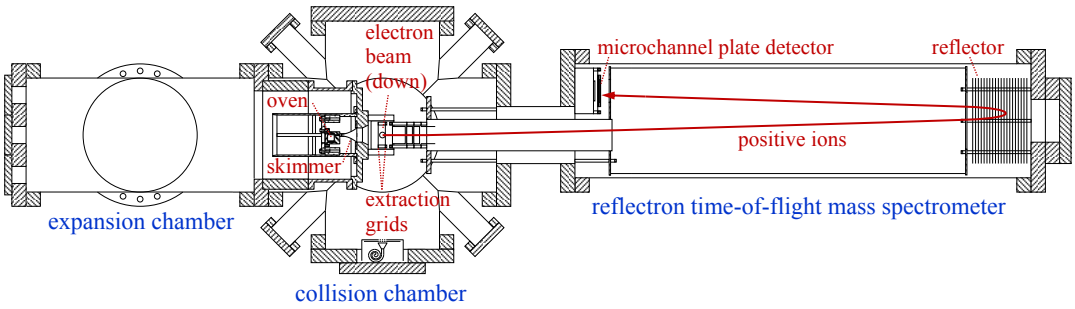

Figure 3.1: Overview of the molecular beam experiment.

Copper gaskets are used on the flanges that seal the three main chambers together, (for a few flanges viton o-rings are used). The expansion chamber is where the molecular beam of 5-fluorouracil is produced through sublimation inside a heated oven. This process is discussed in more detail in Section 3.2.1.

Section 4.2 discusses the process of ion extraction in depth. The electron beam passes between two grids where one grid is charged, discussed in Section 3.4. Using charged electrodes, the fragments are extracted into the reflectron time-of-flight mass spectrometer. The ions are detected using a multichannel plate detector (MCP) situated within the flight-tube.

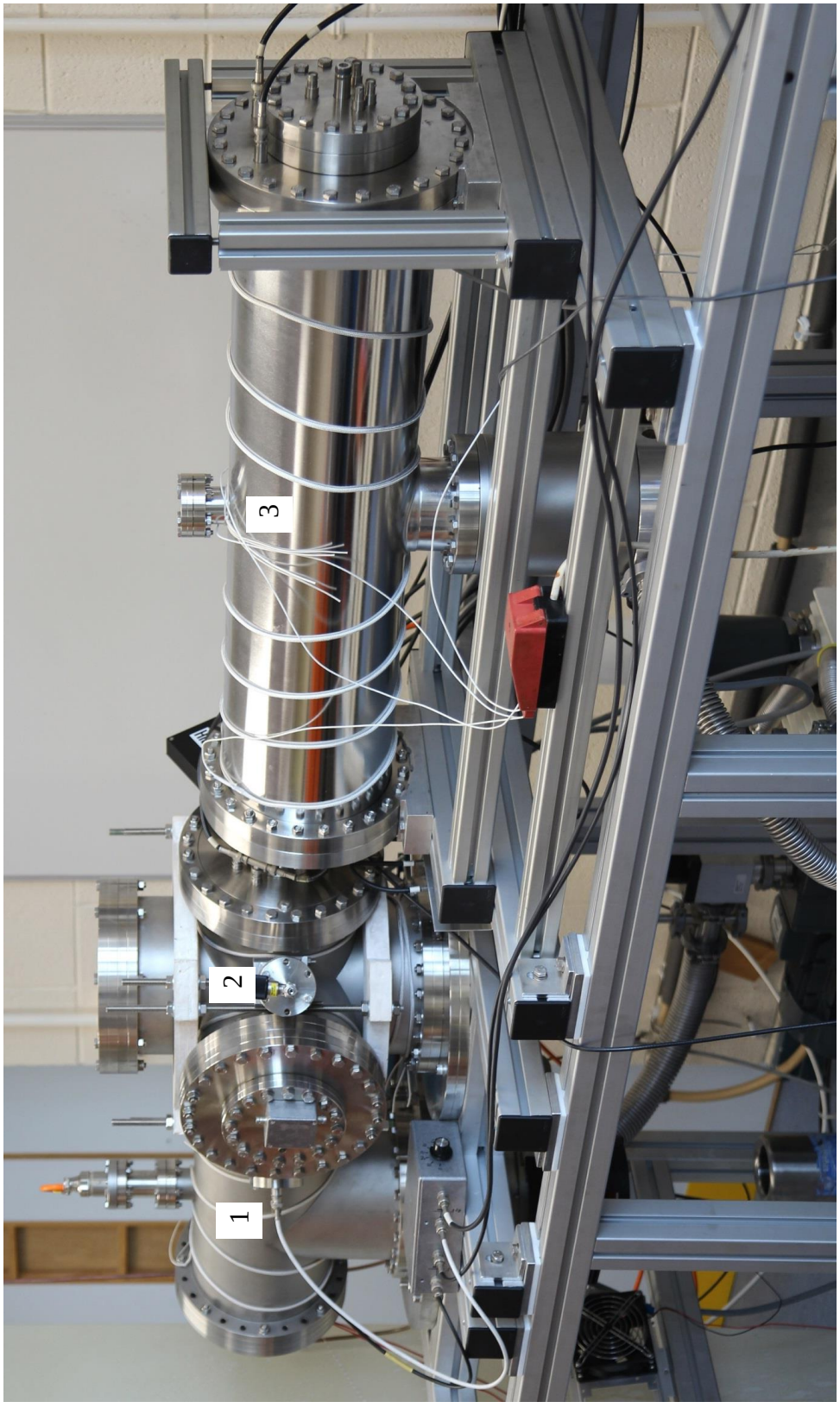

Figure 3.2: Photo of the molecular beam experiment. 1 - Expansion chamber, 2 - Collision chamber, 3 - Flight-tube.

3.1.1 Vacuum system

Three turbopumps backed up by two forepumps are used to keep the entire system at a suitable vacuum. The Leybold TurboVac 360 turbopump on the expansion chamber is backed up by an Alcatel 2063 SD rotary vane pump, and the two Leybold TurboVac 361 turbopumps on the collision chamber and the flight-tube are both backed up by the same Leybold Trivac D25B rotary vane pump. To evacuate the vacuum system after it has been exposed to atmospheric pressure, the rotary vane pumps are started first until the pressure in the vacuum system is low enough and the turbopumps can be started. Once the evacuation procedure is complete, the pressure in the vacuum system is typically $\approx$ 2x10^{-8} mbar.

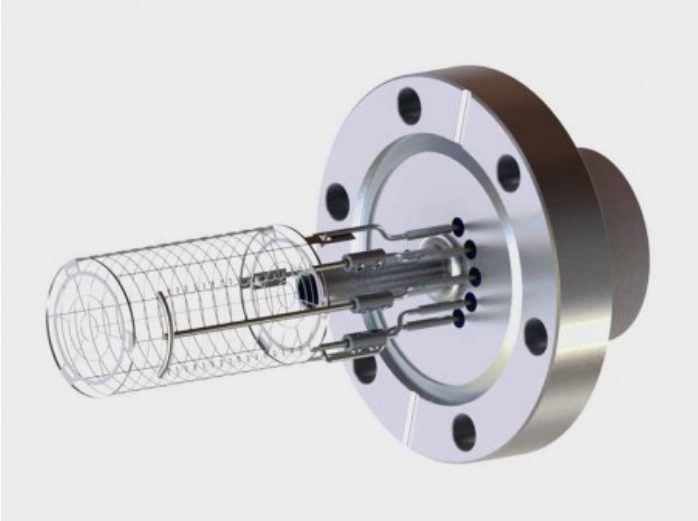

Figure 3.3: The ionisation gauges of this type are used in the experiment, [Project [a], Nude Bayard-Alpert].

The pressure within the system is measured using two AML ionisation gauges and two AML pirani gauges. Each pair of ionisation gauge and pirani gauge is monitored using an Arun Microelectronics PGC2 Pressure Gauge Controller. One of the ionisation gauges used in this experiment can be seen in Figure 3.3. The ionisation gauges measure the pressure inside the collision chamber and the flight-tube whereas the two pirani gauges measure the pressures within the fore-lines of the forepumps.

3.1.2 Interlock system

An interlock system is used as a safety mechanism that will shut down the running of the experiment in the event of equipment failure, which enables the experiment to be ran over an extended time period.

The interlocking of the system prevents the damage of other apparatus, caused by the failing equipment. To ensure this, the three turbopump controllers and the two pressure gauge controllers are connected to the interlock box. Pressure trip points for the ionization gauges and the pirani gauges are set on each of the pressure gauge controllers. The interlock box has five toggle switches on its front panel, for each of the controllers connected to it, so that each of these can be bypassed during the pump-down of the vacuum system. The pieces of apparatus are the following: the three turbo-pumps and the two pirani gauges. If the trip points are activated, the interlock box will receive a signal that implies equipment failure. If this occurs, it was result in the shut-down of the experiment.

3.2 Expansion chamber

The expansion chamber is the left chamber in Figure 3.1. The expansion chamber is separated from the collision chamber by a top-hat arrangement, shown in Figure 3.4, which ensures the correct alignment of the oven, the skimmer and the electron gun. The expansion chamber is where the beam of 5-fluorouracil is generated, inside the resistively heated oven, and collimated using an electroplated skimmer. A skimmer is a conical device that creates a collimated beam of 5-fluorouracil as it enters the collision chamber. The skimmer separates the expansion chamber from the collision chamber. Its aperture is 1.2 mm.

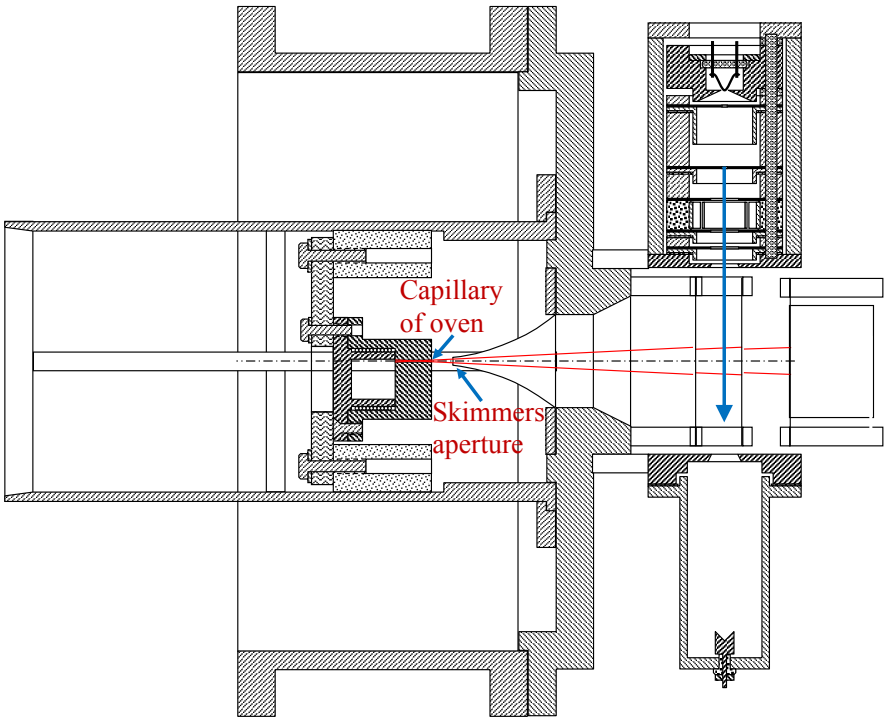

Figure 3.4: Diagram of the top-hat arrangement, showing the oven inside its mounting bracket, the skimmer, the electron gun and the Faraday cup.

Figure 3.4 shows the skimmer which has a diameter of 1.2 mm mounted on a top-hat arrangement separating the expansion chamber and the collision chamber. The bracket in also part of the top-hat arrangement and aligns the capillary of the oven with the aperture of the skimmer.

3.2.1 Oven

The oven is a cylindrical copper compartment that contains the 5-fluorouracil and is situated inside the expansion chamber. The front of the oven contains a 0.5 mm diameter capillary that is positioned such that it lies above the surface of the 5-fluorouracil. Figure 3.5 shows the aperture of the oven positioned above the 5-fluorouracil. The dashed line in Figure 3.4 shows the alignment of the capillary in the oven with the skimmer.

An Omron E5CK digital controller and a Thurlby Thandar PL330 power supply control the temperature of the oven that is measured using a thermocouple. A Thermocoaxial SEI 10/50 heater is used to heat the 5-fluorouracil to sublimation. It will then effuse through the capillary of the oven toward the skimmer. A portion of the 5-fluorouracil will fail to enter the skimmer due to the spreading of the beam as it exits the oven. When the oven is

in operation, the pressure within the expansion chamber increases to 2x10^{-7} mbar.

3.3 Collision chamber

The collision chamber can be seen in detail in Figure 3.5. The molecular beam enters the collision chamber through the skimmer and is crossed at a right angle with a beam of electrons that ionise and fragment the 5-fluorouracil molecules. The electron beam is produced by the electron gun (see section 3.3.1), passes between two extraction grids, G1 and G2 (see Section 3.4), and is collected in the Faraday cup.

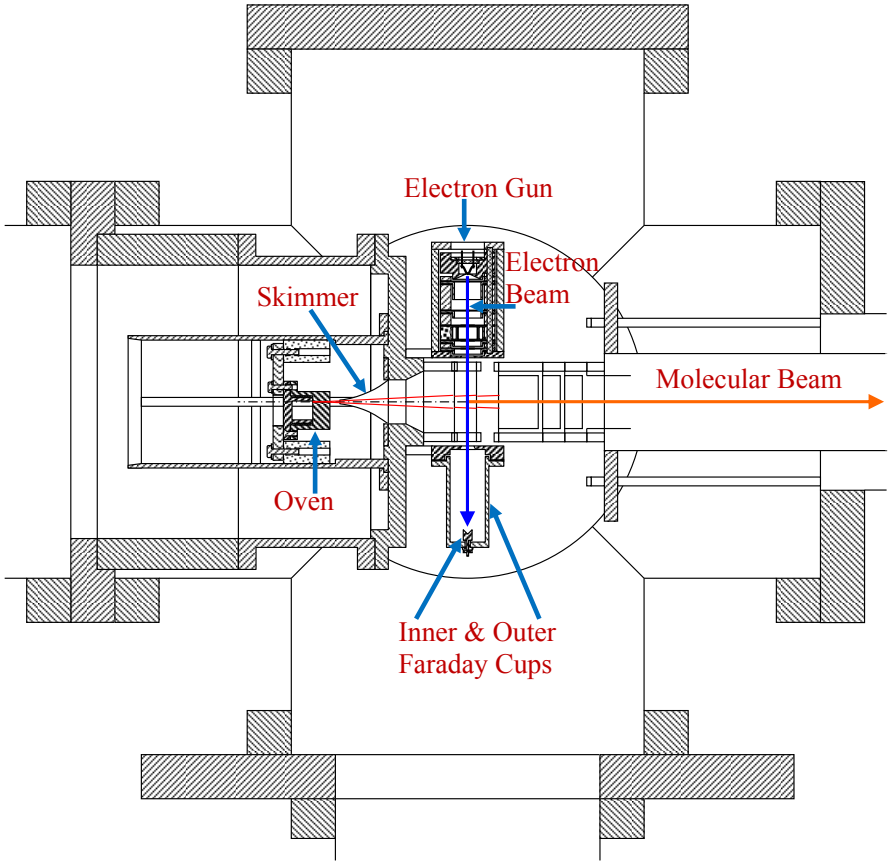

Figure 3.5: Diagram of the collision chamber.

The interaction region is formed by the overlap of both beams and is centred between the extraction grids. The ions that are created within the interaction region are extracted into the reflectron mass spectrometer by pulsing the extraction grid G2 (see section 3.4).

3.3.1 Electron gun

For this experiment, a new electron gun was assembled with better suited materials. The original electron gun had a filament holder made from stainless steel and cylindrical aluminium elements with molybdenum apertures in between.

Figure 3.6: The assembly of the electron gun.

Figure 3.6 shows the new electron gun, where all the electrostatic lens elements were machined from solid pieces of molybdenum. The insulating spacers between the lens elements are made from macor. Figure 3.7 is a schematic digram showing a cross-section of the electron gun, collision chamber and the Faraday cup.

Figure 3.7 shows that the Faraday cup consists of an outer cup, biased at 10 V, and an inner cup biased at 40 V. Apart from collecting the electron beam, the Faraday cup is used to determine the collimation of the electron beam by monitoring the currents on both the inner cup and the outer cup, see Section 3.3.2. A current is passed through the filament situated inside the electron gun using a Thurlby Thandar PL154 power supply, while a Farnell L30B is used as the power supply for the filament holder. The filament holder 'grid' is biased at V_{grid} = -2.5 V relative to the tip of the filament. The pulse width of the electron beam is 0.5 μs which is sufficient to achieve high mass resolution.

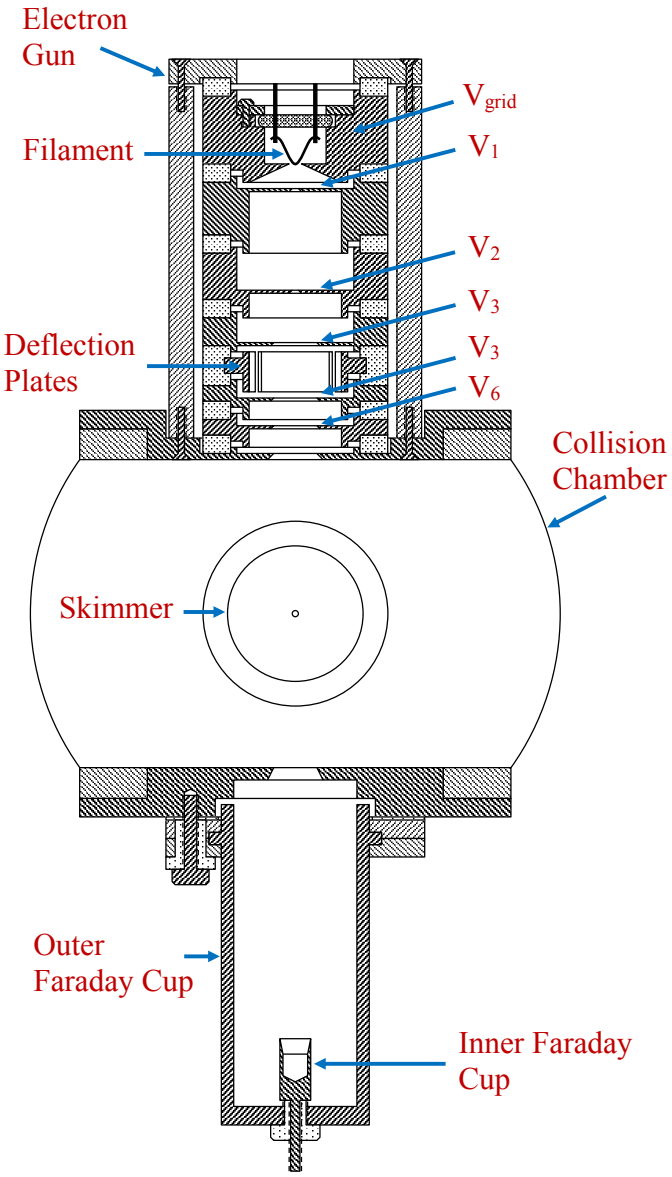

Figure 3.7: Schematic diagram of the electron gun and Faraday cup.

As the current passes through the filament, electrons are being emitted and directed into the collision chamber using electrostatic lens elements to accelerate and decelerate the electrons. The electron beam is pulsed which is discussed in detail in Section 4.2. The charged electrostatic lens elements collimate and focus the electron beam before it enters the collision chamber. The collimated electron beam is crossed with the collimated molecular beam ionising the molecules within the collision chamber. A control box is used to control all electron gun voltages. The control box operates with a resistor divider network shown in Figure 3.8, and provides test points for checking the voltages while the gun is in operation. The voltages on the electron gun elements, V_1, V_2, V_3 and V_6, are varied to achieve a satisfactory electron beam setting. Four deflection plates (X_1, X_2, Y_1,

Y_2) are mounted inside lens element V_3. These values were set using a multimeter and can be seen in Table 3.3.1.

Indicative Electron gun voltages and Faraday cup currents			
V_{grid}	-2.49 V	$V_{filament}$	+2.85 V
V_1	+46.1 V	$I_{filament}$	+2.245 V
V_2	+205.7 V	X1/X2	+7.36 $\pm$ 0.0 V
V_3	+32.4 V	Y1/Y2	-11.59 $\pm$ 11.0 V
V_6	+37.2 V	$V_{Incident}$	+100 V
Inner Faraday cup	+6.3 nA	Outer Faraday cup	+0.2 nA

Table 3.1: Electron gun voltages and Faraday cup currents.

The deflection plates steer the electron beam in a direction that is dependent on the voltages applied to these plates. Figure 3.8 shows the circuitry of the electron gun.

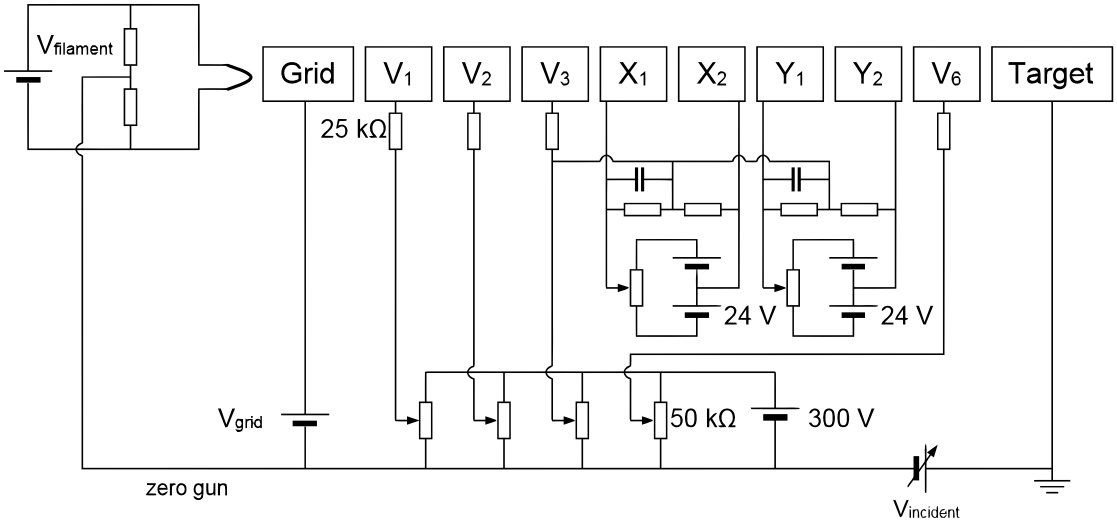

Figure 3.8: Circuitry of the electron gun.

A KEPCO APH 500M supplies 300 V to the control box that operates with a resistor divider network. A set of potential dividers inside the control box allow specified voltages to be applied to the electrostatic lens elements. The circuit is assembled so that V_1, V_2,

V_3 and V_6 do not need to be altered each time $V_{incident}$ is changed. A second KEPCO power supply, labelled $V_{incident}$ in Figure 3.8, controls the electron impact energy.

The Faraday cup collects the incident electron beam as it is positioned underneath the electron gun as shown in Figure 3.7. The Faraday cup consists of an inner and outer cup that together measure the beam current as a function of incident energy. Two Keithley 610C ammeters are connected to a National Instruments USB myDAQ device. The currents in both Faraday cups are displayed on Keithley 610C ammeters.

3.3.2 Testing of the electron gun

Figure 3.9 shows the performance of the electron gun when the incident electron energy is varied. As mentioned above, $V_{incident}$ is the varied incident electron energy, see Figure 3.8. The aim was to achieve a sharp stable current with low applied voltage to the electron gun elements. A LabVIEW program was used to control the KEPCO APH 500M power supply that varied the incident electron energy. The KEPCO power supply sets the acceleration voltage of the electron gun. A step size of 0.25 V was set in LabVIEW for the KEPCO power supply to increment by, until it reaches the set maximum of 100 V. Minimum, maximum and the incremental voltages are specified in the LabVIEW program.

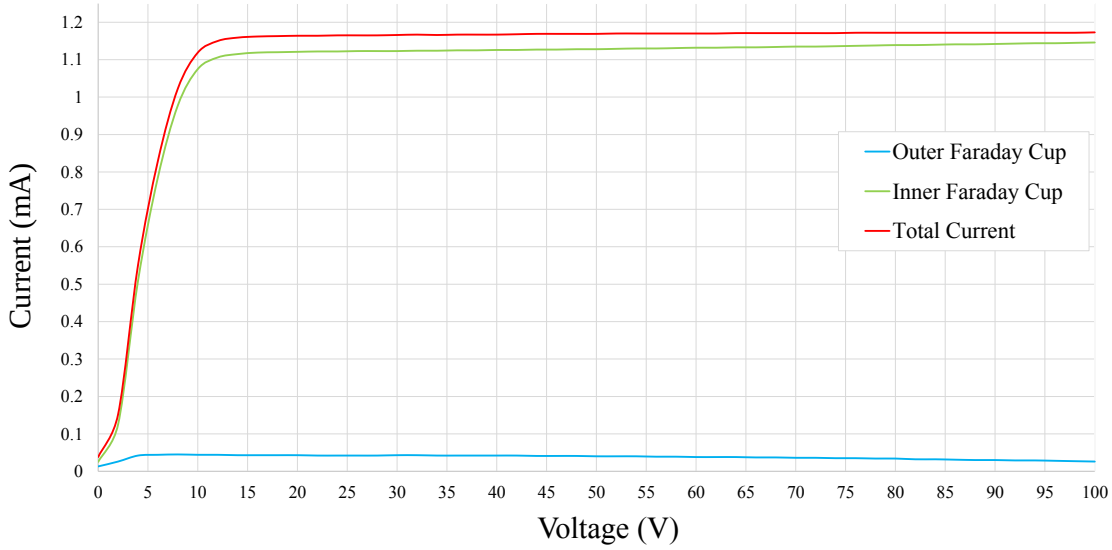

Figure 3.9: Optimum electron gun setting (of current vs applied voltage).

Measuring the currents in both the inner and outer Faraday cups gives an indication

of the shape of the electron beam. The best setting for the electron gun is determined by optimising the combination of voltages, V_1, V_2, V_3, V_6 and the deflection plates such that the total current is constant to as low a voltage as possible. Figure 3.9 shows a stable current from 13 V up to 100 V. The current is not constant below 13 V.

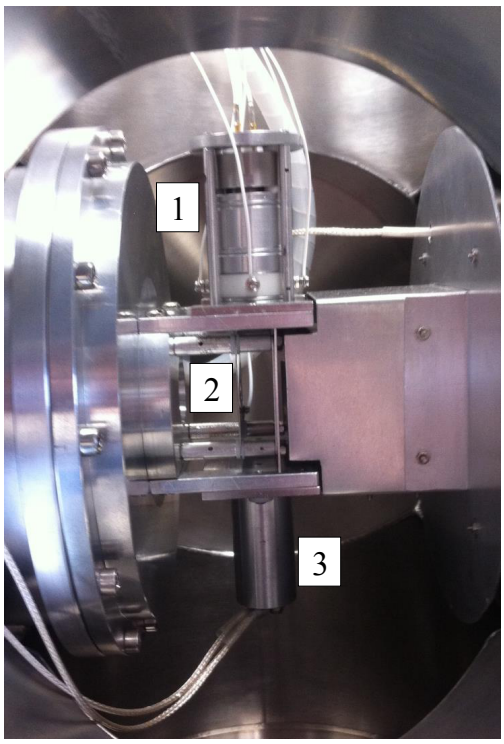

Figure 3.10: Photo of 1 - The electron gun, 2 - The interaction region and 3 - The Faraday cup.

The Faraday cup is positioned directly below the electron gun so that it collects the electron beam, see Figure 3.10. The oven is off when optimising the settings for the electron gun. From analysing the current obtained by the outer and inner Faraday cups, we can determine if the electron beam is sufficiently collimated. If the electron beam was not sufficiently collimated, Figure 3.9 would show an increase in current in the outer Faraday cup. As Figure 3.9 suggests, most of the electron beam was gathered by the inner Faraday cup showing good collimation.

3.3.3 Calibration of the electron energy

The onset voltage in this section refers to the voltage of the Kepco power supply. It is this voltage that allows the determination of the electron impact energy. The ionisation yield

curves for the 17 u and 18 u were generated by summing the counts in both peaks in the mass spectra.

For the energy calibration in this experiment, we analysed observed onset energies for water peaks 17 u and 18 u, and compared them with accepted results. This involved analysing the electron impact ionisation cross-section of the 17 u and 18 u water molecules. The results cited in Itikawa and Mason [2005] are the results used for comparison.

The ionisation energy of H_2O^+ and OH^+ were found to be 12.261 $\pm$ 0.002 eV and 18.116 $\pm$ 0.003 eV respectively, as cited by Itikawa and Mason [2005]. The ion yield curves generated for the 17 u and 18 u are superimposed onto the accepted cross-sections for the 17 u and 18 u. We used a scaling factor of 0.006 and a shift in the horizontal axis (calibration constant), to achieve overlap of the ion yields with the partial ionisation cross-sections results from Itikawa and Mason [2005].

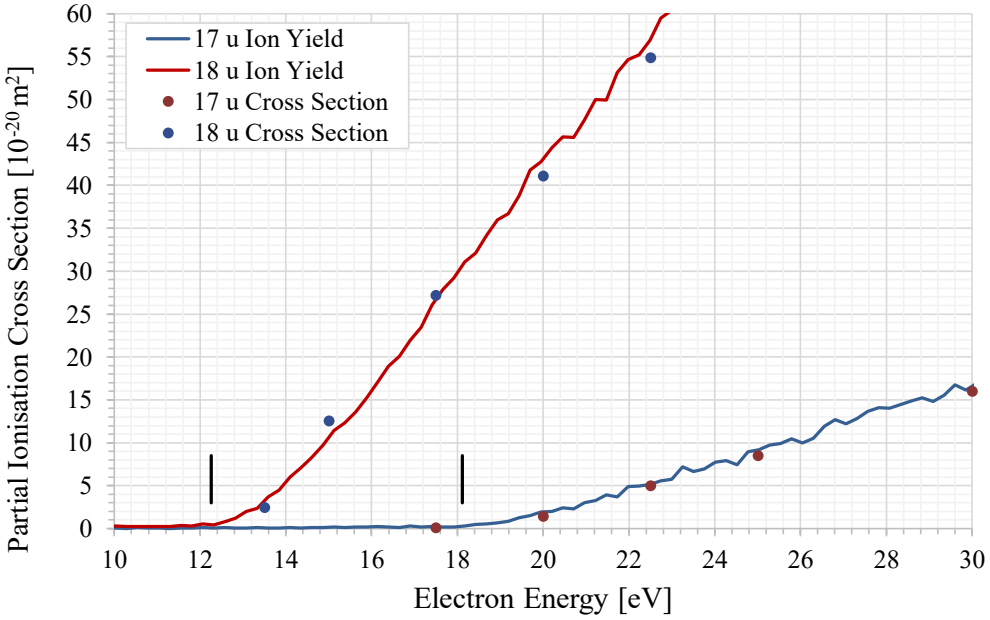

Figure 3.11: Energy calibration using water peak cross-sections from [Itikawa and Mason, 2005]. The black vertical lines indicate the onset positions.

Figure 3.11 shows optimal overlap between the accepted cross-sections and the obtained ionisation yield curves of the 17 u and the 18 u water peaks. The calibration constant was found to be -1.3 V with an estimated error of 0.2 V.

Equation 3.1 shows the relationship between the incident energy and the incident voltage.

$$E_i = V_i - 1.3 \tag{3.1}$$

where E_i is the incident energy (eV) and V_i is the incident voltage (V). Once the calibration constant was determined, it was then applied to the voltage values read from the Kepco power supply.

3.4 Reflectron time-of-flight mass spectrometer

The reflectron time-of-flight mass spectrometer separates the ions by mass to charge ratio based on their flight time. Extraction electrodes are positioned on either side of the electron beam to extract the ions into the time-of-flight mass spectrometer, see Figure 3.12.

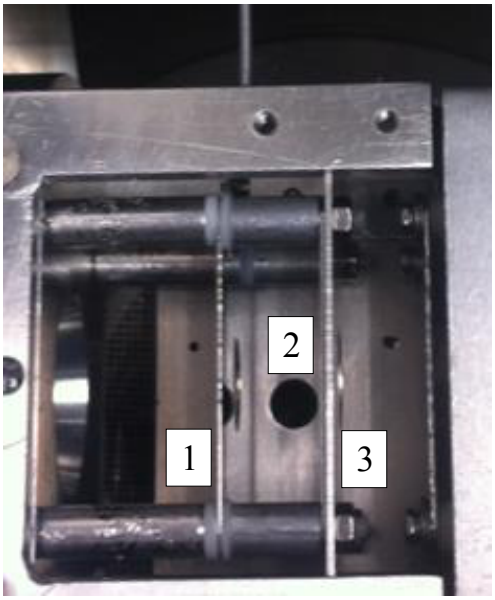

Figure 3.12: Photo of the interaction region. 1 - Extraction grid G1, 2 - Entrance to Faraday cup, 3 - Extraction grid G2.

The ions are extracted from the collision chamber due to a potential difference between extraction grids G1 and G2. G1 is pulsed positive and G2 is kept at ground. The pulsing is discussed in detail in Section 4.2.

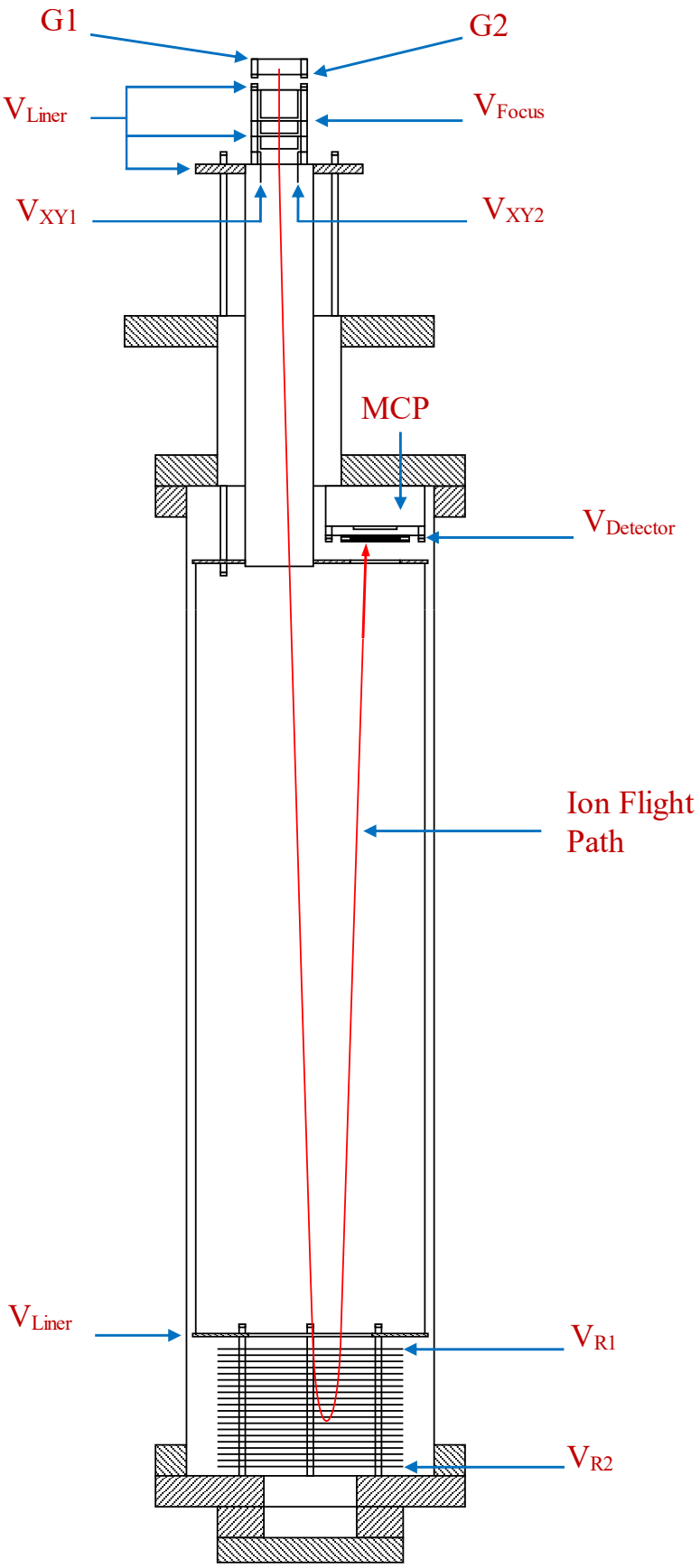

Figure 3.13: Schematic drawing of the reflectron.

Figure 3.13 is a schematic diagram of the reflectron flight-tube. The ions extracted from the collision chamber are accelerated before they enter the field-free flight-tube. A liner inside the flight-tube is held at -1200 V. It can be seen that the flight path of the ions is manipulated by using an Einzel lens and a pair of deflection plates. An Einzel lens focuses the ions without changing their energy. A voltage of -1200 V is applied to the first and third electrodes of the Einzel Lens denoted as V_{Liner} in Figure 3.13. The second electrode, V_{Focus}, is set to a voltage of -1400 V.

The microchannel plate detector is positioned adjacent to the entrance of the flight-tube from the collision chamber. In order for the ions to reach the detector, they need to be directed toward the reflector in an off-axis trajectory. A potential difference between the deflection plates XY1 and XY2 cause an off-axis trajectory of the ion beam (V_{XY1} = -1200 V and V_{XY2} = -1160 V).

The ions enter the reflector and are reflected back into the flight-tube by the electric fields inside the reflector. The reflector consists of two plates R1 and R2 with mesh-covered rectangular holes and 18 plates with open rectangular holes. To produce the electric fields in the reflector, voltages V_{R1} = -390 V and V_{R2} = +87 V are applied, and each of the 18 plates is biased using a resistor divider network such that the electric field between R1 and R2 is uniform. The ions entering the reflector encounter a strong decelerating field between the liner and R1, and a weaker electric field between R1 and R2, which turns their trajectory around, and directs them back into the field-free region towards the detector.

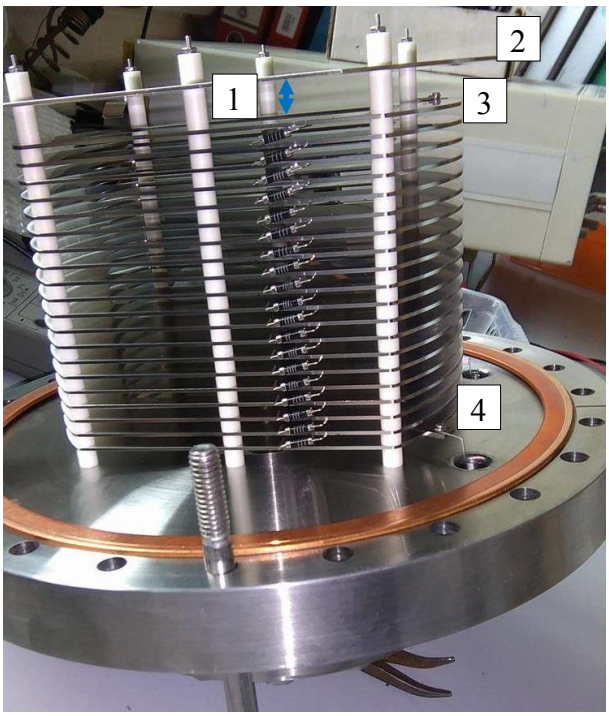

Figure 3.14: The reflector assembly situated in the flight-tube. 1 - Deceleration region, 2 - Liner plate (- 1200 V), 3 - Top plate (- 390 V), 4 - Bottom plate (+ 87 V).

V_{R1} refers to the top plate of the reflector which is held at -390 V, while the bottom plate V_{R2} is held at +87 V. The reflector uses a resistor divider network to apply voltages to a series of equidistant plates mounted between the top plate and the bottom plate (see Figure 3.14) in order to create a homogeneous field. The electric field lessens the flight-time spread of the extracted ions with equal *m/q* value. Ions with an identical *m/q* value may be produced with different kinetic energy in the interaction region and as a result will have slightly different velocities when traversing the flight-tube. The reflector will increase the path distance of the ions that have higher velocities, as they will penetrate further into the electric field before being repelled. The depth of penetration into the electric field is proportional to the kinetic energy of the ion. The reflector directs the ions back into the flight-tube where they enter the microchannel plate detector.

Figure 3.15 shows the inside of the flight-tube. The top aperture joins the collision chamber with the flight-tube. The bottom aperture is the entrance to the microchannel plate detector where the ions are detected.

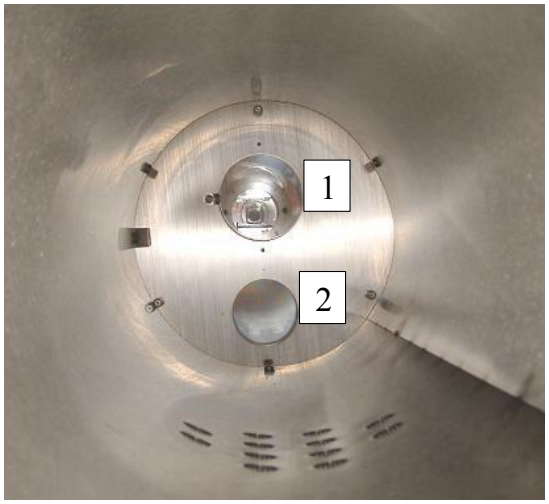

Figure 3.15: Inside of the flight-tube. 1 - Exit from the collision chamber into the flight-tube, 2 - Entrance into the microchannel plate detector.

Once the ions have travelled back through the flight-tube they will strike the microchannel plate detector (MCP) positioned opposite the reflector. The MCP consists of two microchannel plates in chevron configuration mounted in front of a tapered anode. An incident ions will strike one of the microchannels in the top plate of the MCP, releasing secondary electrons that are accelerated through the channel by a potential difference between two plates. Further collisions in the channel result in a small current pulse being produced on the anode, which can be detected using an ORTEC 9327 1-GHz amplifier and timing discriminator (see Section 4.2).

A resistor divider network is used to apply appropriate potential differences across both microchannel plates. For the measurements with 5-fluorouracil, the resistor divider network was supplied with -4200 V, resulting in a voltage of -1848 V on the front of the first plate, a voltage of -1008 V on the back of the first plate and the front of the second plate, and a voltage of -168 V on the back of the second plate. The anode is kept at ground.

Chapter 4

Interfacing, Data Acquisition and Data Analysis

4.1 Introduction

This chapter describes the procedures and software used to acquire mass spectra as a function of electron impact energy and to analyse these mass spectra. A combination of interfacing hardware, LabVIEW programs for data acquisition and data analysis is needed to generate mass spectra and each will be discussed in this chapter.

In this experiment, the main piece of hardware used for data acquisition was the FastComtec 7886S multichannel scaler card (MCS) which is discussed in detail in Section 4.4. Other hardware include an amplifier and timing discriminator (discussed in Section 4.3) and a digital delay generator (discussed in Section 4.4).

The hardware and the software operate together and are used to set a sequence of events. The sequence of events were timed with precision as accurate timing between the hardware and software is of huge importance when collecting data. A Stanford DG535 digital delay generator was used to control the timing sequence and pulsing of the grid, the multichannel scaler card and the various electrostatic lens elements of the system.

4.2 Experimental event sequence

The first step in the sequence was to initiate the electron pulse. Once the electron pulse has stopped, the output extraction pulse was triggered to extract the newly formed ions from the interaction region. Once the ions have been extracted into the flight-tube, the multichannel scaler (MCS) was triggered by sending a pulse to its start input.

Ions are extracted by applying a pulsed voltage to the extraction grids G1 and G2, see Figure 3.12. When the experiment is in operation, G2 is held at ground and G1 is set to +100 V, creating the field that extracts the ions from the interaction region.

In order to obtain accurate results, the electron pulse and the ion extraction pulse must be set to particular time intervals in which to operate. The digital delay generator (Stanford DG535) is used to accurately time the electron pulse and the extraction pulse to extract the ions into the reflectron and trigger the multichannel scaler. A, B, C and D are the delay signal outputs on the delay generator which are triggered relative to T0 that denotes the beginning of the timing cycle. They are generated with remote pulsers and are delayed with respect to each other to ensure no overlap as the induced field within the collision chamber would alter the trajectory of the incoming electron beam, see Figure 4.1. Two remote pulses are used, which are triggered by the AB and CD pulses from the digital delay generator.

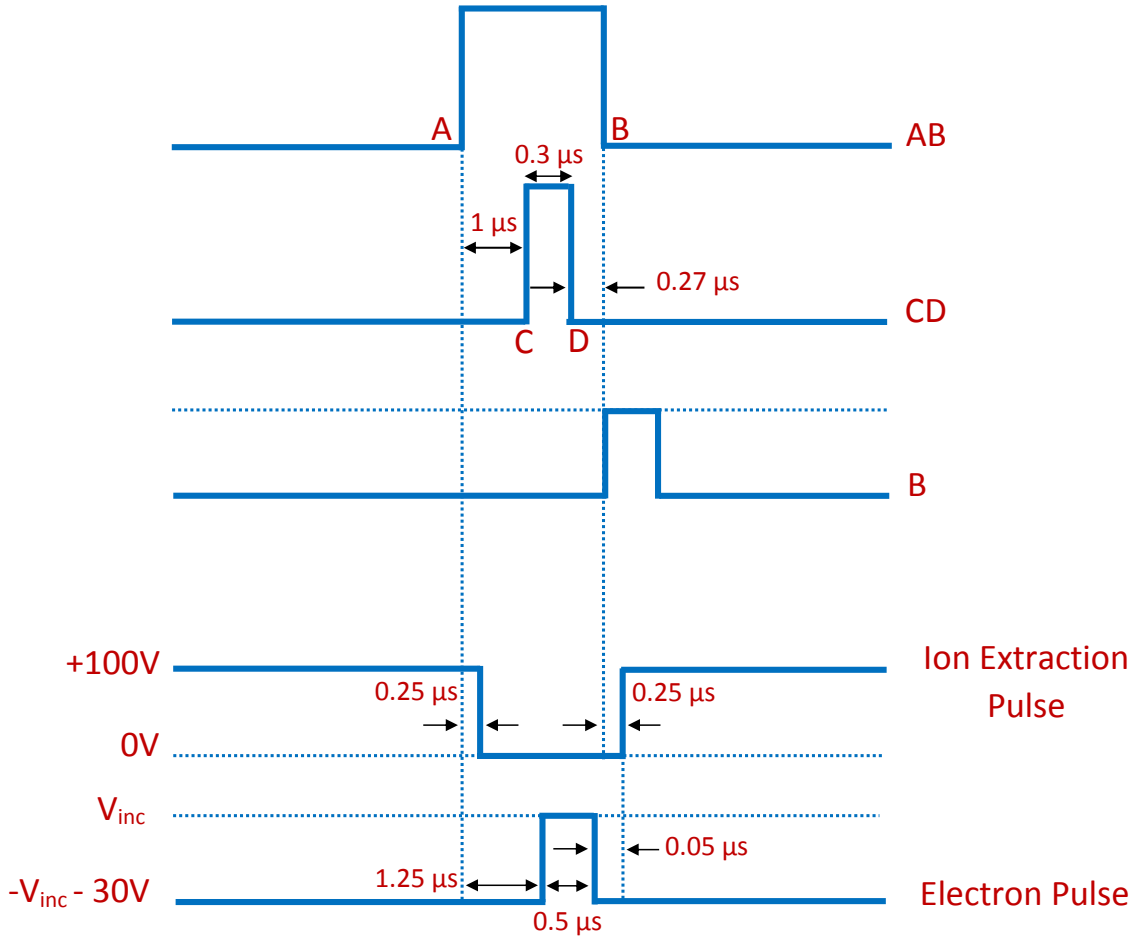

Figure 4.1: Diagram showing the settings for the extraction pulse and the electron gun pulse.

The AB output from the signal delay generator is connected to trigger the ion extraction remote pulser box. The remote pulser requires 12 V to operate its circuit and DC bias voltages that are connected to a pulser power supply. The 12 V supply is connected to G1. Signal AB is sent from the digital delay generator and triggers the extraction remote pulser that is connected to G1, grounding G1 temporarily. The reaction time of the remote pulser causes a delay of 0.25 μs between trigger A and the grounding of the extraction pulse.

Signal CD triggers the electron gun remote pulser box. This electron gun remote pulser box consists of a bias voltage received from a Farnell L30B stabilised power supply, a pulsed voltage from a Farnell E30/2 power supply and 12 V from a pulser power supply. The electron gun remote pulser pulses from -V_{inc} - 30 V to V_{inc}.

The B output of the signal delay generator is connected to an ORTEC EG&G 416A gate and a delay generator. The output of this generator is connected to the START input of the multichannel scaler card (MCS). The MCS used in this experiment is the 7886S manufactured by FAST ComTec.

Figure 4.1 shows the delay between the end of the CD signal and the beginning of the B signal, where B = D + 0.27 μs. The B signal triggers a sweep of the MCS card. The ions that travel through the flight-tube and strike the multichannel plate detector generate a signal that is passed to the STOP input of the MCS stopping the cycle.

Figure 4.1 shows the pulse settings used for the output ion extraction and the output electron gun. Before the start of the electron pulse, the extraction pulse that operates at +100 V, is reduced to ground, eliminating the extraction field inside the interaction region. The potential applied to G1 is set for most of the cycle to reduce background in our mass spectra. It is only switched off when the electron pulse is being triggered. The output electron pulse is started 1 μs after the output extraction pulse has been re-set to ground. The duration of this electron pulse is set to 0.5 μs during which time the electron beam ionises the molecules. The output extraction pulse is re-initiated to +100 V, 0.05 μs after the grounding of the electron pulse, resulting in the extraction of the newly formed ions into the flight-tube. This delay of 0.05 μs is minimised to ensure no ions escape from the interaction region before being extracted. This also slightly improves the mass resolution.

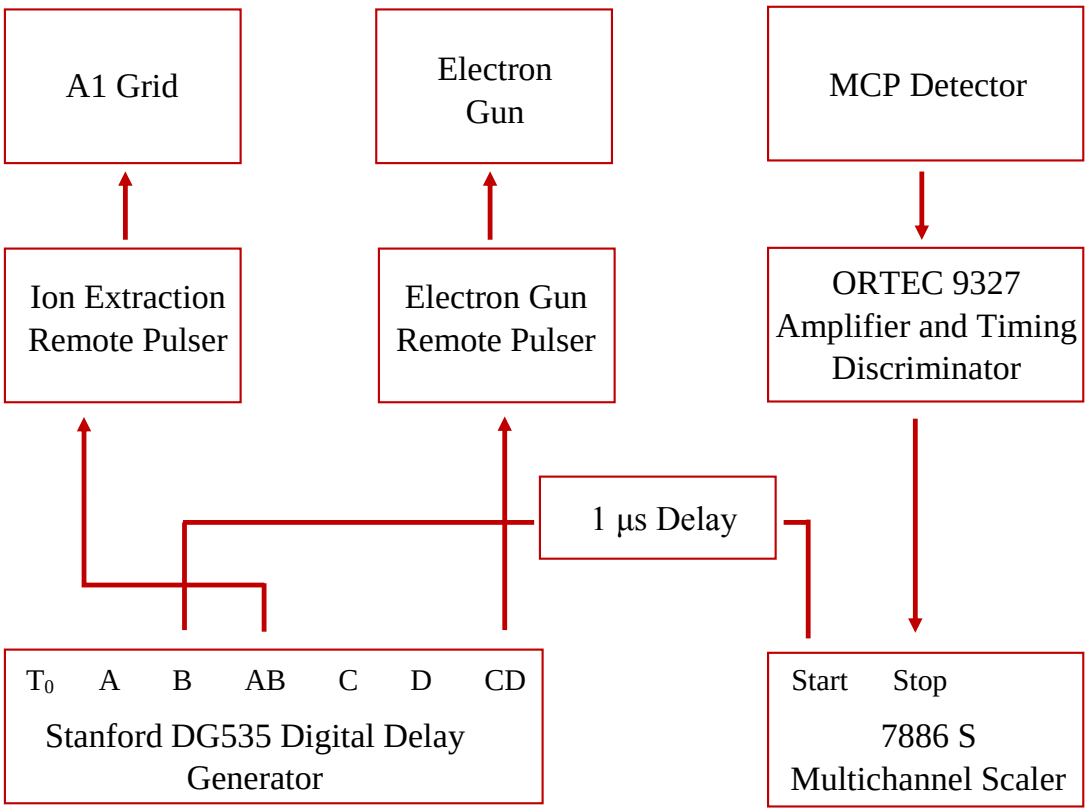

Figure 4.2: Pulsing arrangement for the DG535 digital delay generator.

Figure 4.2 show the pulsing set up of the Stanford DG535 digital delay generator. It shows that the output signal AB triggers the output extraction remote pulser while the output signal CD triggers the electron gun remote pulser, see Section 4.2. An ORTEC 416A gate and delay generator were used to delay the multichannel scaler start by 1 μs.

Figure 4.2 also shows the connections needed for the detection of pulses, which is described in the next two paragraphs.

4.3 Amplification and discrimination of detector pulses

When an ion is detected by the multichannel plate detector (MCP), the MCP produces a current pulse that needs to be amplified and discriminated before the data acquisition can commence at the MCS card. The signal is sent to an ORTEC 9327 1-GHz amplifier and timing discriminator, which produces a NIM logical pulse whenever the current pulse exceeds the discriminator level. The ORTEC 9327 has a 1-GHz bandwidth that minimises

the noise and rise time contributions to timing jitter on the detector pulses. The device has a 15-turn potentiometer to control the discriminator level, and a LED on the front flashes whenever a pulse exceeds the discrimination level. The optimum discriminator level was determined by monitoring the background signal between the peaks in the mass spectra, and the value used was -0.0247 V.

4.4 Multichannel scaler

In this experiment, data acquisition was carried out using a FastComtec 7886S multichannel scaler. It was used to accumulate time-of-flight spectra. The 7886S multichannel scaler card is capable of accepting one event per channel and can handle up to 2-GHz of peak count rates. It has a dynamic range of up to 2^{37} channels, which enables sweeps of 68.7 s with a time resolution of 430 ps per channel. All of the mass spectra were recorded with a bin width of 64 channels (effective resolution of 27.55 ns) and a range of 2023 bins (total range of 55.7 μs). The multichannel scaler card is LabVIEW controlled. Within the LabVIEW program we can initialise the MCS card and also specify the bin width and time range. The bin width can be set in powers of 2 up to 16,384 channels.

The multichannel scaler card has the following inputs and outputs: START IN, STOP IN, ABORT IN, SYNC OUT, DIGITAL IN and a THRESHOLD adjust potentiometer. Output B of the digital delay generator is connected to the START IN of the MCS via the gate and delay generator that delays the signal by 1 μs. A sweep of the MCS begins when the signal from output B of the digital delay generator arrives at the START IN input of the MCS as seen in Figure 4.2. The multichannel plate detector is connected to the input of the ORTEC 9327 amplifier and discriminator. The NIM OUT output of the 9327 device is connected to the STOP IN input of the multichannel scaler card, so that the signal from the detector can be registered as a count at the relevant binning location of the MCS.

4.4.1 Calibration of the multichannel scaler

The multichannel scaler card was calibrated to find the length of time for one channel. The MCS utilizes a phase-locked loop (PLL) oscillator that is set to at least 1.8 GHz resulting in an assured time resolution of less than 500 ps per channel. This frequency can vary so the time per channel was calibrated using the Stanford digital delay generator as an

external reference. The time delays for the output pulses of this device can be set with 5 ps resolution. The digital delay generator sent a start and stop pulse to the multichannel scaler card with a fixed delay. The delay between the pulses incremented by 5 μs from a minimum value of 5 μs up to a maximum of 60 μs. The corresponding channel number was recorded with each 5 μs incremental delay as shown in Figure 4.3.

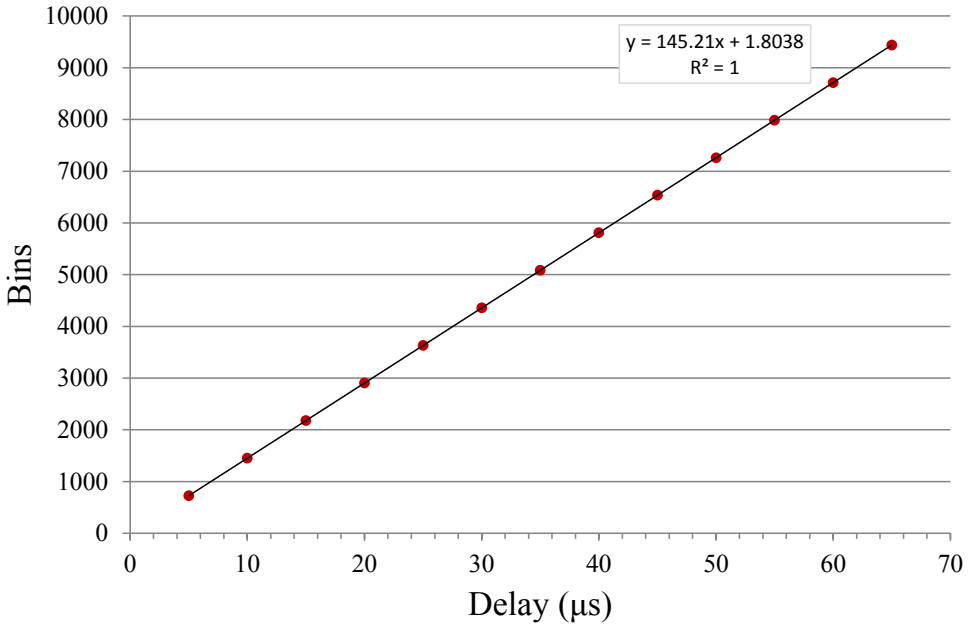

Figure 4.3: Calibration graph of the multichannel scaler card.

Figure 4.3 shows a graph of the number of bins versus the delay time (μs). A best fit trendline was fitted through these data that yielded a slope of 145.2003 $\pm$ 0.0002 bins per μs. For this calibration, a bin width of 16 channels was used. Using this information we calculated the calibration constant (dwell time) to be 430.4400 $\pm$ 0.0005 ps per channel. This is in good agreement with previous calculations.

4.4.2 LabVIEW control of the multichannel scaler

In this experiment, the multichannel scaler (MCS) card was controlled using LabVIEW code. LabVIEW is able to interact with the MCS card by using dynamic link library (DLL) files. These DLL files were written in C code by Dr. Marcin Gradziel, and are modified versions of the DLL files provided by FASTComTec. The DLL files are accessed within LabVIEW by using two Call Library Function Nodes. The first node is used to

check whether the MCS card is correctly initialised, and the second node is used to access the data accumulated by the MCS card (for more information see Barrett [2008]).

4.5 Data acquisition

4.5.1 Measurement of single mass spectra

Two different LabVIEW based programs were used to acquire mass spectra in this experiment. The first program was called *getspectrum-3-5.vi* (developed by Dr. Peter van der Burgt and Dr. Marcin Gradziel), and was used to measure single mass spectra in real-time. The data from the multichannel scaler card was recorded by the *getspectrum-3-5.vi* program and displayed on a graph in real-time. The prime focus of the *getspectrum-3-5.vi* program was to measure a single mass spectrum so that it could be assessed before the experiment was initiated to carried out multiple time-of-flight scans.

Figure 4.4 is a screen shot of the front panel from the *getspectrum-3-5.vi* program. The screen shot was taken during earlier measurements and shows a mass spectrum of cytosine. The control structure used in this program was a standard state structure and it uses two different nodes to produce a single mass spectrum. The user determines appropriate values for the time range, bin width and other variables, and inputs them on the front panel of the program, as seen in Figure 4.4.

Some of the controls on the front panel include the *Start, Stop, Continue* and *Save* controls. The *Start* control initiates the acquisition of a mass spectrum while the *Stop* control stops the data acquisition. The *Save* control is used to save the data containing current mass spectrum into a text file for further analysis.

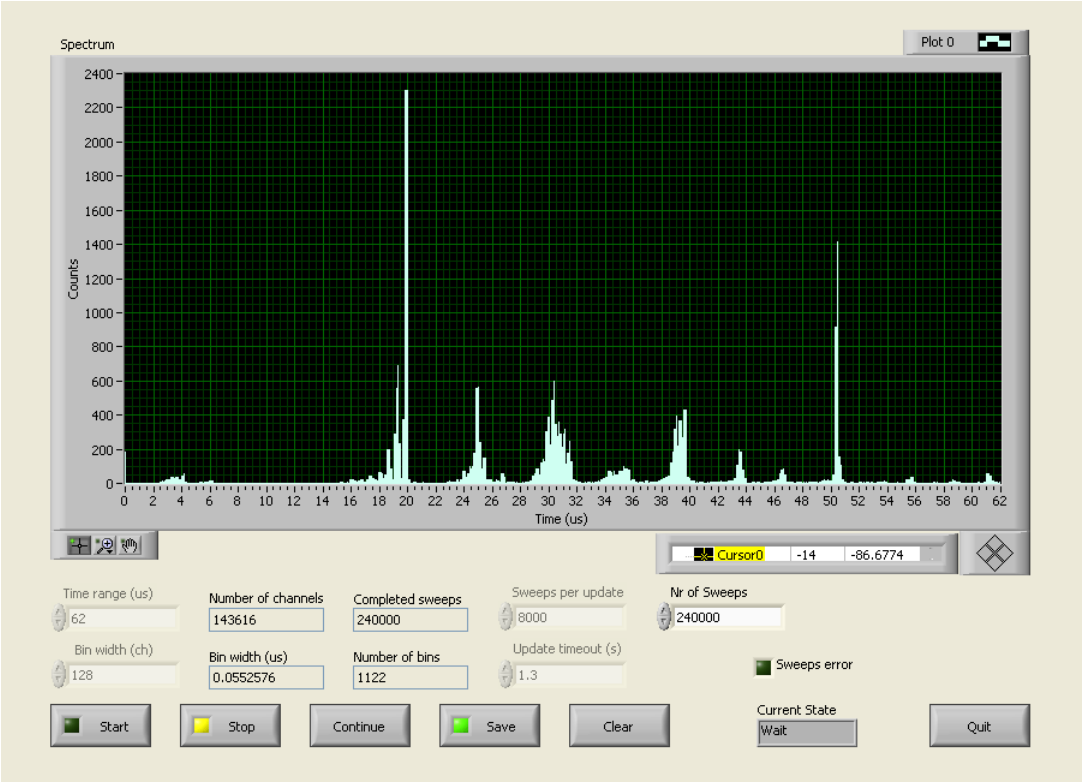

Figure 4.4: The front panel of the *getspectrum-3-5.vi* program. (This mass spectrum belongs to cytosine).

4.5.2 Measurement of mass spectra as a function of electron impact energy

The LabVIEW program that was used for the measurement of mass spectra as a function of electron impact energy was called *Spectra-vs-E-v7.vi*, developed by Barrett [2008]. This program ramps the electron impact energy in 0.25 eV steps from 5 eV to 100 eV, acquires a mass spectrum at each electron impact energy, and adds that mass spectrum to the data already accumulated in the appropriate place in the full data set. The full data set consists of a two-dimensional array of ion yields as a function of time-of-flight and as a function of electron impact energy. After each cycle, which is a single loop through the specified range of electron impact energies taking about two hours, the full data set is written to a file. The data set used for this thesis consists of 10 cycles of the electron impact energy.

Figure 4.5 shows the front panel of the *Spectra-vs-E-v7.vi* program, (showing a mass spectrum of cytosine from a past measurement). As can be seen, there are many controls and indicators on the front panel. Some of these controls include: the starting and ending

electron impact energy, the value with which to increment, the number of cycles, and the bin width and time range. The top of Figure 4.5 shows a small part of the two-dimensional array of ion yields called Spectrum Array holding the accumulated mass spectra.

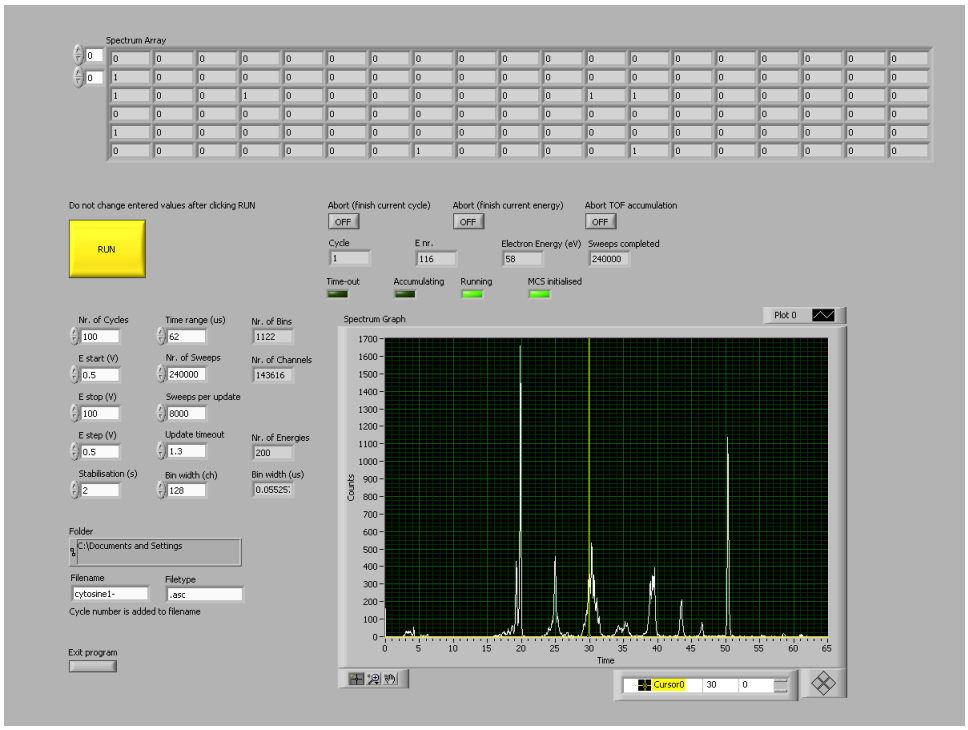

Figure 4.5: An image of the front panel from the *Spectra-vs-E-v7.vi* program. (This mass spectrum of cytosine was produced when the electron impact energy was 58 eV).

The *Spectra-vs-E-v7.vi* program operates using three nested loops. The first loop will continue running until it has reached the maximum number of cycles specified, or until the user aborts the data acquisition. The second loop operates the data acquisition for a single cycle, covering the full range of electron impact energies. The third loop is in relation to the number of times the multichannel scaler sweeps over the full range of masses, which is equal to the number of electron pulses used to accumulate a single mass spectrum. For 5-fluorouracil, the number of sweeps was set to 240,000, indicating that 240,000 sweeps are completed for each mass spectrum. Using an electron pulse rate of 8 kHz this takes 30 s.

Because the full data set is written to a file every time a cycle is completed, mass spectra obtained after each cycle can be examined, and it has been verified that no undesired effects occurred during the collection of the data for 5-fluorouracil.

4.6 Data analysis

4.6.1 Gaussian peak fitting

A Gaussian fitting program called Gaussians2.vi was developed by Dr. Peter van der Burgt to fit groups of adjacent peaks in the mass spectra with a sequence of normalised Gaussians. The formula was of the form:

$$f(x) = \Sigma_{i=1}^{n} \frac{C_i}{a\sqrt{\pi}} exp\left(- \left(\frac{x - p - \delta_i}{a} \right)^2 \right) + B \tag{4.1}$$

where C is the peak area, p is the position of the largest peak in the group, a is the width of the peak, B is the background and δ_i is the difference between the largest peak and each of the other peaks in the group. The values of δ_i are kept fixed during the fitting, and are evaluated based on the mass calibration.

The program uses the Levenberg-Marquardt algorithm available in LabVIEW to determine the best fit. The program allows the user to change initial values, until the best fit for the group of peaks in the mass spectrum at the highest electron energy is obtained, and then this group is fitted successively for all mass spectra at all electron energies from 100 to 5 eV. At each step, the best fit values obtained for the previous electron energy are used as starting values for the next electron energy.

For several groups of peaks it was found that not all of the peaks had the same width. For this purpose a second version of the program was developed, called *Gaussians2ab.vi*, in which one or more peaks within the range of peaks to be fitted could be given a different width b.

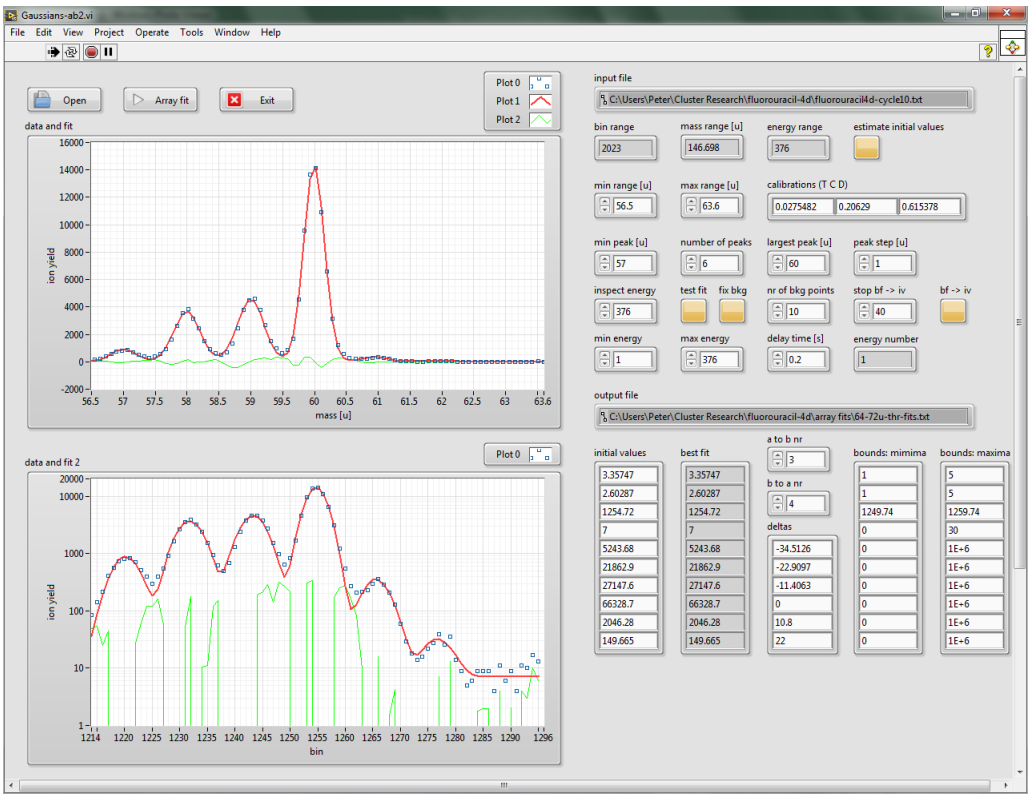

Figure 4.6: Front panel screen shot of *Gaussians-ab2.vi* (57 u - 62 u group).

Figure 4.6 shows a front panel screen shot of the *Gaussians-ab2.vi* program being used for the 57 u - 62 u group. In this case the peaks at 57 u, 58 u and 59 u had width a and the peak at 60 u had width b and finally, peaks 61 u and 62 u had width a. The grey box in Figure 4.6 shows the best fit for energy number 376 (corresponding to 101 eV), showing the values for a, b, p, B, C_1, C_2, C_3 and C_4.

This program asks the user to enter a minimum and maximum peak range, and the number of peaks to be fitted within this specified range. This allows the program to scale the mass spectrum such that it only displays the range specified allowing clear visualisation when adjusting the initial parameters array to achieve the model that best fits the data. The initial parameters array includes: the number of background points, the width of the peaks, the count of the peak and the model functions position along the mass axis (delta values). The size of the array will change depending on the number of peaks to be fitted. The bottom graph is a logarithmic representation of the above graph. This effectively acts as a zoom in function, allowing for better initial parameters. It also helps to set an accurate background value. There is a 'test fit' button allowing the user to check the fit for a single electron energy without running the program for the full range of electron energies.

In several cases, problems with convergence of the fits were encountered at low electron energies. In these cases, the number of peaks was reduced, or the peak width a and the position of the largest peak p were both set to a fixed value, and the fitting was repeated over a smaller range of electron energies near threshold. The fits over the full energy range and over the smaller energy range were then compared and combined in Excel, to obtain a set of ion yield curves.

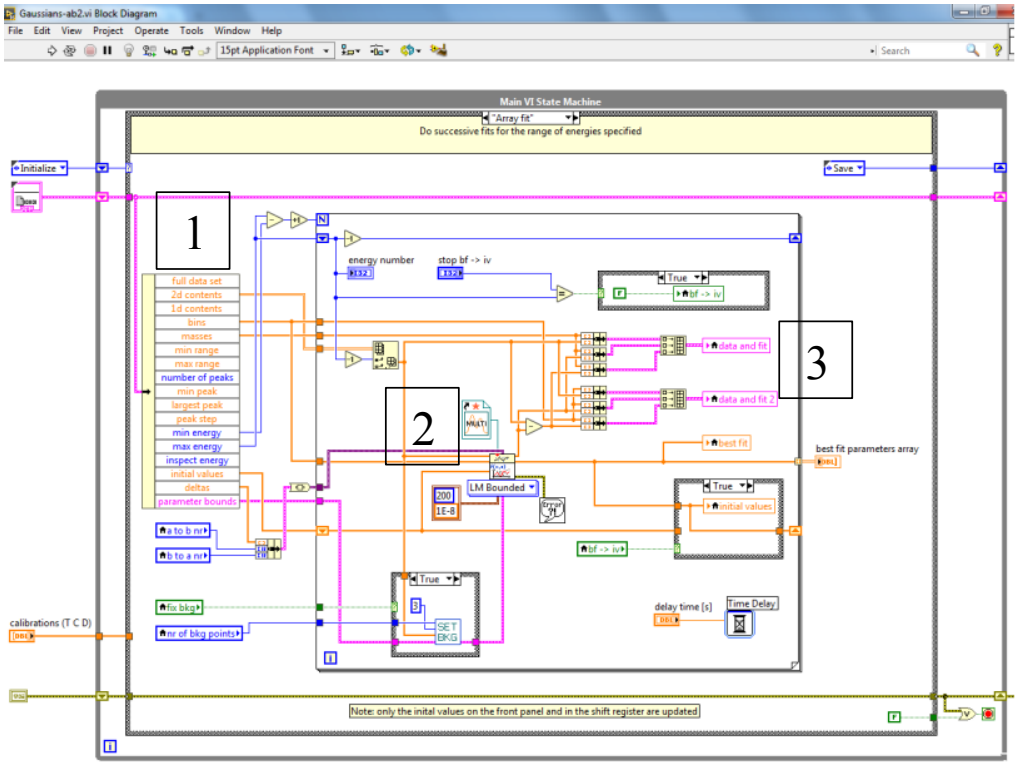

Figure 4.7: Block diagram screen shot of *Gaussians-ab2.vi* program. 1) Arrays and integers, 2) Levenberg-Marquardt fitting algorithm and 3) The two graphs as seen in Figure 4.6.

Figure 4.7 shows part of the block diagram of the *Gaussians-ab2.vi* program. Below the label 1 in Figure 4.7 is a list of various arrays and integers used in the program. Some of these arrays and integers include: the number of peaks specified in the program, the minimum and maximum electron energy, and the initial parameters. It can be seen that the initial parameters are sent into the Levenberg-Marquardt fitting algorithm, situated at label 2 in Figure 4.7. To the left of label 3 is where the two graphs in Figure 4.6 can be

found.

The Levenberg-Marquardt algorithm and both graphs are positioned inside a while loop. The while loop forces the program to fit to the data at every electron energy, which will cause the graphs on the front panel to update, enabling real-time analysis. The energy range through which the program runs is specified on the front panel, and this value is sent into the while loop, as can be seen in Figure 4.7.

4.6.2 Determining appearance energies

To determine the appearance energy and possibly one or two higher onsets in the ion yield of each fragment, a LabVIEW program called *Onsets.vi* was developed by Dr. Peter van der Burgt. This program uses the Levenberg-Marquardt algorithm to fit an onset function convoluted with a Gaussian function to a section of the ion yield curve near threshold.

$$P(E) = \Sigma_{-\infty}^{\infty} f(\varepsilon)\, g(E-\varepsilon)\, d\varepsilon + b \tag{4.2}$$

Equation 4.2 shows the onset function $f(\varepsilon)$ convoluted with the Gaussian function $g(\varepsilon)$.

$$f(\varepsilon) = 0 \qquad \text{if } \varepsilon \leq E_0 \tag{4.3}$$

$$f(\varepsilon) = c(\varepsilon - E_0)^p \qquad \text{if } \varepsilon > E_0 \tag{4.4}$$

$$g(\varepsilon) = \frac{1}{\sigma\sqrt{\pi}} \exp\left(-\frac{\varepsilon^2}{\sigma^2} \right) \tag{4.5}$$

In these equations ε is the incident energy, and the fitting parameters are the background b, the power p, the scaling factor c, and the appearance energy E_0. σ is the Gaussian beam width that is fixed at 0.48, corresponding to an electron beam width of 0.8 eV FWHM.

In case the ion yield curve shows a second onset, equation 4.4 is modified to:

$$f(\varepsilon) = c_1(\varepsilon - E_0)^{p_1} + c_2(\varepsilon - E_1)^{p_2} + b \qquad if \quad \varepsilon > E_1 \tag{4.6}$$

In case there is a third onset, another term $c_3(\varepsilon - E_2)^{p_2}$ is added.

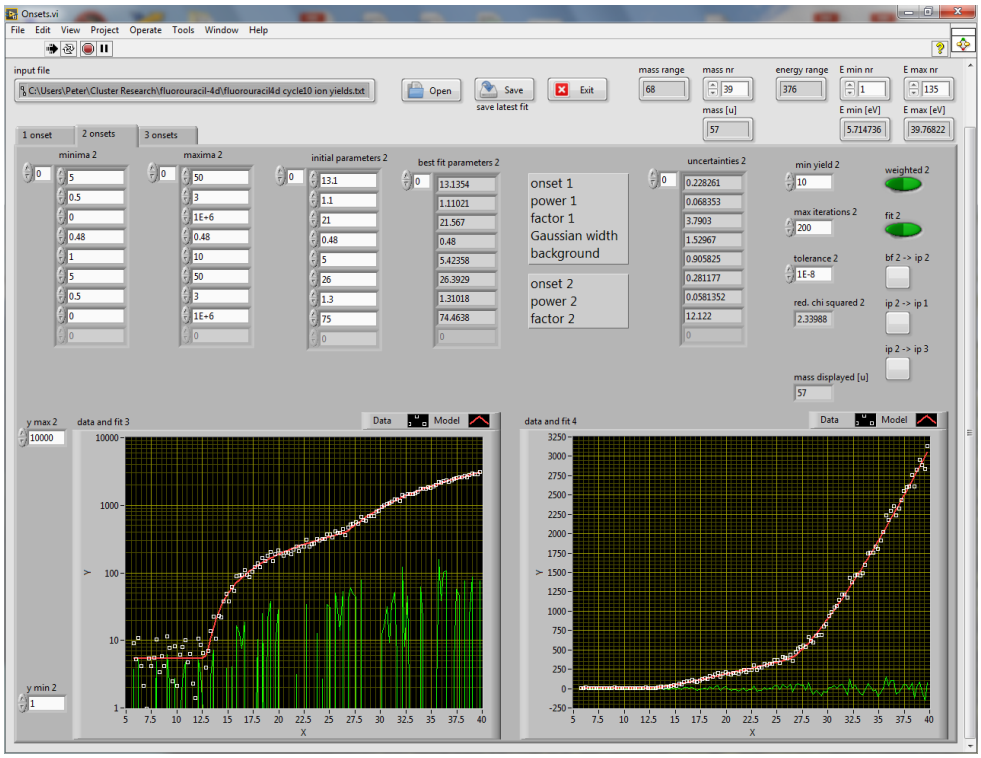

Figure 4.8: Front panel of the Onsets.vi program used to determine the appearance energy of 57 u fragment at 13.1 $\pm$ 0.2 eV, and a second onset at 26.4 $\pm$ 0.3 eV.

Figure 4.8 shows the front panel of the *Onsets.vi* program displaying an ion yield curve that has a second onset. A graph with a linear scale and a graph with a logarithmic scale are displayed to enable the user to judge the quality of the fit. The program is supplied with a text file, in which the first row contains the electron energies, and the subsequent rows contain the ion yields of all the fragments for which ion yields have been obtained using the Gaussian peak fitting. On the front panel, the user is able to select a specific fragment (mass nr in Figure 4.8) and the energy interval (E min nr and E max nr) over which the fitting is to be done. The tab structure allows the user to choose whether to fit an onset function with a single appearance energy or an onset function with one or two additional onsets. The user has to provide suitable values for the initial parameters to commence the fit. If the fit converges, the program displays the fit result in the graphs and shows the best fit parameters. If the fit does not converge a toggle switch (fit 2 in Figure 4.8) turns red and the graphs show the onset function calculated using the initial parameters. The user then has to select better values for the initial parameters and has to press the toggle switch to see whether the fit converges.

Chapter 5

Electron Impact Fragmentation of 5-Fluorouracil

5.1 Introduction

This chapter presents the new results obtained for 5-fluorouracil. These results include: Gaussian peak fit results for the various groups within the mass spectrum alongside their corresponding ion yield curves and the appearance energy results for most fragments. Possible fragmentation processes producing the obtained ions are also discussed. All measurements in this section were taken over an electron impact energy range of 5.71 - 101.01 eV in 0.25 eV steps using the procedure discussed in Section 3.3.1. 10 cycles were measured in total for the final data. Assuming that the detection efficiency of the reflectron time-of-flight mass spectrometer is mass independent, all of the measured ion yield curves are on the same relative scale allowing them to be compared.

Section 5.2 presents the mass spectra of 5-fluorouracil at four different electron energies, and compares these with the corresponding mass spectra of uracil.

Section 5.3 presents the Gaussian fits of the groups of positively ionised fragments of 5-fluorouracil, and the resulting ion yield curves. The Gaussian fit images show the individual Gaussians for all fragments in the group, with a superimposed sum of fits that best models that data. Ion yield curves were generated using the Gaussian peak fitting program *Gaussians-ab2.vi* as discussed in Section 4.6.1.

The appearance energies obtained for most 5-fluorouracil fragments are presented in Section 5.4. The appearance energies were determined by fitting an onset function to the threshold region of the ion yield curves near threshold, using the *Onsets.vi* fitting program as discussed in Section 4.6.2. Section 5.4 will also include appearance energy results for various molecules including: 5-chlorouracil, 6-chlorouracil, 5-bromouracil and uracil that were used for comparison.

Section 5.5 discusses the fragmentation pathways for a selection of fragments of 5-fluorouracil and these are compared with the pathways for corresponding fragments of uracil. Chosen fragments are stated as well as images that show the configuration and fragmentation pattern of particular fragments.

5.2 Mass spectra

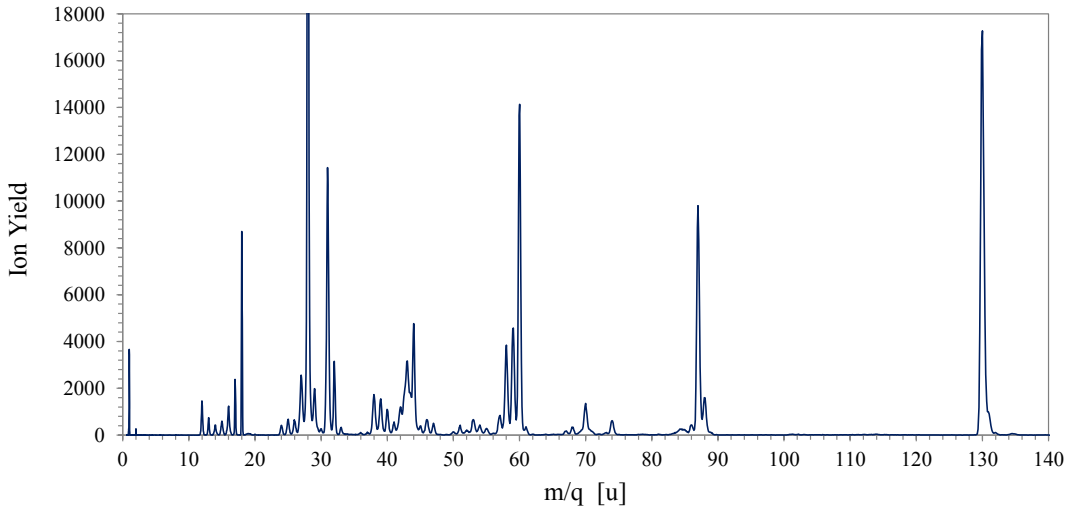

Figure 5.1: 5-fluorouracil mass spectrum at an electron impact energy of 101 eV.

Figure 5.1 shows the mass spectrum of 5-fluorouracil at an electron impact energy of 101 eV. Figure 5.2 shows a superimposed image of the mass spectra of uracil and 5-fluorouracil. (The uracil mass spectrum was measured shortly after the data set for 5-fluorouracil was obtained.)

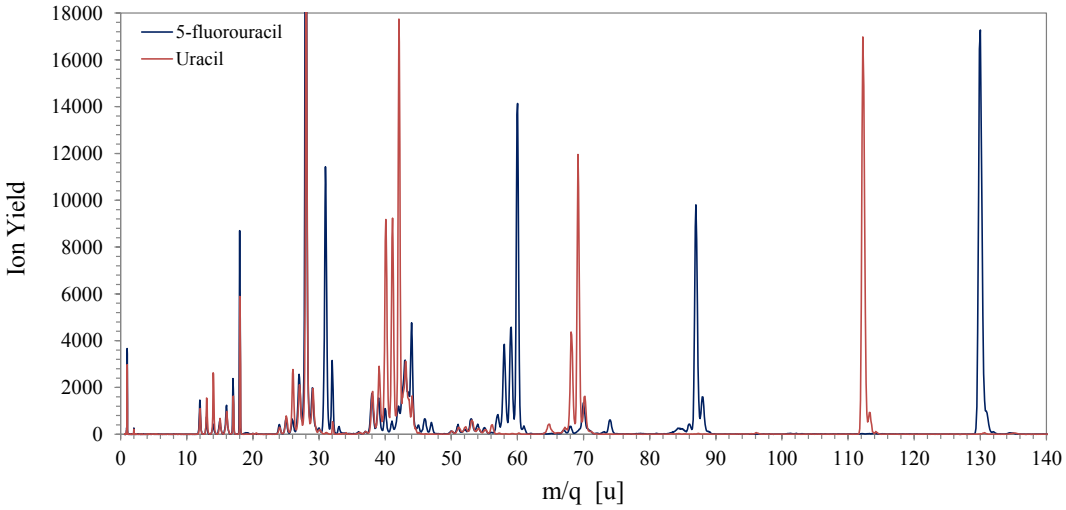

Figure 5.2: Superimposed mass spectra of 5-fluorouracil and uracil at an electron impact energy of 101 eV.

Figure 5.2 provides a comparison between corresponding fragmentations with their relative abundance. It was also used to view the overlapping peaks so that we could determine which group of 5-fluorouracil peaks did not contain the fluorine atom. Series of overlapping peaks indicate groups of fragments that have the same configuration, whereas groups of peaks that have similar yields but are 18 u apart indicate corresponding fragments for which the 5-fluorouracil fragment contains a fluorine atom.

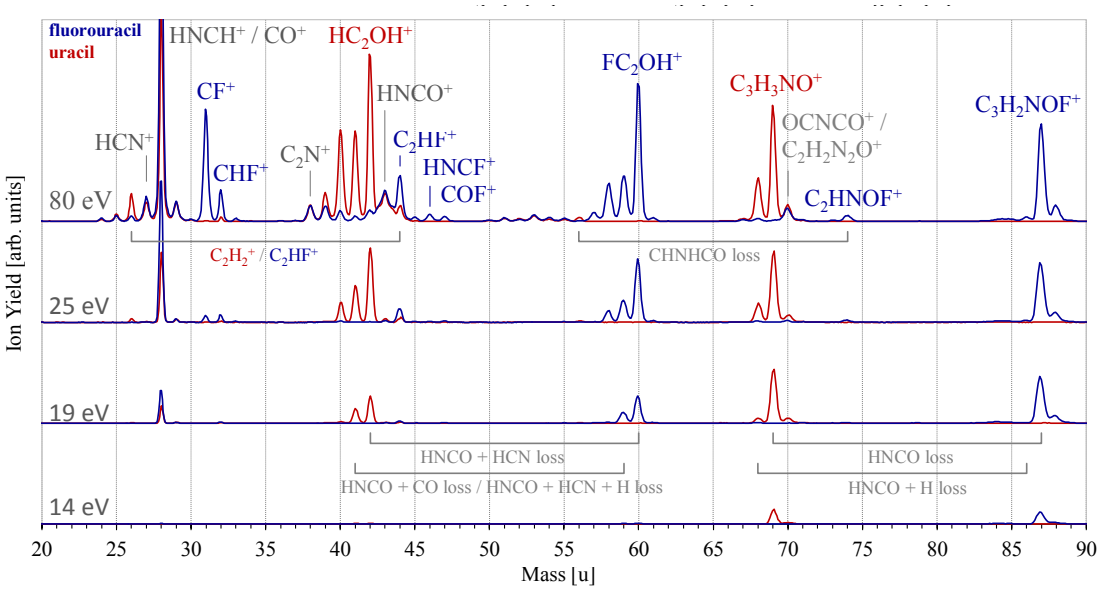

Figure 5.3: Superimposed mass spectrum of 5-fluorouracil and uracil at 4 different electron impact energies.

Figure 5.3 shows four mass spectra of 5-fluorouracil and uracil at four different electron

impact energies. The two parent ions are excluded from all spectra in this image. The molecular formula for various fragments is stated above their corresponding peak. The molecular formulas that are stated in blue represent 5-fluorouracil fragments and the molecular formulas stated in red represent uracil fragments. Corresponding fragments that are 18 u apart are indicated with grey lines.

Apart from the parent ions, the 87 u ion and the 69 u ion are the only two fragments produced at an electron impact energy of 14 eV, see Figure 5.3. Further corresponding groups of peaks between 5-fluorouracil and uracil can be seen at higher electron impact energies.

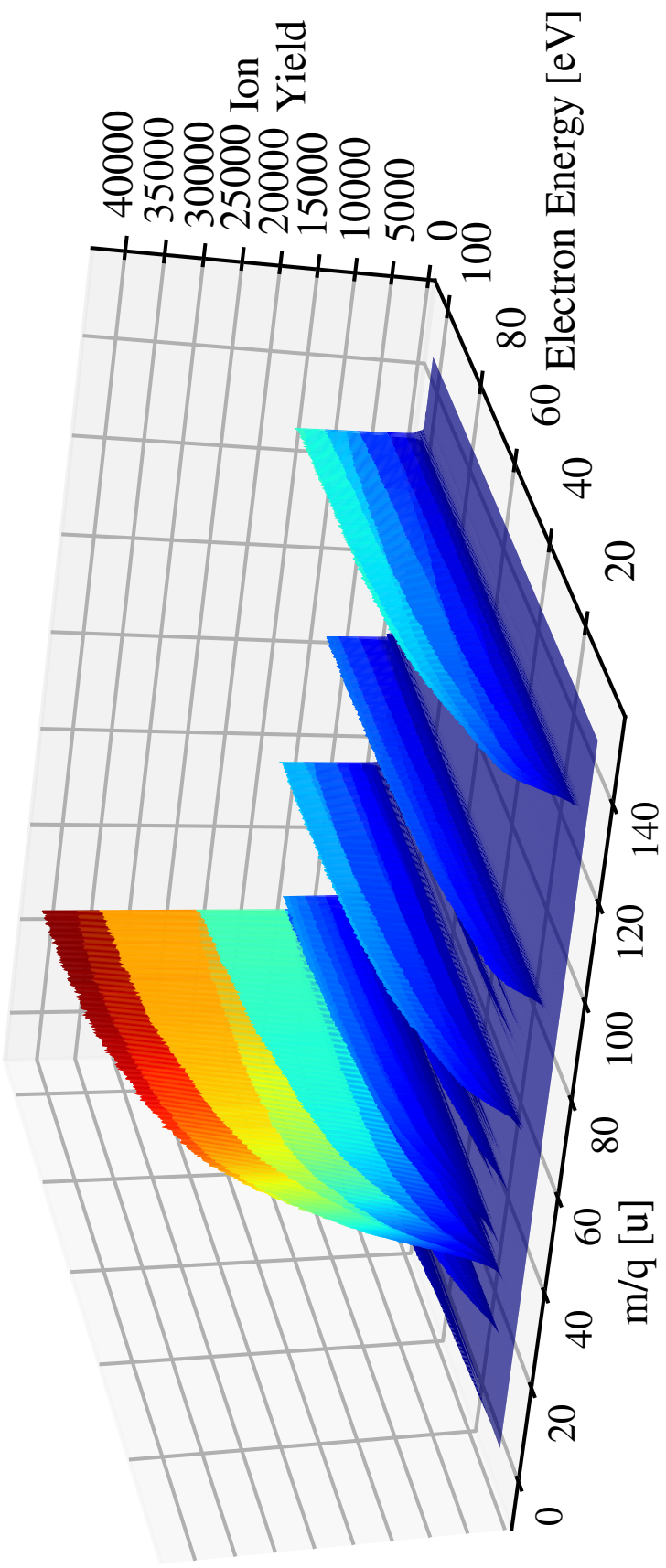

Figure 5.4: 3D image of the mass spectrum of 5-fluorouracil.

Figure 5.4 is a 3D image of the mass spectrum of 5-fluorouracil taken over the full energy range of 5.71 - 101.01 eV. This figure was generated using the Python code in Appendix A. Figure 5.4 can be used as a visual tool to estimate the energies at which fragments appear in the mass spectrum (by locating the position where the count starts to increase from zero).

The most abundant fragment in this experiment was the 28 u ion. The second most abundant fragment was the 130 u parent ion with an ion count of approximately 16500. There is a very weak peak at 131 u and an even weaker peak at 132 u and these are attributed to 5-fluorouracil isotopes, containing one or two isotopes of the constituent atoms. The 87 u has a very high yield and is the fifth most abundant fragment in the spectrum.

Figure 5.2 shows how the 87 u in the 5-fluorouracil data corresponds perfectly to the 69 u fragment in uracil. This shift of 18 u can be accounted for by exchanging a hydrogen atom from a uracil molecule, and replacing it with a fluorine atom. The peak at 60 u is the third largest peak in the 5-fluorouracil spectrum. The 57 - 61 u group of peaks correspond to the 39 - 43 u group in the uracil mass spectrum. The overlap of the 26 - 30 u groups in Figure 5.2 implies that these fragments do not contain the fluorine atom.

5.3 Gaussian peak fitting

5.3.1 130 - 132 u group

Figure 5.5 shows the 130 - 132 u group of peaks in the mass spectrum at 101 eV and compares the model fit (red line) with the data from the ion yield (blue squares). The fit with Gaussians was done with 4 peaks for 130 - 133 u and ion yield data from 127.0 u to 133.5 u. The ion yield curves for the 130 - 132 u ions are shown in Figure 5.6.

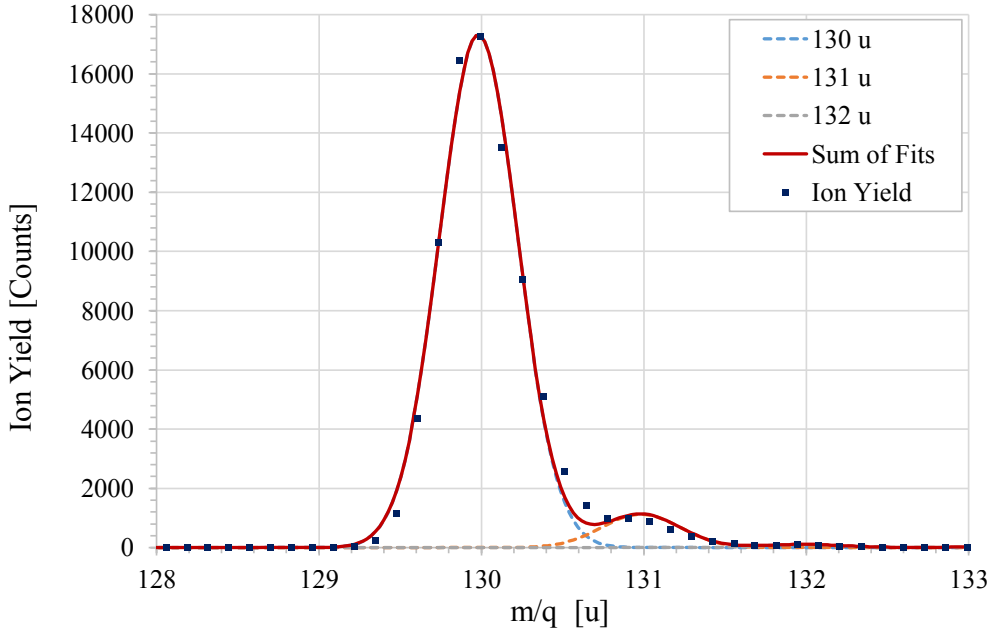

Figure 5.5: Comparison between the Gaussian peak fitting results and the measured ion yields at 101 eV for the 130 - 132 u group.

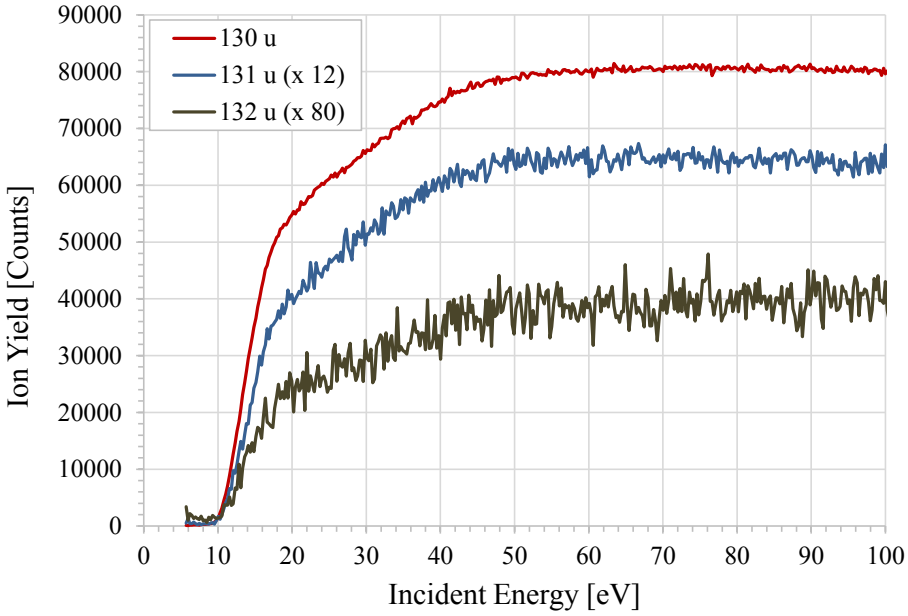

Figure 5.6: Ion yield curves for the 130, 131 and 132 u.

The 130 u is the parent ion and has the second highest yield behind the 28 u, as seen in Figure 5.1. The 131 u and 132 u are due to isotopes and therefore the ion yield curves have the same shape. The 131 u: 130 u ratio is 0.067. The multiplication factors allow

for a comparison of the shape of the ion yield curves over the full range of energies. The ion yield curves for all three masses exhibit the same shape over the full range of electron impact energy, as seen in Figure 5.6.

5.3.2 86 - 88 u group

Figure 5.7 shows the 86 - 88 u group of peaks in the mass spectrum at 101 eV and compares the model fit (red line) with the data from the ion yield (blue squares). The fit with Gaussians was done with 6 peaks for 85 - 90 u and ion yield data from 84.8 u to 92.1 u. The ion yield curves for the three masses with the highest yields are shown in Figure 5.8. The 87 u peak is the largest peak in the group and one of the most abundant fragments in the mass spectrum. 89 u is the same fragment as 88 u, but originating from an isotope of 5-fluorouracil. (Multiplication factors of 12 and 4 were applied to the 86 u and 88 u data, respectively.) Below 85 u there is an increased background that does not show clear peaks. 85 u was included in the fit to improve the fit of the 86 u peak. The rise in the 86 u ion yield between 12 and 18 eV is attributed to a rising background (perhaps due to metastable decay), and the second onset in the 86 u ion yield curve at 17.8 $\pm$ 0.3 eV is taken as the appearance energy of this fragment. A further discussion of the appearance energies is given in Section 5.4.

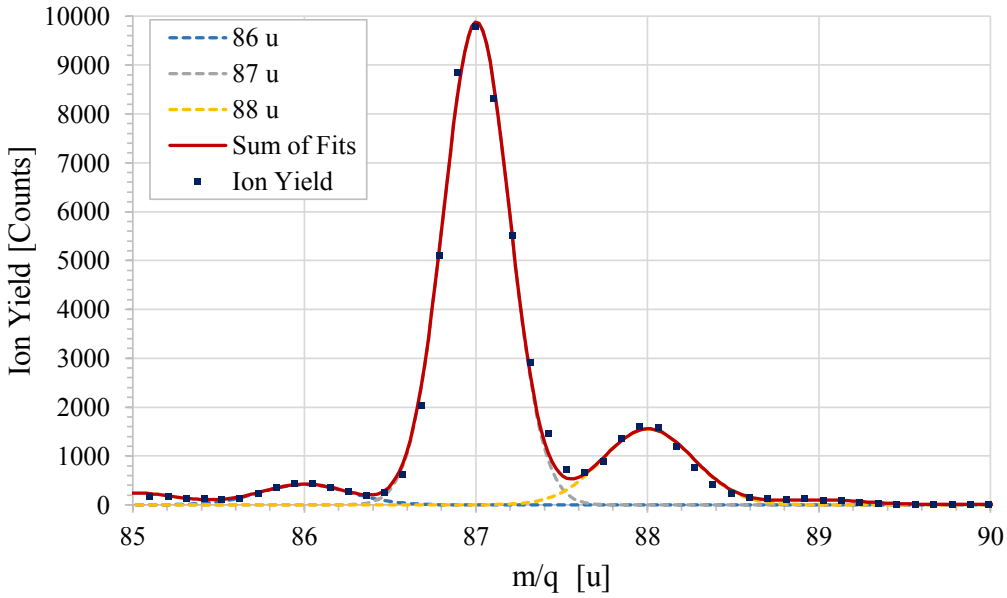

Figure 5.7: Comparison between the Gaussian peak fitting results and the measured ion yields at 101 eV for the 86 - 88 u group.

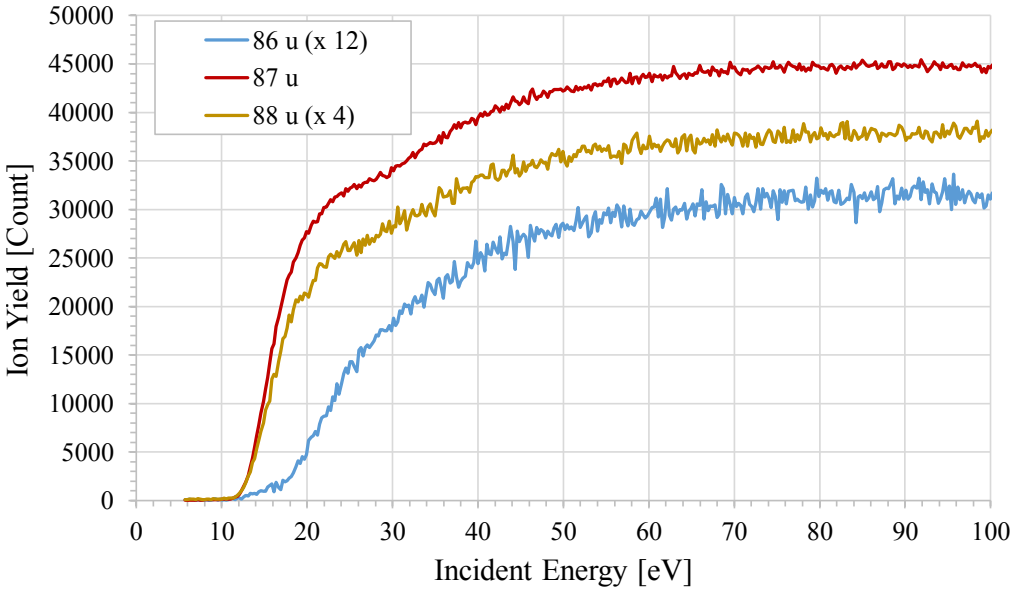

Figure 5.8: Ion yield curves for the 86, 87 and 88 u.

The 88 u:87 u yield ratio is constant above 30 eV and equal to 0.21. The 86 u:87 u yield ratio is constant above 50 eV and is equal to 0.058. This indicates that these ions are produced by similar fragmentation processes, which are discussed in Section 5.5.2.

5.3.3 72 - 75 u group

Figure 5.9 shows the 72 - 75 u group of peaks in the mass spectrum at 101 eV and compares the model fit (red line) with the data from the ion yield (blue squares). The ion yield curves for each mass are shown in Figure 5.10. In comparison with the previous three groups of peaks, the 72 - 75 u group is a weak group with low ion yields. For this reason, only the 73 u and 74 u fragments will be considered in the discussion of fragmentations in Section 5.5.3.

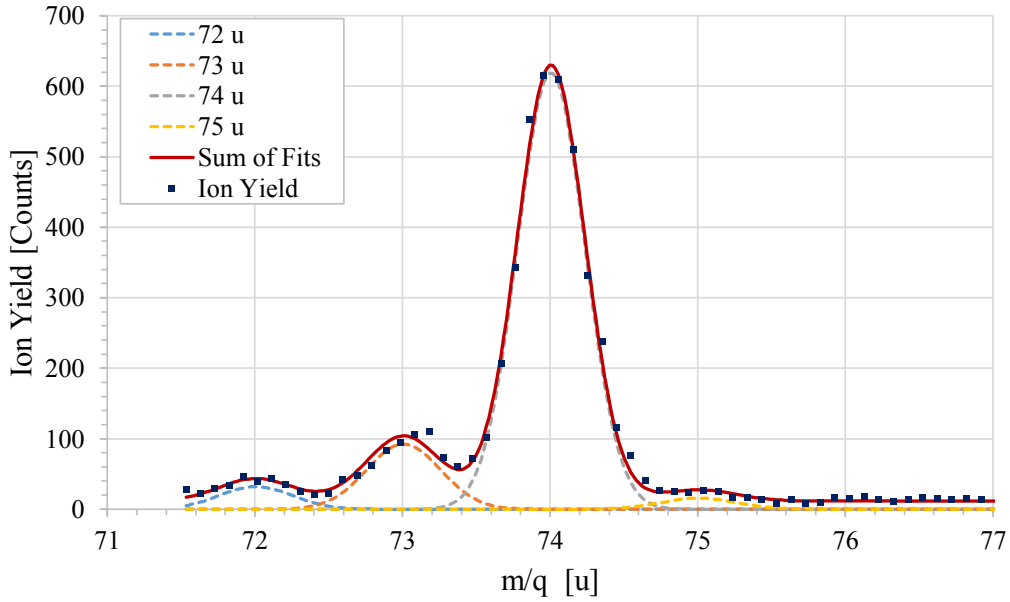

Figure 5.9: Comparison between the Gaussian peak fitting results and the measured ion yields at 101 eV for the 72 - 75 u group.

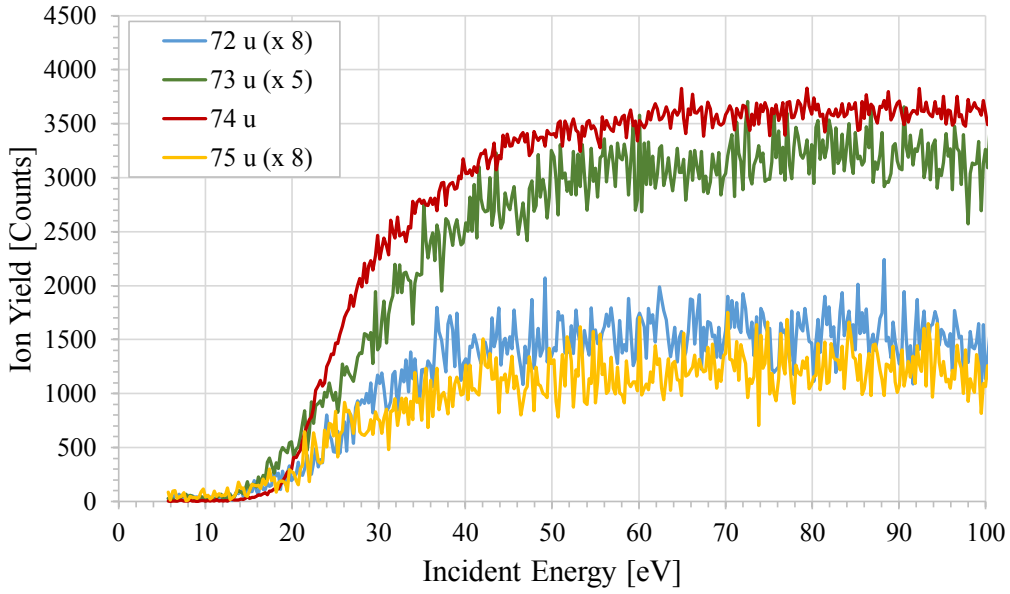

Figure 5.10: ion yield curves for the 72, 73, 74 and 75 u.

The 74 u is the largest peak in the group. (Multiplication factors of 8, 5 and 8 were applied to the 72 u, 73 u and the 75 u data, respectively.) It is proposed that the 74 u contains a fluorine atom, based on the assumption that the 74 u ion in the 5-fluorouracil

mass spectrum corresponds to the 56 u ion from the uracil mass spectrum, see Figure 5.2. The difference in mass between these two fragments suggests that the 74 u contains the fluorine atom and the 56 u uracil fragment contains a hydrogen atom in its place. The appearance energy of the 73 u ion is lower than that of the 74 u ion which may indicate that these ions are produced by different fragmentation processes.

5.3.4 64 - 72 u group

Figure 5.11 shows the 64 - 72 u group of peaks in the mass spectrum at 101 eV and compares the model fit (red line) with the data from the ion yield (blue squares). The ion yield curves for each mass are shown in Figure 5.13. There appear to be doubly charged fragments at 69.5 u and 70.5 u but because the mass of the parent ion is 130 u, this cannot be the case. It is likely that the 69.5 u and 70.5 u peaks are the shoulders of a broadened 70 u peak, produced by a fragmentation process that yields energetic 70 u fragments. Figure 5.12 shows the mass spectrum of the 64 - 72 u group at 30 eV. It shows that at lower electron energies the 69.5 u and 70.5 u peaks disappear, and that the appearance energies of integer fragments are not affected.

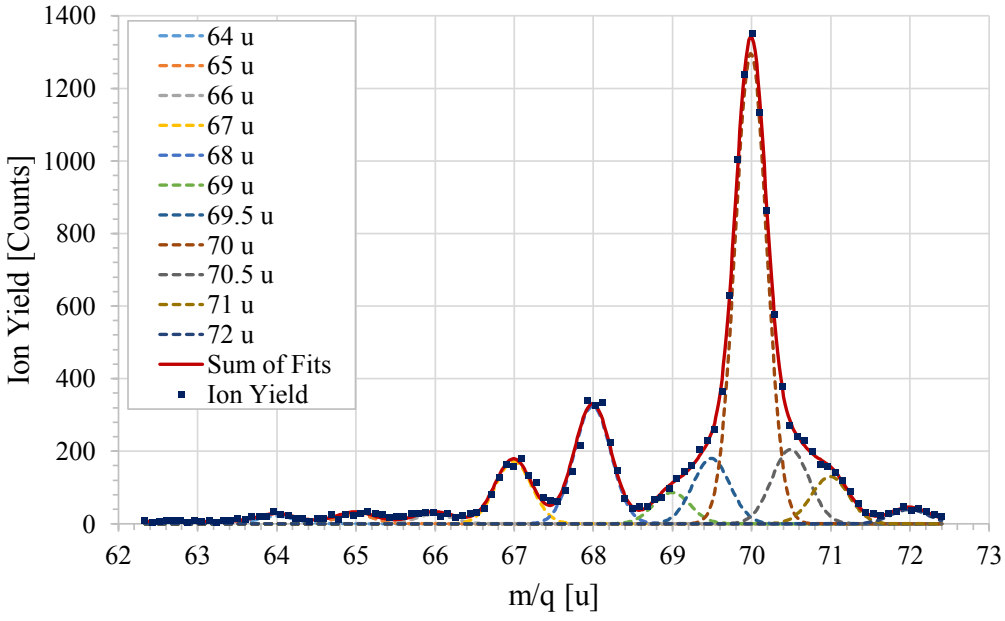

Figure 5.11: Comparison between the Gaussian peak fitting results and the measured ion yields at 101 eV for the 64 - 72 u group.

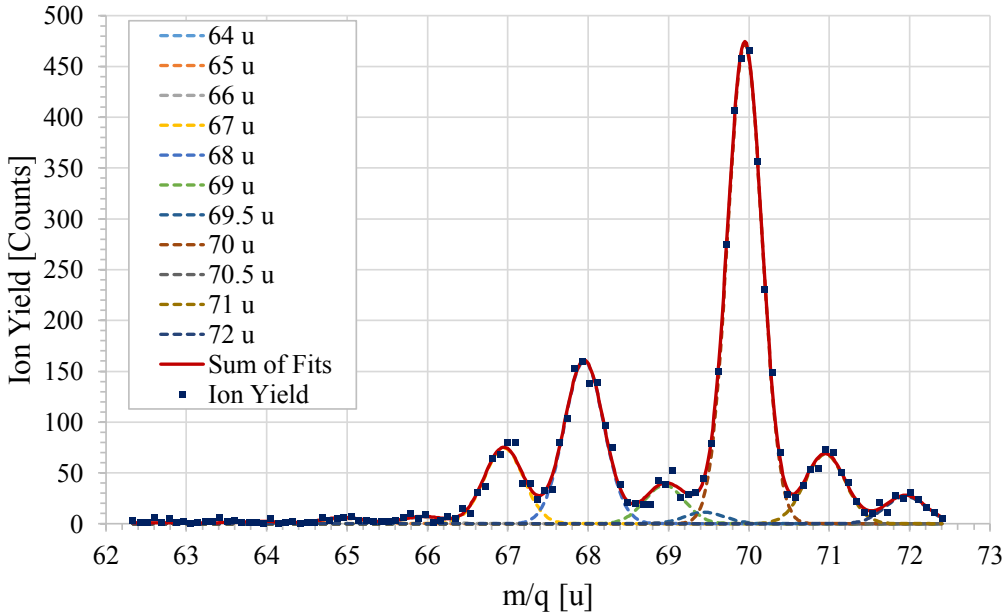

Figure 5.12: Comparison between the Gaussian peak fitting results and the measured ion yields at 30 eV for the 64 - 72 u group.

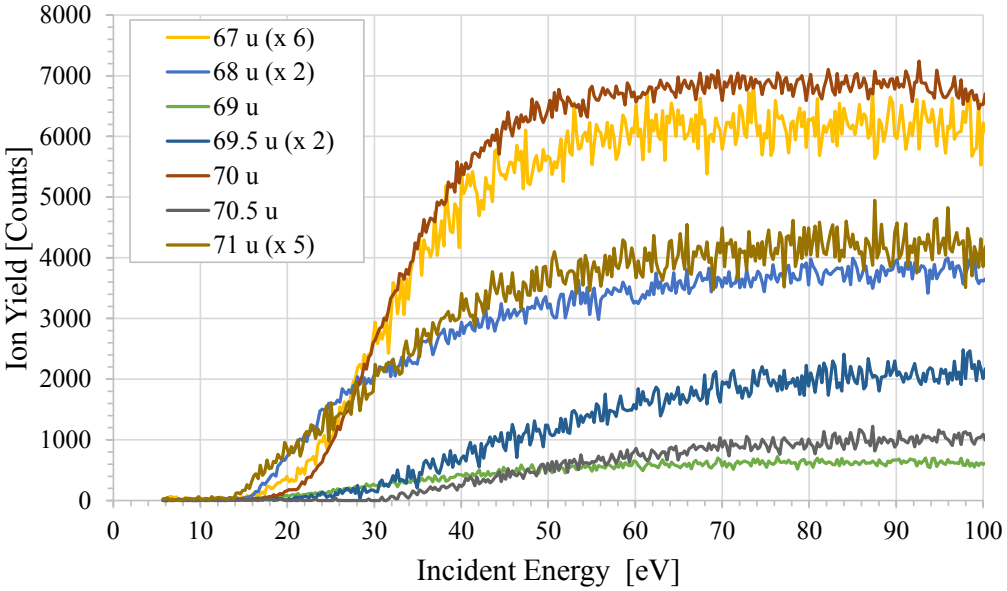

Figure 5.13: Ion yield curves for the 64 - 72 u group.

The peak at 65 u is deemed to be too small to suggest double ionisation and may be due to background contamination, see Figure 5.11.

5.3.5 57 - 62 u group

Figure 5.14 shows the 57 - 62 u group of peaks in the mass spectrum at 101 eV and compares the model fit (red line) with the data from the ion yield (blue squares). The ion yield curves for the 57 - 60 u ions are shown in Figure 5.15 and clearly exhibit a variation in shape over the full energy range. The 60 u is the third most abundant fragment in the mass spectrum.

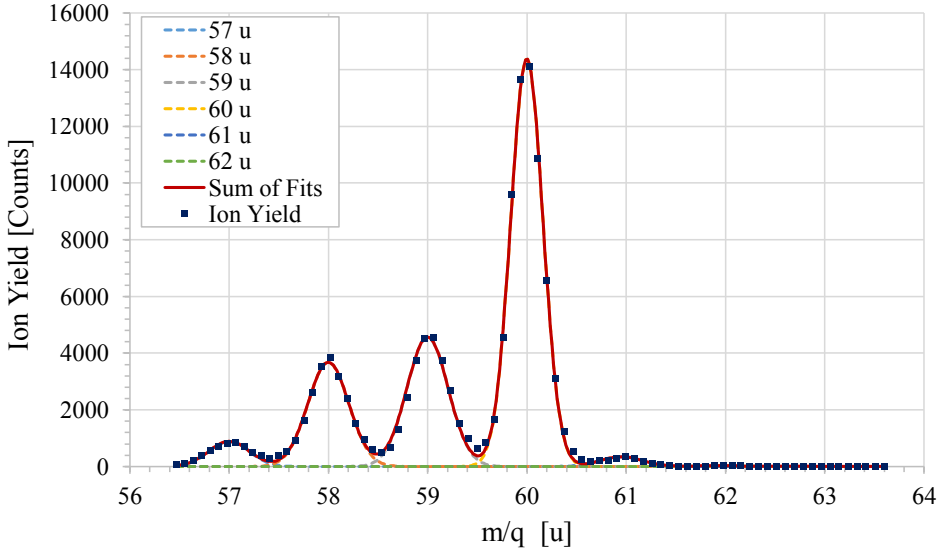

Figure 5.14: Comparison between the Gaussian peak fitting results and the measured ion yields at 101 eV for the 57 - 62 u group.

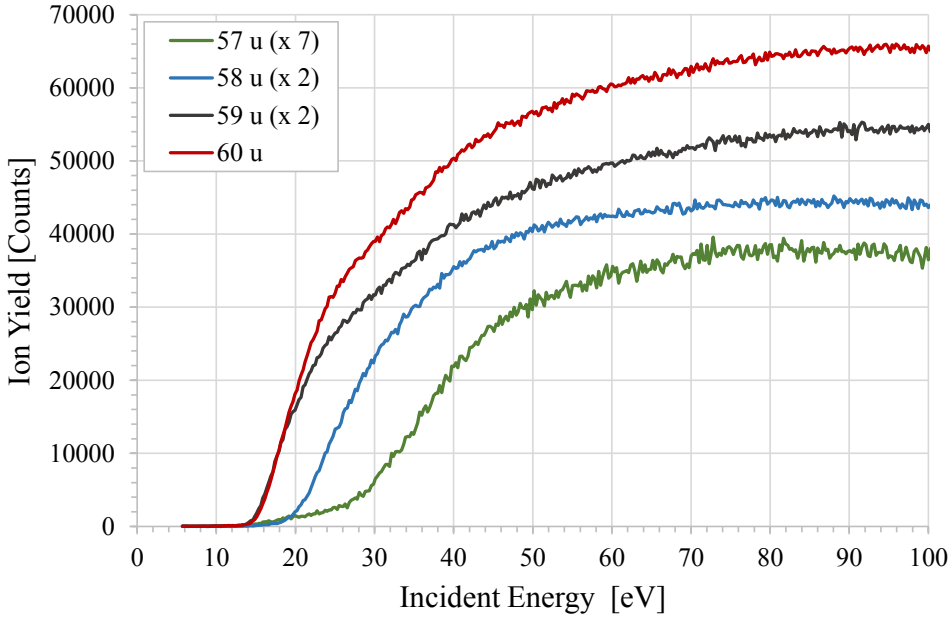

Figure 5.15: Ion yield curves for the 57 - 62 u group.

61 u and 62 u are attributed to isotopes of 60 u. Figure 5.15 shows that the 59 u and 60 u ion yield curves have the same shape over the full energy range with a yield ratio 59 u:60 u = 0.41. Figure 5.2 indicates that the 57 - 60 u group in 5-fluorouracil corresponds to the 39 - 42 u group in uracil, which implies that the 57 - 60 u fragments all contain the fluorine atom.

5.3.6 50 - 56 u group

Figure 5.16 shows the 50 - 56 u group of peaks in the mass spectrum at 101 eV and compares the model fit (red line) with the data from the ion yield (blue squares). The ion yield curves for all masses are shown in Figure 5.17. The 50 - 56 u is the group of peaks that have the lowest ion yields. The 50 - 55 u peaks have similar yields as the 50 - 55 u peaks in the uracil spectrum (see Figure 5.2). The overlapping of both groups in the mass spectra suggests that the fluorine atom is not present in any of the 50 - 55 u fragments. Figure 5.17 shows the ion yield curve for each fragment.

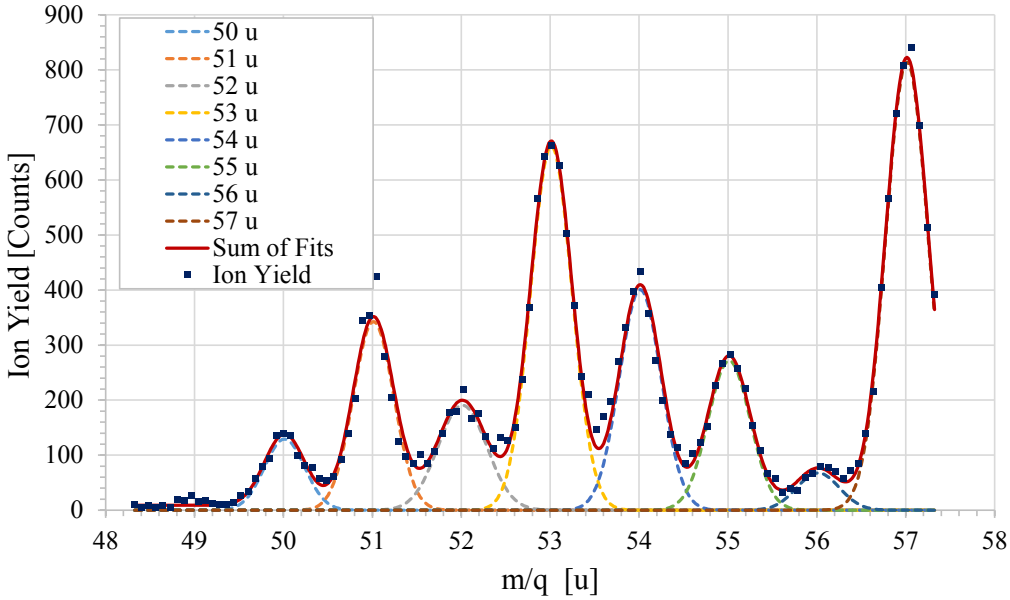

Figure 5.16: Comparison between the Gaussian peak fitting results and the measured ion yields at 101 eV for the 50 - 56 u group. The 57 u peak is included merely to improve the fit of the 56 u peak.

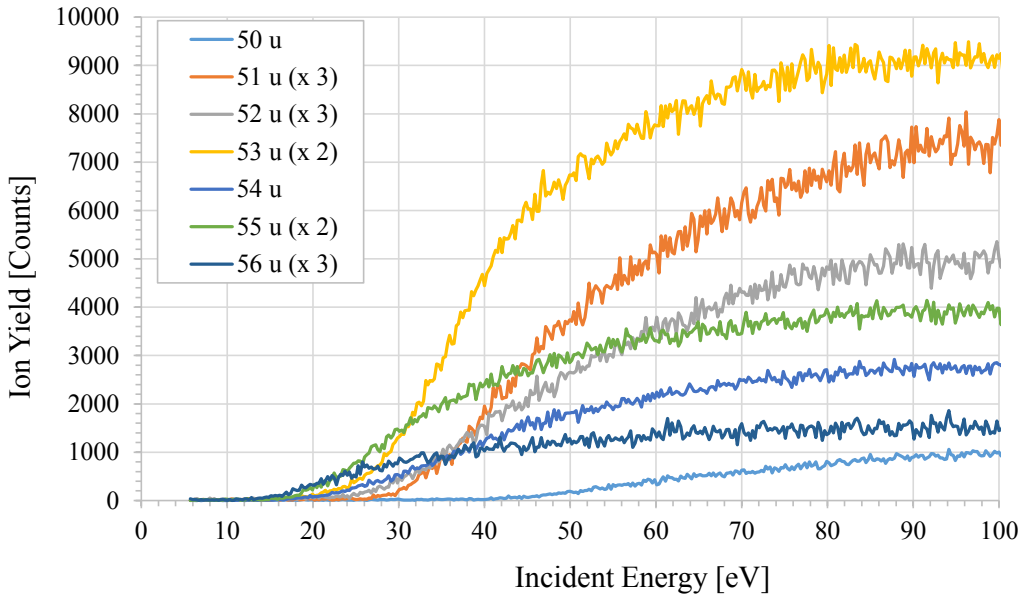

Figure 5.17: Ion yield curves for the 50 - 56 u group.

5.3.7 41 - 47 u group

Figure 5.18 shows the 41 - 47 u group of peaks in the mass spectrum at 101 eV and compares the model fit (red line) with the data from the ion yield (blue squares). The ion yield curves for all masses are shown in Figure 5.20. This group is part of a bigger group that ranges from 36 - 47 u but has been separated into two groups to increase the accuracy of the fits with Gaussians.

Figure 5.18 clearly shows the presence of 42.5 u and 43.5 u fragments, and four half-integer peaks had to be included to obtain a good fit of this group of peaks. 42.5 u and 43.5 u could be due to 85 u and 87 u doubly-ionised fragments, and indeed 87 u is a prominent singly-charged fragment in the mass spectra (see Figure 5.1). Another possibility is that these half-integer peaks are due to broadening of the 41 - 44 u peaks caused by energetic fragmentations. If this is indeed so, it would be difficult to correct the ion yields of the integer peaks, because it is not clear how to redistribute the counts of each half-integer peak to the integer peaks on either side. In the remainder of this chapter we only consider fragmentation processes for the integer fragments in their group.

Figure 5.19 shows that at low electron energies the broadening disappears, so that we can reliably determine the appearance energies of the (integer) fragments.

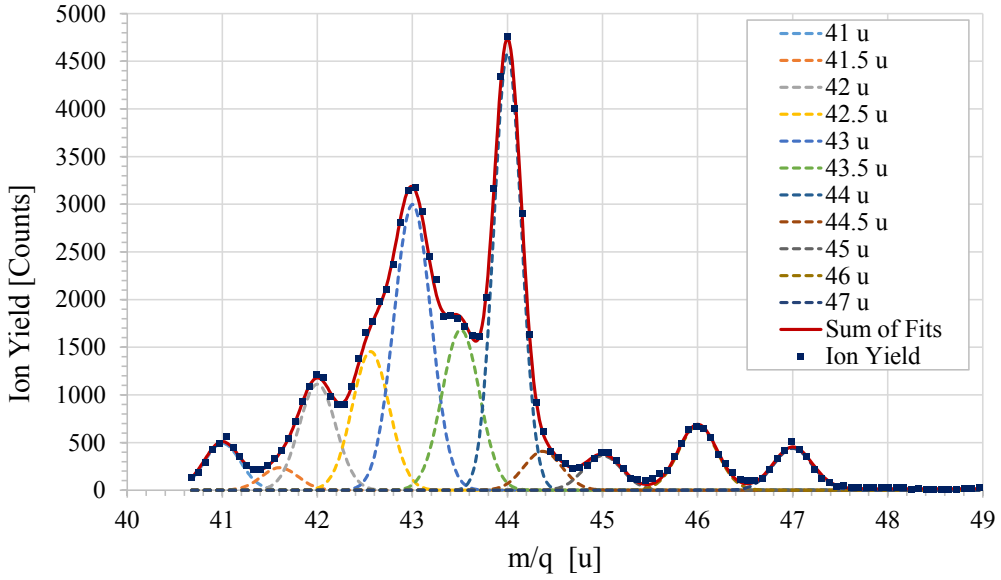

Figure 5.18: Comparison between the Gaussian peak fitting results and the measured ion yields at 101 eV for the 41 - 47 u group.

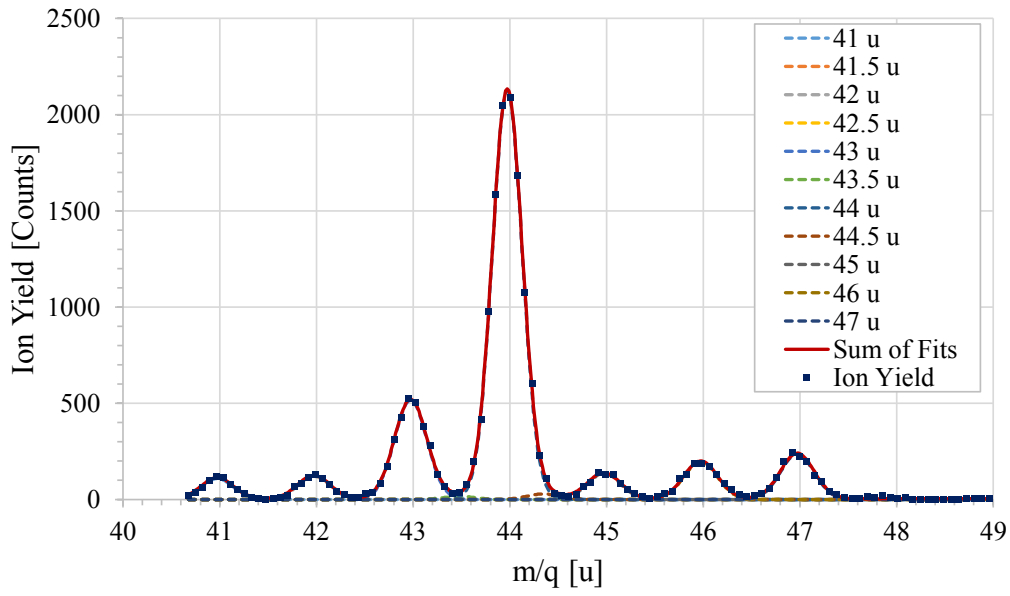

Figure 5.19: Comparison between the Gaussian peak fitting results and the measured ion yields at 30 eV for the 41 - 47 u group.

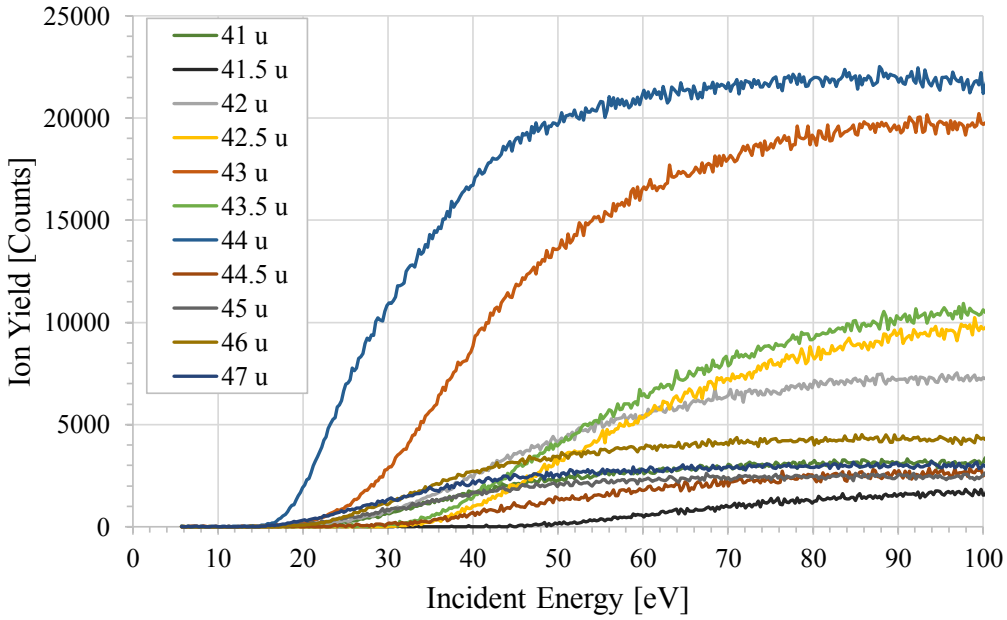

Figure 5.20: Ion yield curves for the 41 - 47 u group.

Figure 5.18 shows the abundance of the 45 - 47 u fragments to be relatively low in 5-fluorouracil but Figure 5.2 shows how the 45 - 47 u are completely absent in uracil. By comparing the mass spectrum of 5-fluorouracil and uracil, it would appear that the 45 - 47 u fragments contain a fluorine atom.

Figure 5.2 shows a mass shift of 18 u between the 45 - 47 u in 5-fluorouracil with the 27 - 29 u in uracil. The ion yield curves for the 45 u and 46 u have similar shape and have a constant yield ratio of 0.58 above 35 eV. The 41 u and 47 u have a constant yield above 55 eV.

5.3.8 36 - 40 u group

Figure 5.21 shows the 36 - 40 u group of peaks in the mass spectrum at 101 eV and compares the model fit (red line) with the data from the ion yield (blue squares). The ion yield curves for the 38 - 41 u ions are shown in Figure 5.22. The yields of the 36 u and 37 u fragments are quite low but still exhibit a peak shape so it was decided to include these peaks in the fit with Gaussians.

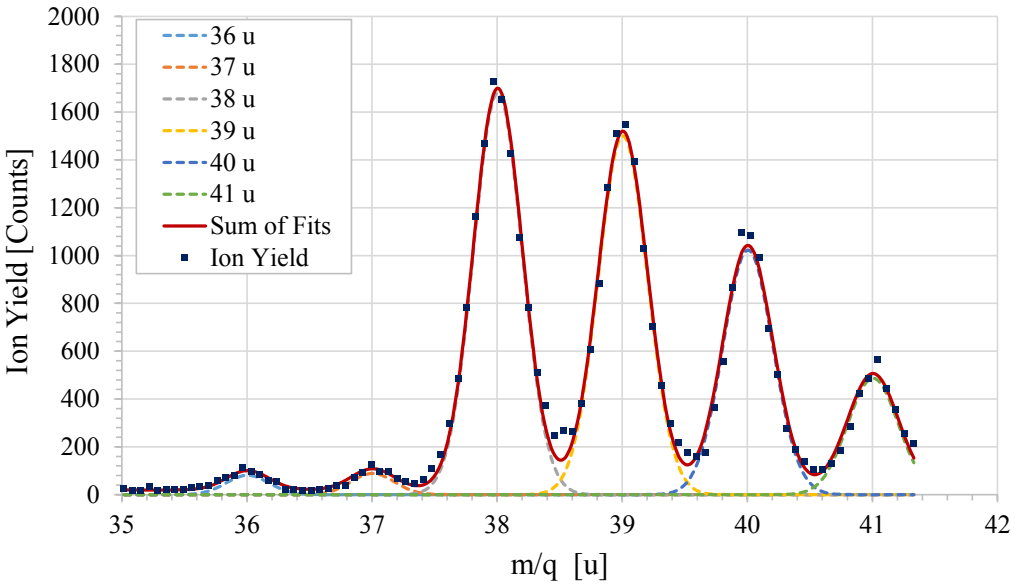

Figure 5.21: Comparison between the Gaussian peak fitting results and the measured ion yields at 101 eV for the 36 - 40 u group. The 41 u peak is included merely to improve the fit of the 40 u peak.

The ion yields in this group were also determined by summing the counts over a suitable bin range for each of the peaks. The bin ranges were determined by taking the two bins with the lowest two counts between each pair of peaks and assigning the left bin to the peak on the left, and the right bin to the peak on the right. The counts obtained in this way were in close agreement with the peak areas obtained in the fits with Gaussians, and it was decided to use the counts for the ion yield curves in Figure 5.22.

The 36 u peak is puzzling. It has a very low appearance energy of 12.9 $\pm$ 0.7 eV and a second onset at 46.0 $\pm$ 1.5 eV. We propose that this peak may be due to an impurity in the 5-fluorouracil and this fragment is not further considered.

The ion yield curves for the 38 - 40 u fragments all appear to be different, indicating that each fragment underwent a different fragmentation process. The 40 u and 41 u ion yield curves are similar in shape, and the yield ratio is 41 u:40 u = 0.22 above 50 eV. Unlike the other ion yield curves, the 38 u has an ion yield curve that does not reach a maximum at 100 eV but keeps rising in count throughout the full energy range.

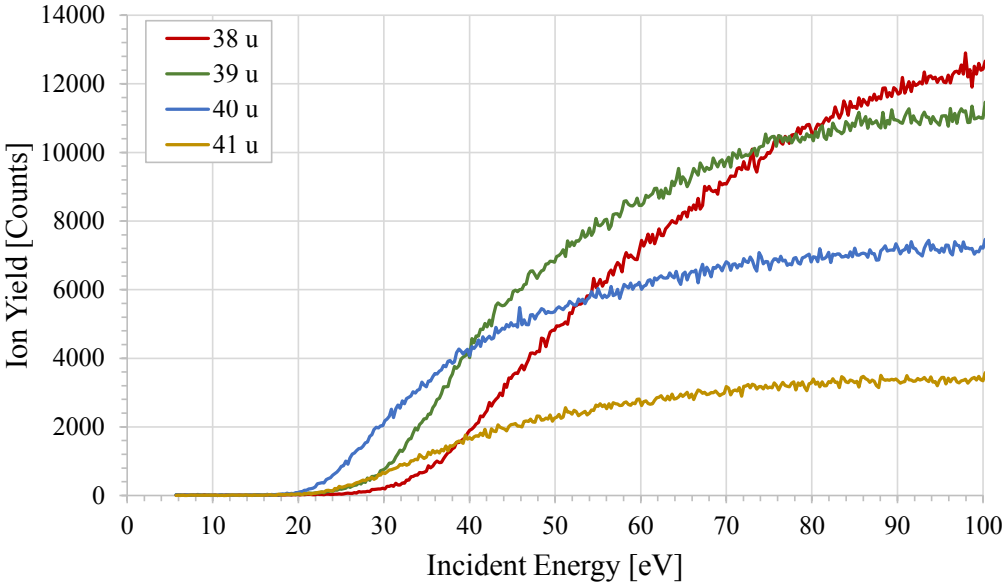

Figure 5.22: Ion yield curves for the 36 - 40 u group.

5.3.9 24 - 34 u group

Figure 5.23 shows the 24 - 34 u group of peaks in the mass spectrum at 101 eV and compares the model fit (red line) with the data from the ion yield (blue squares). The fit with Gaussians was done with ion yield data from 21.0 u to 35.0 u. The ion yield curves for all masses are shown in Figure 5.24.

Figure 5.23 clearly shows that the 28 u peak is not well fitted with a Gaussian and is wider at the bottom. For this reason, the ion yields for this group were also determined by summing the counts over a suitable bin range for each of the peaks. The bin ranges were determined as described in the previous paragraph.

For the 24, 25, 26, 30 and 31 u peaks, the counts obtained in this way were in good agreement with the peak areas in the fit with the Gaussians. For 32 u the counts were slightly higher than the fits, and for 27 - 29 u the counts were clearly higher than the fits for electron energies above about 40 eV. It was decided to take the counts for all peaks in this group, and the ion yield curves obtained are shown in Figure 5.24.

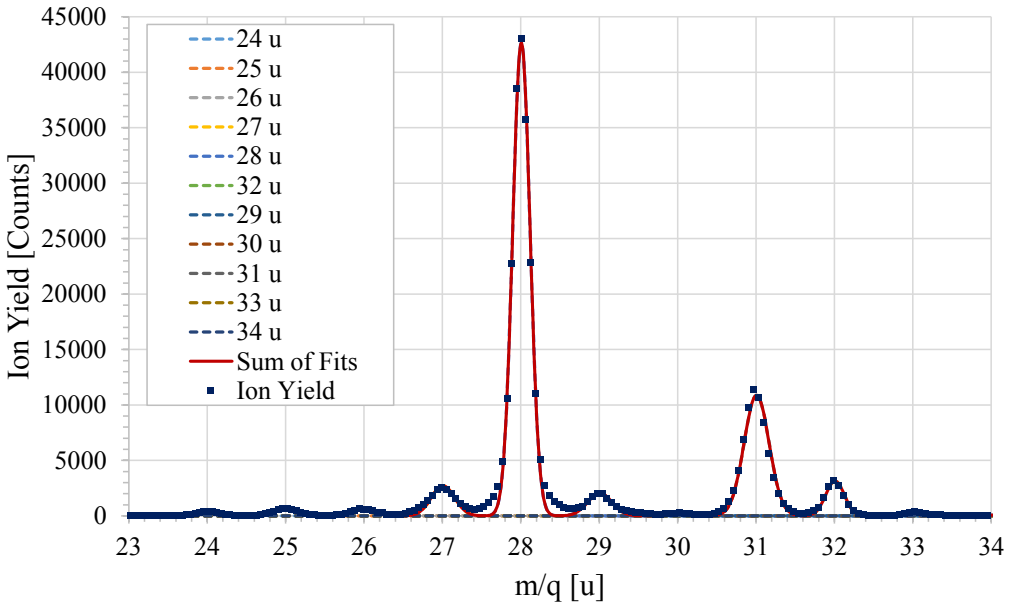

Figure 5.23: Comparison between the Gaussian peak fitting results and the measured ion yields at 101 eV for the 24 - 34 u group.

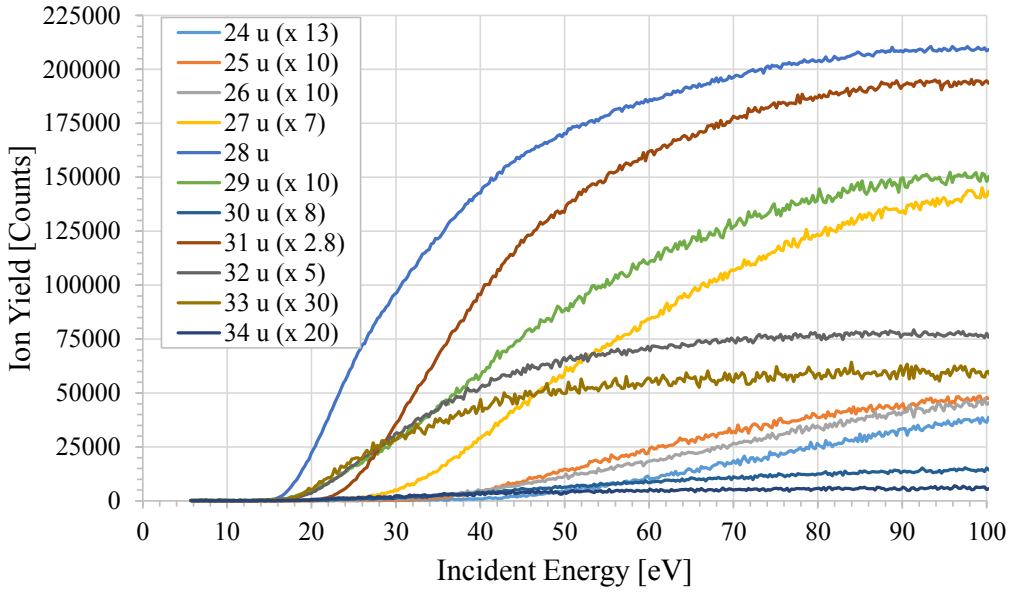

Figure 5.24: Ion yield curves for the 24 - 34 u group.

The ion yield curves shown in Figure 5.24 appear to vary in shape, indicating that fragments in the same group are undergoing different fragmentation processes.

Because these peaks are absent in the uracil mass spectrum, it is likely that fragments 31 u and 32 u contain the fluorine atom, (discussed in Section 5.5). The 31 u peak is

wider than the 32 u peak, which implies that the 31 u is a more energetic fragmentation. Fragments 24 - 29 u cannot contain fluorine.

5.3.10 12 - 15 u group

Figure 5.25 shows the 12 - 15 u group of peaks in the mass spectrum at 101 eV and compares the model fit (red line) with the data from the ion yield (blue squares). The ion yield curves for all masses are shown in Figure 5.26.

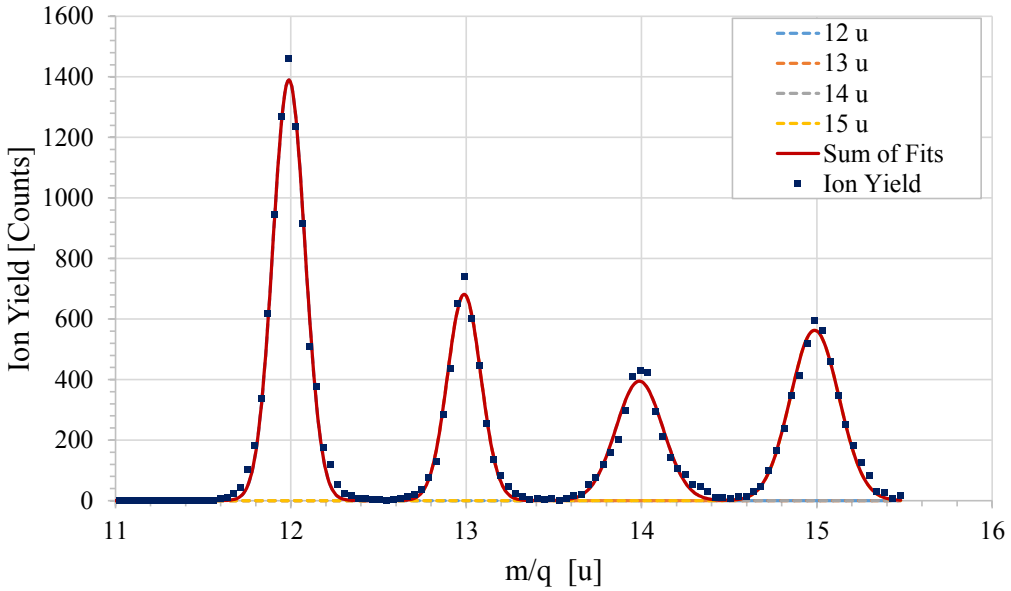

Figure 5.25: Comparison between the Gaussian peak fitting results and the measured ion yields at 101 eV for the 12 - 15 u group.

Because the peaks are well separated, the ion yield curves were determined by summing the counts over a suitable bin range for each of the peaks. The different shapes of the ion yield curves indicate that these fragments may be produced by different fragmentation processes.

It can be seen that all of the ion yield curves in Figure 5.26 continue to increase over the full energy range. The 12 u has the highest appearance energy and the highest yield at 101 eV in this group.

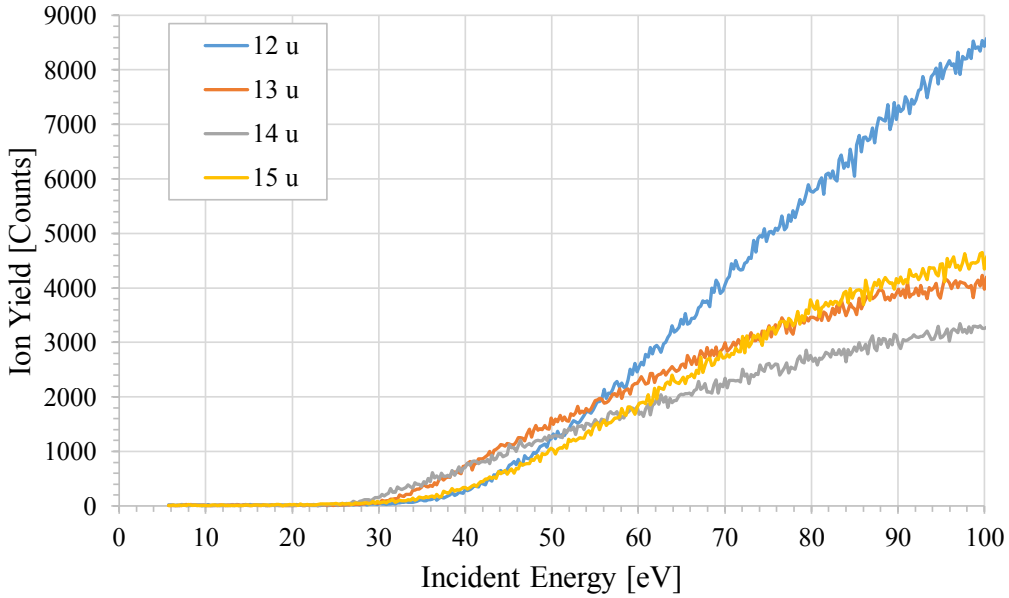

Figure 5.26: Ion yield curves for the 12 - 15 u group.

5.4 Appearance energies

5.4.1 Introduction

The ionisation energy can be defined as the minimum amount of energy that is needed to be transferred to a neutral molecule to cause ionisation of that molecule with the removal of a single electron. The *appearance energy* of a fragmentation is the minimum amount of energy that must be supplied to a molecule to produce that ion. Each fragment will appear as a peak on a mass spectrum, and the height of the peak provides information on the abundance of the corresponding fragment. The appearance energies of the fragments are important because these give information on the fragmentation processes as the incident electron energy increases.

The appearance energies were determined using the LabVIEW program *Onsets.vi* (discussed in Section 4.6.2). The appearance energy results obtained from this experiment allow us to investigate the fragmentation pathways of 5-fluorouracil, and are discussed in more detail in Section 5.5.

In this section, a comparison will be made between the appearance energies of 5-fluorouracil, obtained in this experiment, with the appearance energies for fragments of uracil from Diskin [2015] and for fragments of other halo-uracil molecules found in the research of Denifl et al. [2004b].

A halo-uracil molecule consists of a halogen atom replacing a hydrogen atom in the uracil molecule. The three halo-uracil molecules used for comparison are the 5-chlorouracil, 6-chlorouracil and 5-bromouracil, (i.e. the halogens are chlorine and bromine). The structures of these molecules are shown in Figure 5.27.

5.4.2 Comparing results

Table 5.1 displays the appearance energy results obtained in this experiment for chosen fragments of 5-fluorouracil, as well as results obtained by Diskin [2015] for uracil. In each case, the corresponding uncertainty of each result is stated. For 5-fluorouracil fragments containing the fluorine atom, we have taken the corresponding uracil fragment containing a hydrogen atom instead.

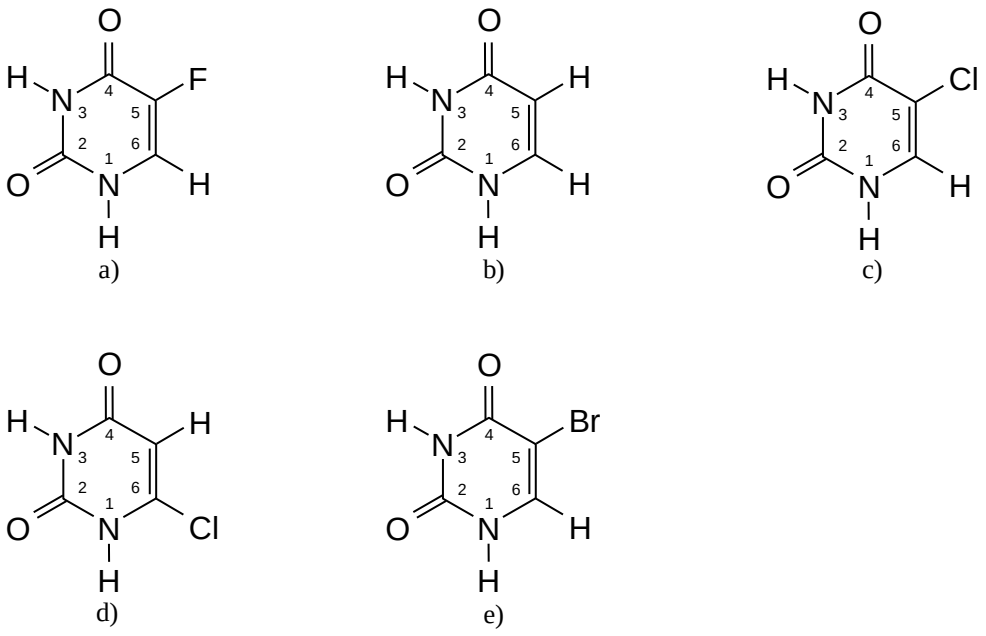

Figure 5.27: Molecular structure of a) 5-fluorouracil, b) uracil c) 5-chlorouracil, d) 6-chlorouracil and e) 5-bromouracil.

Appearance Energies (eV)				
Mass (u)	Possible assignments	5-fluorouracil, [present data]	Mass (u)	uracil, [Diskin, 2015]
130	$C_4H_3N_2O_2F^+$	9.5 ± 0.2	112	9.15 ± 0.21
88	$C_3H_3NOF^+$	11.5 ± 0.2	70	11.04 ± 0.84
87	$C_3H_2NOF^+$	11.4 ± 0.2	69	10.84 ± 0.17
86	C_3HNOF^+	17.8 ± 0.3	68	12.36 ± 0.29
70	$OCNCO^+$ / $C_2H_2N_2O^+$	16.2 ± 0.7, 21.1 ± 0.4	70	11.04 ± 0.84
60	C_2HOF^+	14.0 ± 0.2	42	13.07 ± 0.24
59	$C_2H_2NF^+$ / C_2FO^+	13.6 ± 0.2	41	13.21 ± 0.25
58	C_2HNF^+	14.5 ± 0.6, 17.6 ± 0.3	40	13.01 ± 0.66
57	C_2NF^+	13.1 ± 0.2, 26.4 ± 0.3	39	16.52 ± 0.72
47	COF^+	14.8 ± 0.2	29	13.71 ± 1.2
46	$HCNF^+$	17.9 ± 0.7	28	13.40 ± 0.29
44	C_2HF^+	15.1 ± 0.3	26	16.3 ± 0.39
43	$HNCO^+$	14.6 ± 1.4, 19.4 ± 0.7	43	13.58 ± 0.78
39	C_2HN^+	22.0 ± 0.9, 28.0 ± 0.4	39	16.52 ± 0.72
38	C_2N^+	24.4 ± 0.7, 30.8 ± 0.9	38	21.77 ± 0.45
32	CHF^+	16.6 ± 0.4	14	18.69 ± 0.26
31	CF^+	18.0 ± 1.4, 20.2 ± 0.5	13	19.8 ± 2.3
29	$HNCH_2^+$ / HCO^+	16.6 ± 0.6	29	13.71 ± 1.2

Continuation of Table 5.1				
Mass (u)	Possible assignments	5-fluorouracil, [present data]	Mass (u)	uracil, [Diskin, 2015]
28	$HNCH^+$ / CO^+	13.8 ± 0.7, 15.7 ± 0.3	28	13.40 ± 0.29
27	HCN^+	21.4 ± 1.0, 26.9 ± 0.5	27	14.56 ± 0.18
26	$C_2H_2^+$ / CN^+	25.5 ± 1.4	26	16.3 ± 0.39
15	NH^+	29.6 ± 1.2, 36.3 ± 1.3	15	16.9 ± 1.4
14	CH_2^+ / N^+	25.8 ± 0.6	14	18.69 ± 0.26
13	CH^+	27.7 ± 0.5	13	19.8 ± 2.3

Table 5.1: Appearance energy of 5-fluorouracil fragments [present data], compared with uracil fragments, [Diskin, 2015].

Table 5.1 shows that there are substantial differences between the appearance energies of corresponding fragments of 5-fluorouracil and uracil. Taking the estimated errors into account, agreement is obtained for the appearance energies of 130 (112) u, 47 (29) u, 43 u, 31 (13) u, and 28 u. The appearance energies of 88 (70) u, 87 (69) u, 60 (42) u, 58 (40) u, and 44 u are outside the ranges of the error bars, but are less than 1.5 eV apart. This indicates that, despite the similarities of the mass spectra of 5-fluorouracil and uracil, there are differences in the fragmentation patterns of both molecules.

Mass (u)	Assignment	Present results electron impact (eV) 5-fluorouracil	Mass (u)	[Denifl et al., 2004b] results electron impact (eV) 5-chlorouracil
130	$C_4H_3N_2O_2F^+$	9.5 ± 0.2	146	9.38 ± 0.05
87	$C_3H_2NOF^+$	11.4 ± 0.2	103	11.12 ± 0.03
60	C_2HOF^+	14.0 ± 0.2	76	13.19 ± 0.03
44	C_2HF^+	15.1 ± 0.3	60	13.97 ± 0.06
32	CHF^+	16.6 ± 0.4	48	14.92 ± 0.07
31	CF^+	18.0 ± 1.4, 20.2 ± 0.5	47	16.8 ± 0.4
40	$C_2H_2N^+$ / CN_2^+	18.8 ± 0.7	40	12.34 ± 0.2, 16.08 ± 0.2
39	C_2HN^+	22.0 ± 0.9, 28.0 ± 0.4	39	15.61 ± 0.10
28	$HNCH^+$ / CO^+	13.8 ± 0.7, 15.7 ± 0.3	28	13.96 ± 0.05

Table 5.2: Appearance energies of the 5-fluorouracil fragments, compared with the appearance energies of the 5-chlorouracil fragments, determined by Denifl et al. [2004b].

Table 5.2 compares the appearance energies of 5-fluorouracil obtained in this experiment with the appearance energies of 5-chlorouracil obtained by Denifl et al. [2004b]. The appearance energies for 130 (146) u, 87 (103) u, and 28 u are in agreement. The appearance energies of 60 (76) u, 44 (60) u, 32 (48) u, and 31 (47) u are less than 1.5 eV apart, but there are substantial differences in the appearance energies of 40 u and 39 u. This again points to differences in the fragmentation patterns of these molecules related to the halogen atom in position 5 in the halo-uracils.

Parent ion	Method	Appearance energy (eV)
5-fluorouracil, [present data]	Electron impact	9.5 ± 0.2
5-chlorouracil, [Denifl et al., 2004b]	Electron impact	9.38 ± 0.05
6-chlorouracil, [Denifl et al., 2004b]	Electron impact	9.71 ± 0.05
5-fluorouracil, [Holland et al., 2008]	Photoelectron spectroscopy	9.54 ± 0.02

Table 5.3: Appearance energy results for the parent ions of: 5-fluorouracil, 5-chlorouracil and 6-chlorouracil.

The ionisation energy of 5-fluorouracil (the appearance energy for the 130 u parent ion) was determined to be 9.5 ± 0.2 eV. Table 5.3 shows that this value agrees well with the ionisation energies of 5-chlorouracil and 6-chlorouracil determined by Denifl et al. [2004b], and 5-fluorouracil determined by Holland et al. [2008] using photoelectron spectroscopy.

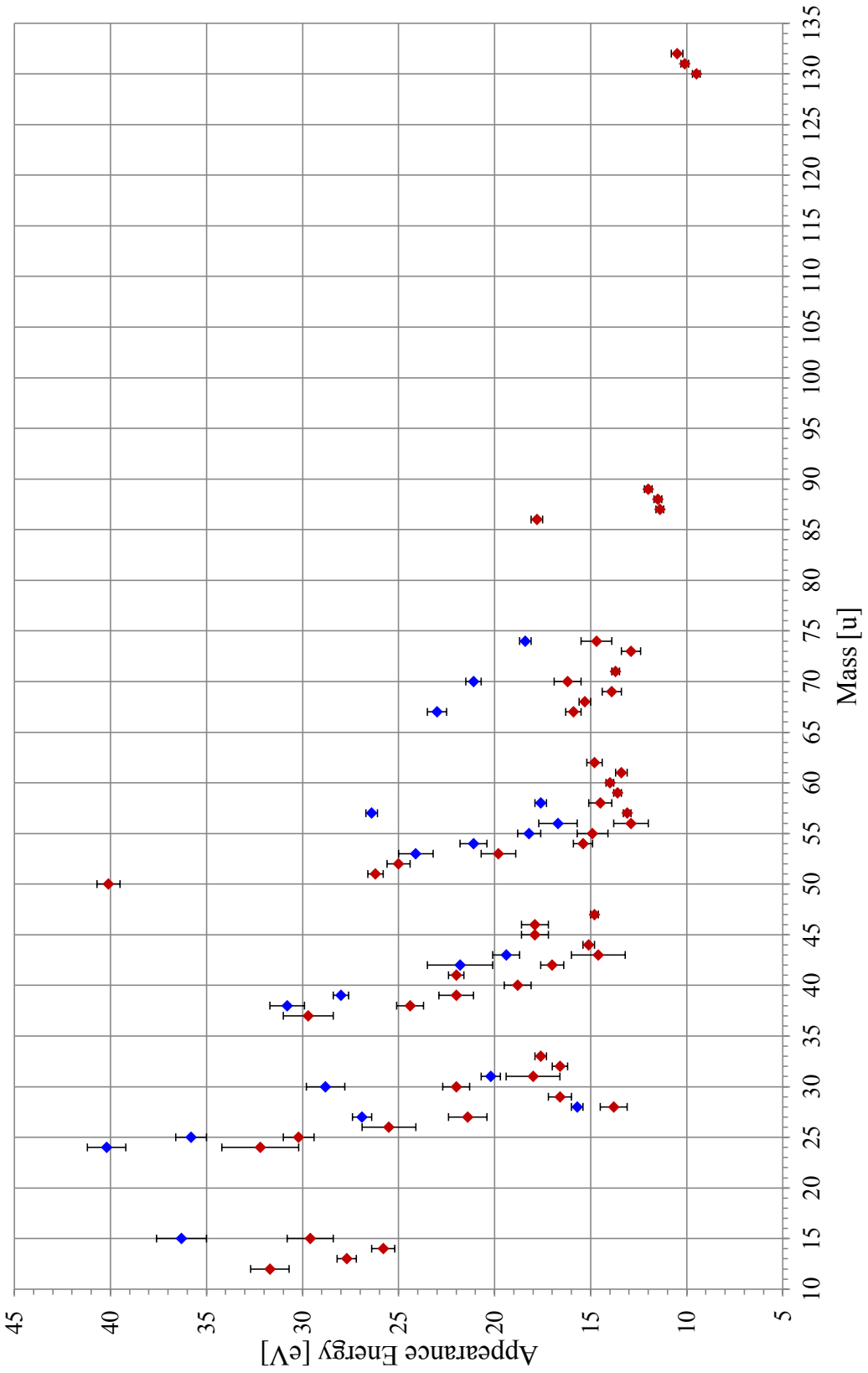

Figure 5.28: Appearance energies for the positive fragments of 5-fluorouracil. The appearance energies are shown as red and blue squares. The red squares indicate first onsets and the blue squares indicate second onsets.

Figure 5.28 shows the appearance energies for the 5-fluorouracil fragments determined in this work. For eight of the most important fragments, the ion yield curves and the fitted onset functions are shown in Figure 5.29 to 5.36. The ion yield curves of 74 u, 70 u, 31 u and 28 u show a second onset. Figure 5.28 shows that in general the smaller fragments have higher appearance energies because more bond breakages may be required to produce these fragments. Apart from the parent ion, the fragments with the lowest appearance energies are 87 u and 88 u, and most smaller fragments may be produced with the 87 u (or 88 u) ion as the intermediate. Several groups of fragments show increasing appearance energies with reducing mass: 56 - 50 u, 43 - 38 u, 28 - 24 u, and 14 - 12 u. This may be partly due to successive loss of hydrogen atoms, but this cannot be the full explanation because 5-fluorouracil has only three hydrogen atoms.

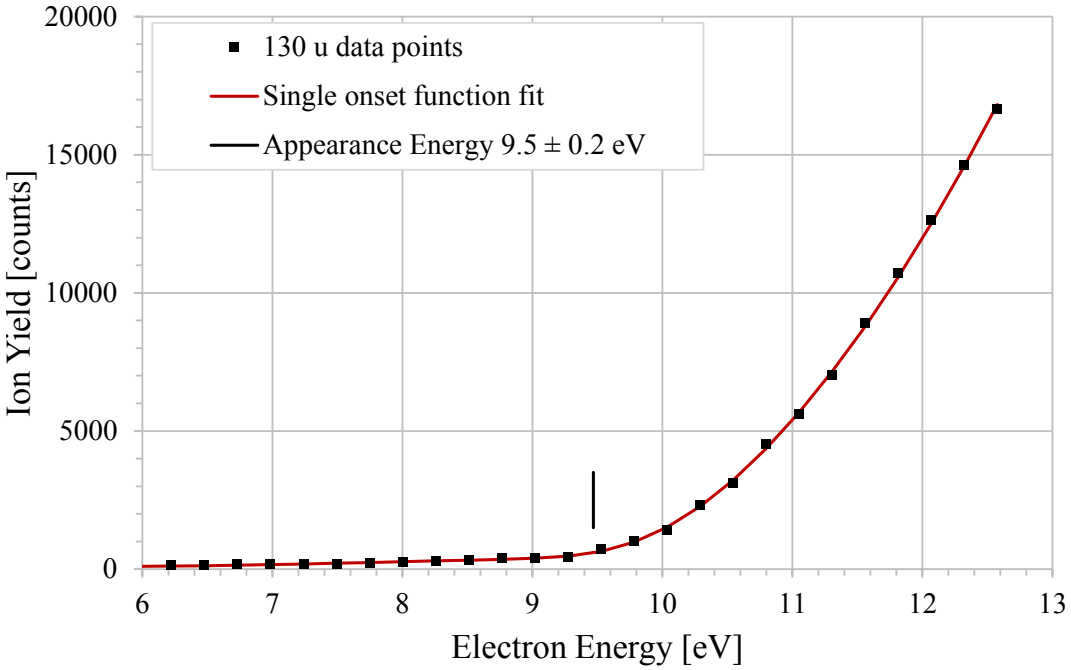

Figure 5.29: Appearance energy graph of the 130 u fragment.

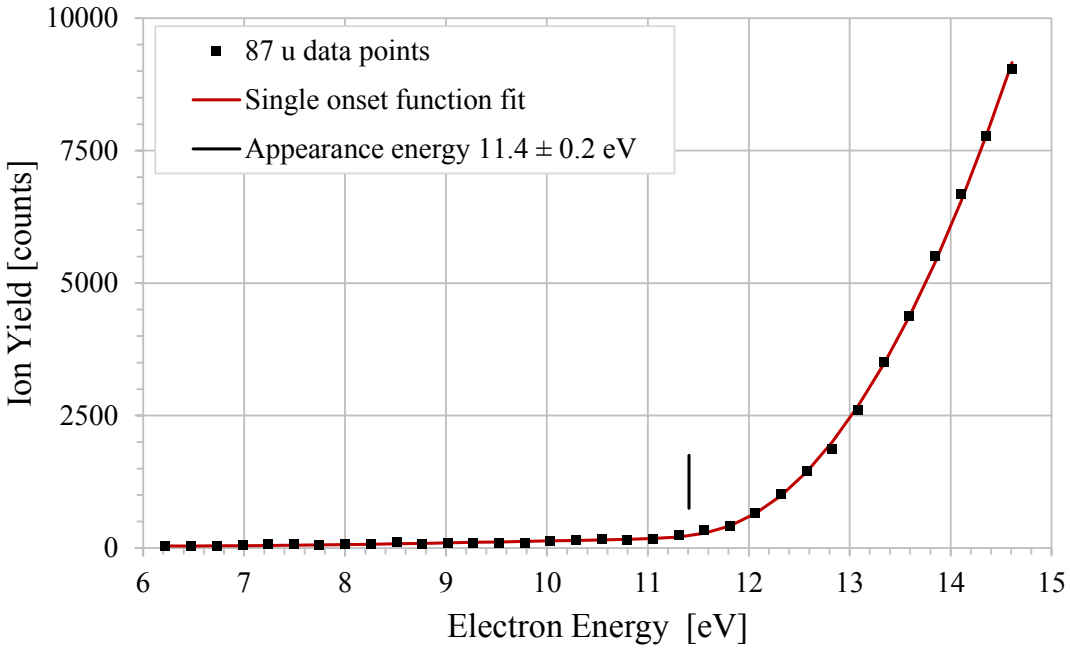

Figure 5.30: Appearance energy graph of the 87 u fragment.

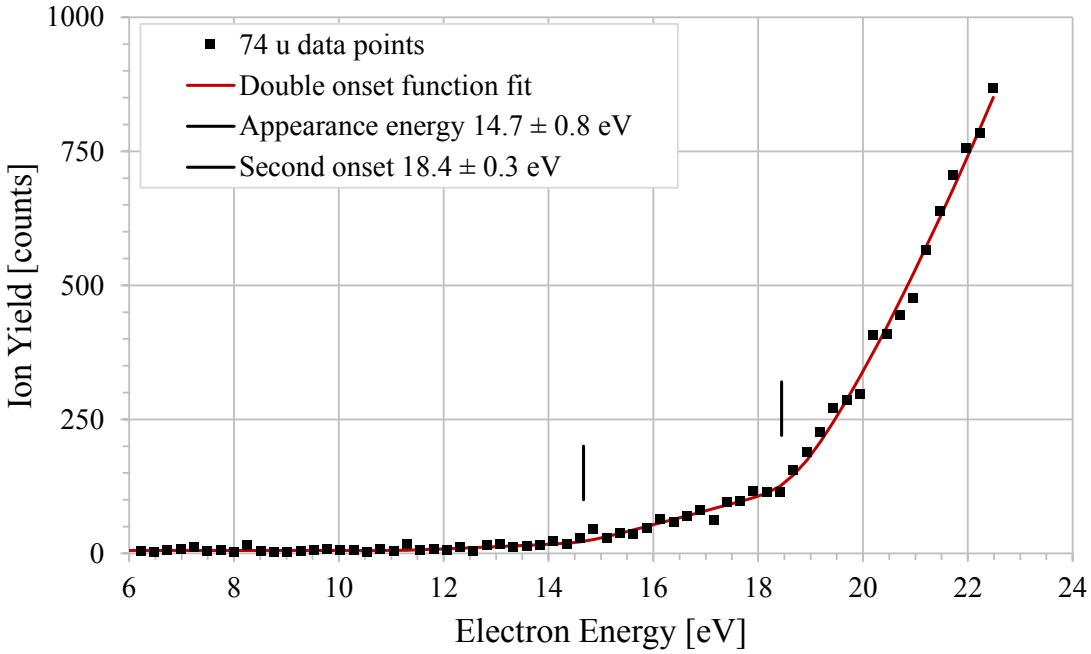

Figure 5.31: Appearance energy graph of the 74 u fragment.

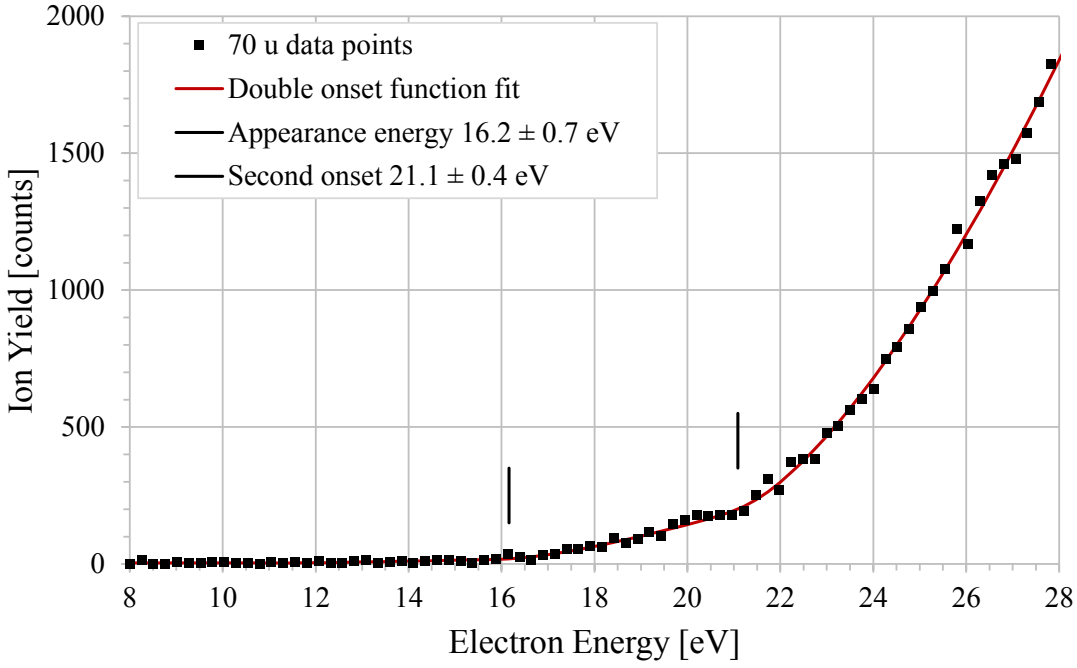

Figure 5.32: Appearance energy graph of the 70 u fragment.

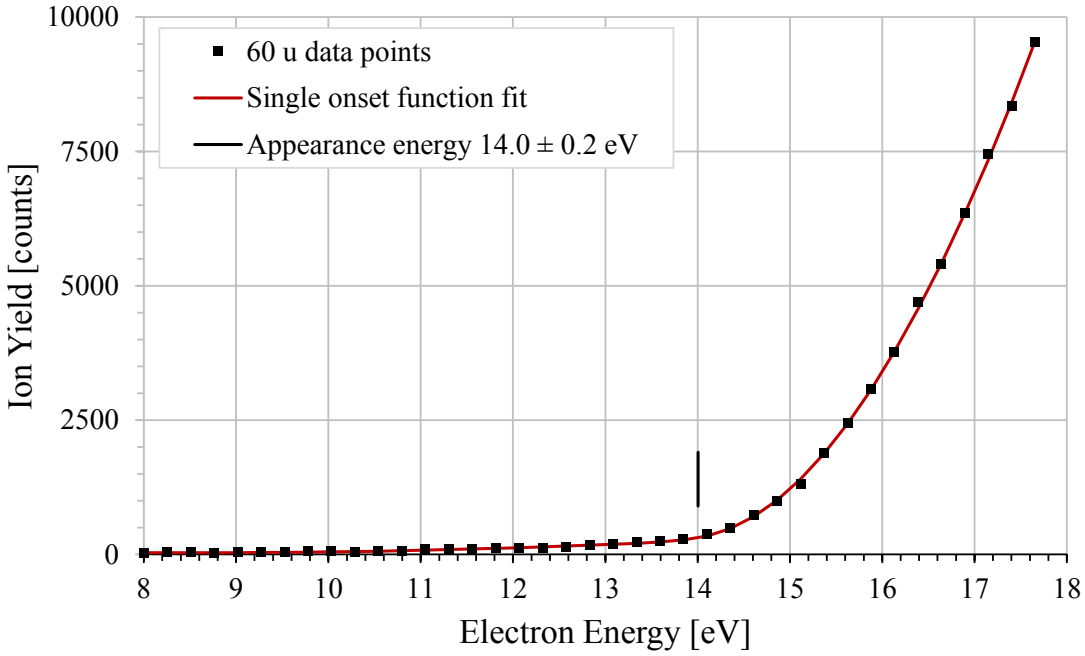

Figure 5.33: Appearance energy graph of the 60 u fragment.

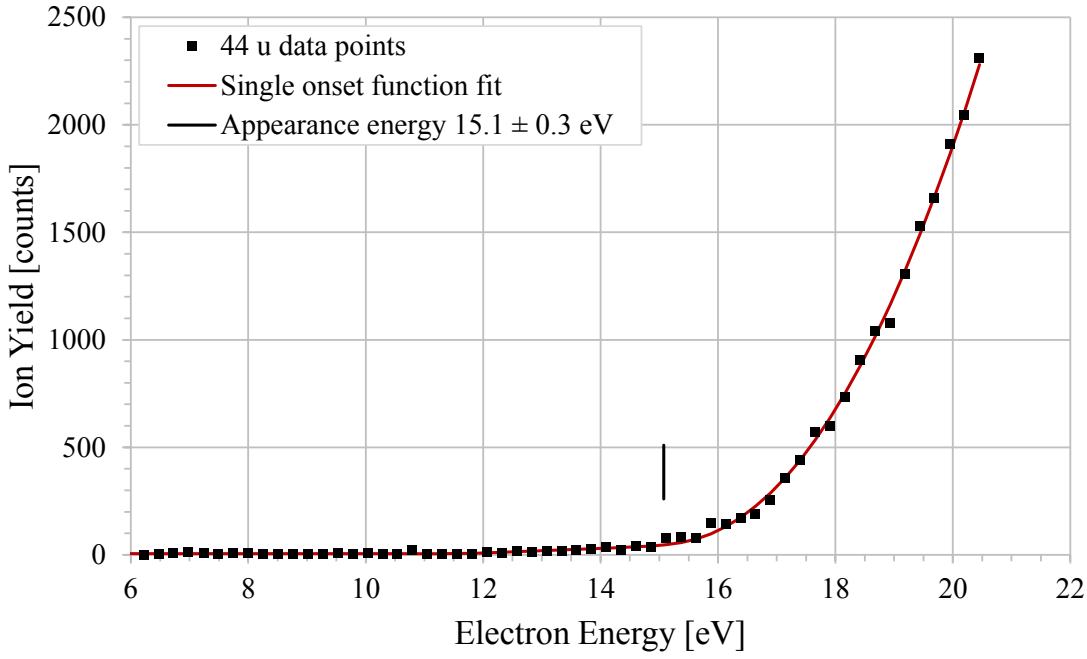

Figure 5.34: Appearance energy graph of the 44 u fragment.

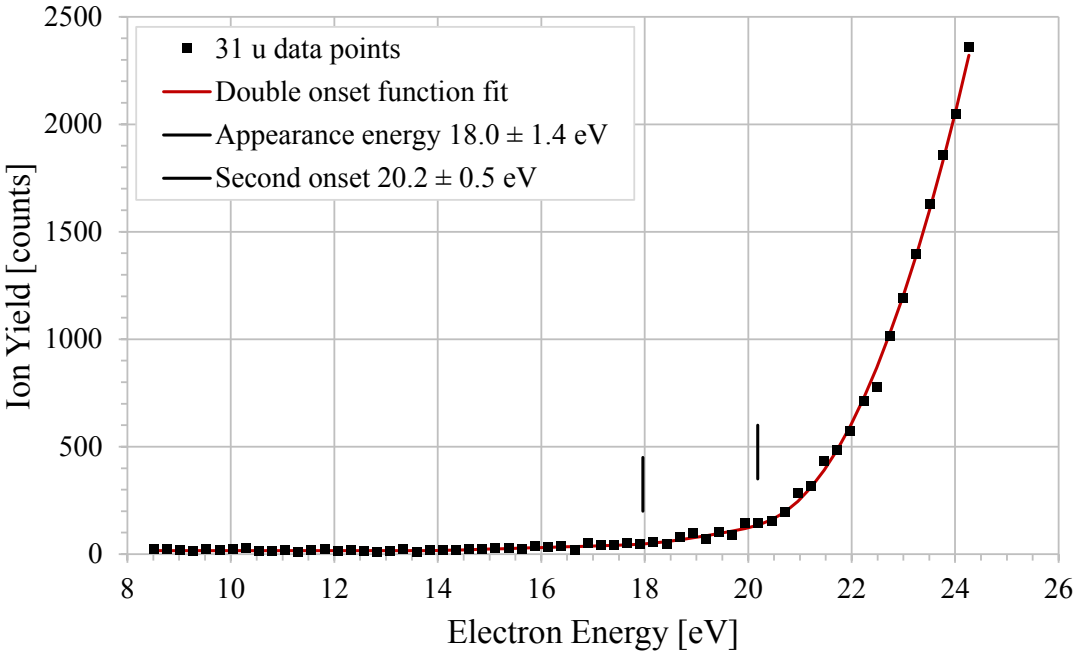

Figure 5.35: Appearance energy graph of the 31 u fragment.

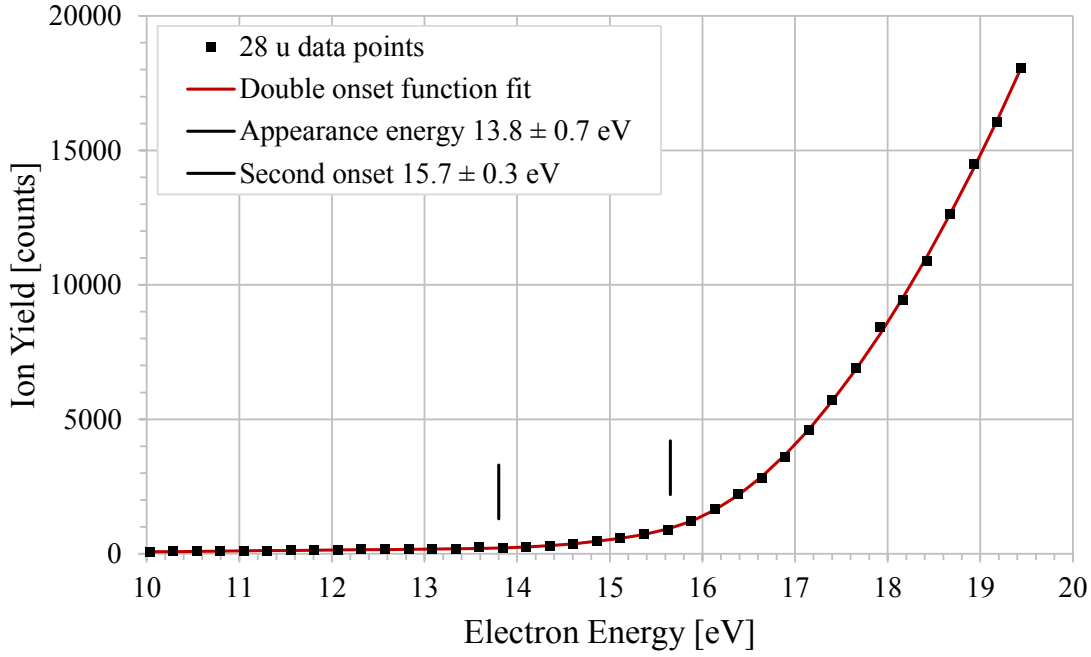

Figure 5.36: Appearance energy graph of the 28 u fragment.

5.5 Fragmentation processes

Introduction

This section discusses fragmentation processes that lead to the formation of various positively charged fragments of 5-fluorouracil based on the measured data. This section is divided into paragraphs for each of the groups of fragments, beginning with the 130 - 133 u group and ending with the 12 - 15 u group.

This section will include a short discussion on the fragmentation pathways for chosen fragments. For several of the fragments the proposed pathways are compared with results obtained for uracil (Rice et al. [1965], Jochims et al. [2005], Diskin [2015]), 5-fluorouracil and 5-chlorouracil ([Denifl et al., 2004c], Ferreira da Silva et al. [2011]), and 5-bromouracil (Imhoff et al. [2007]).

For most of the chosen fragments the fragmentation pathway is represented as equations of molecular formulas. In addition, some fragments are presented in figures as combinations or fragmentations of the parent ion.

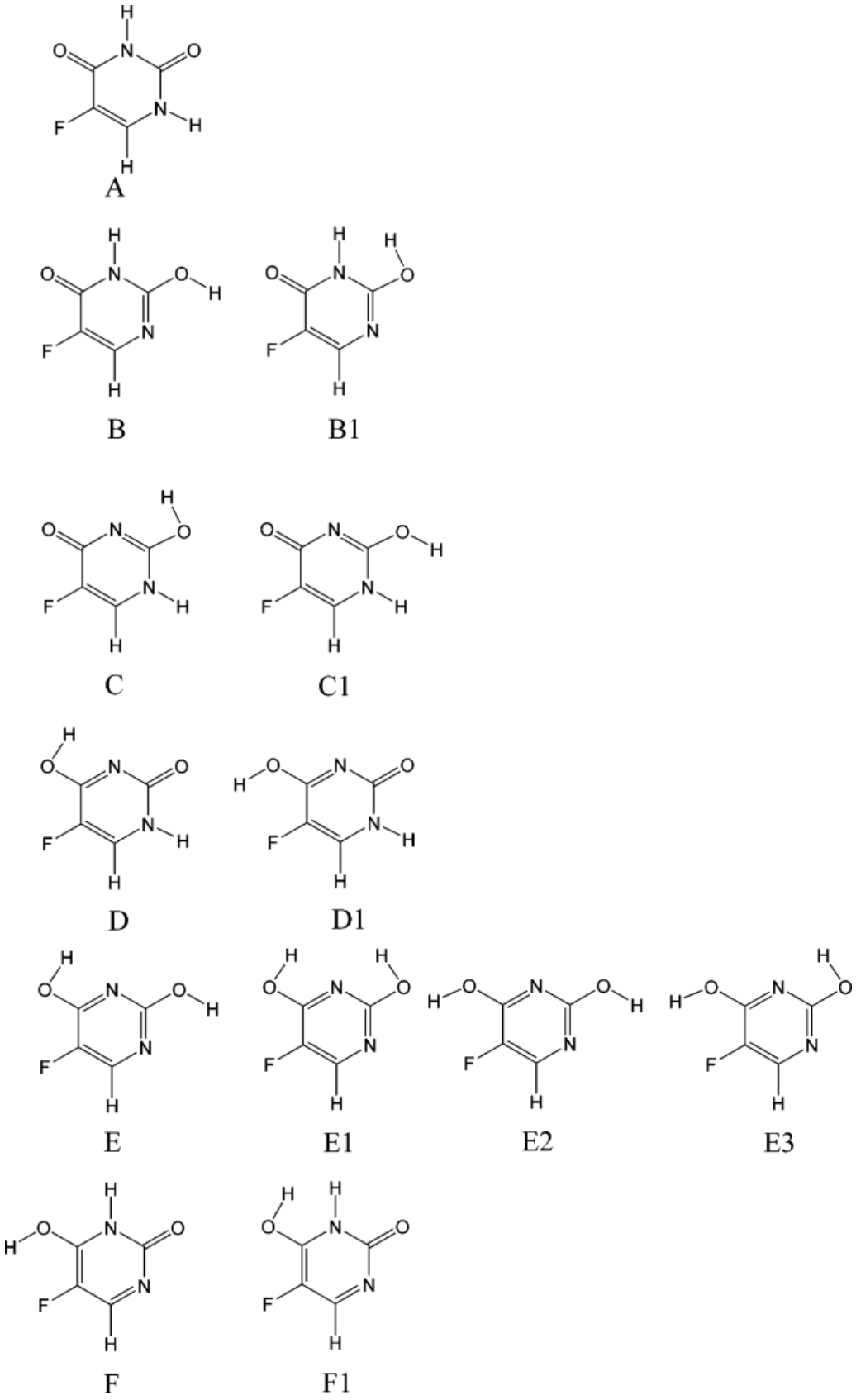

Figure 5.37: Tautomeric and rotameric forms of 5-fluorouracil, [Markova et al., 2005].

Many fragments may be formed through more than one fragmentation process. In some cases the shapes of the ion yield curves may indicate a similar fragmentation process for two fragments 1 u apart, related to tautomerization. An ion yield curve showing a second onset indicates the presence of an additional fragmentation process.

The 5-fluorouracil molecule can exist in different tautomeric forms and some of these may be present in the molecular beam. Figure 5.37 shows the various tautomeric forms of 5-fluorouracil, [Markova et al., 2005]. Tautomerization preceding the fragmentation of the molecule may lead to rearrangements of hydrogen atoms during the fragmentation, [van der Burgt et al., 2014]. These various forms of 5-fluorouracil were taken into consideration when analysing the fragmentation processes.

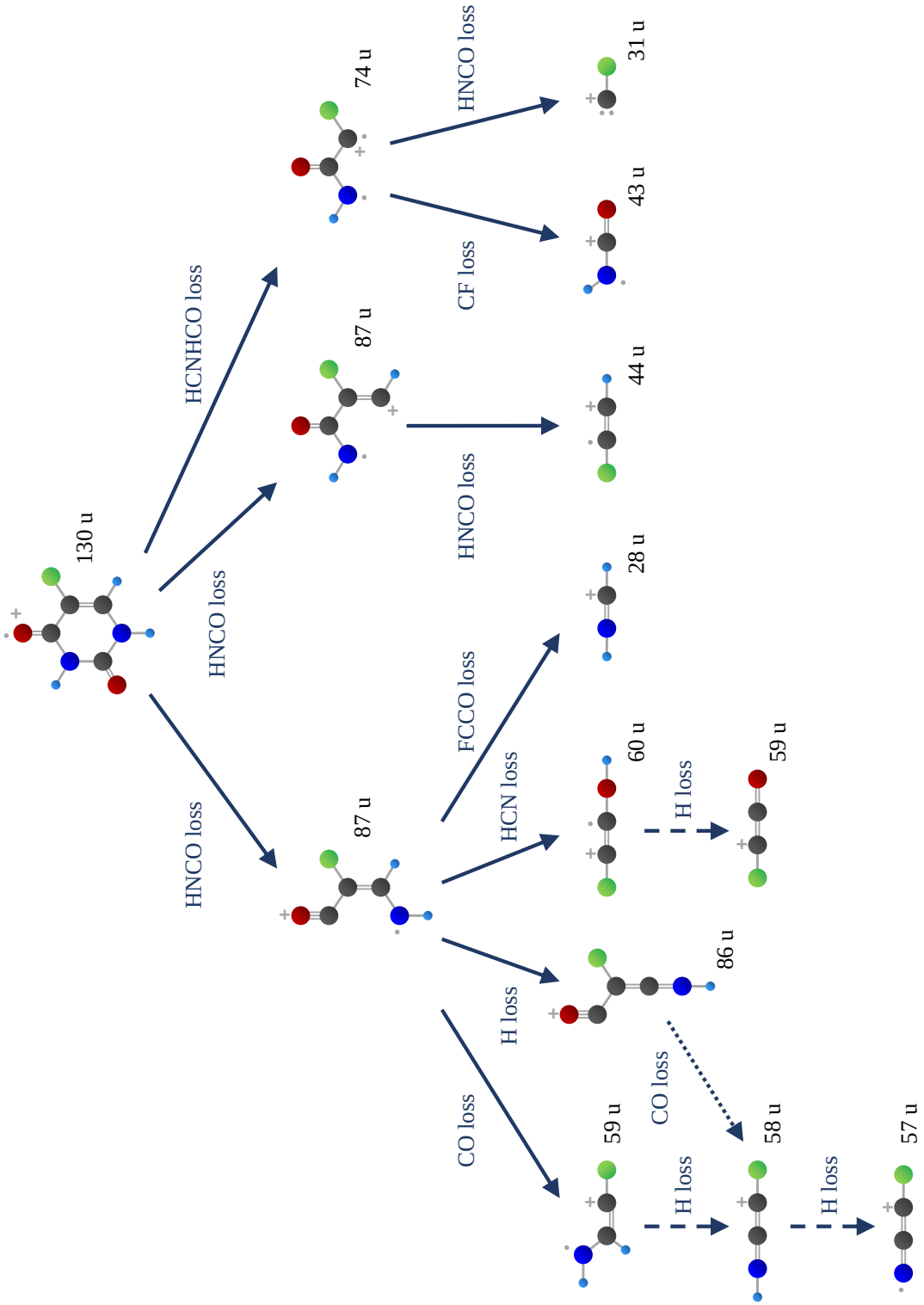

Figure 5.38: Fragmentation processes for the main fragments of 5-fluorouracil. The four fragmentations of the 87 u ion on the left are adapted from Rice et al. [1965] and Jochims et al. [2005].

5.5.1 130 - 132 u parent ions

There exists very weak peaks at 131 u and 132 u in the mass spectrum, which are attributed to 5-fluorouracil isotopes. The ion yield ratio 131 u:130 u = 0.067 and 132 u:131 u = 0.094. The 130 - 132 u ion yield curves all exhibit the same shape over the full energy range which would be expected, as the difference in their mass is mostly due to the ^{13}C isotopes, see Figure 5.6.

5.5.2 86 - 88 u fragmentation processes

The first fragment to appear in the mass spectrum below the 130 u ion is the 88 u ion. The 88 u fragment could have formed by NCO loss due to N3-C4 and N1-C2 bond breakages, with the hydrogen atom migrating to the oxygen atom. The 87 u ion is one of the more prominent fragments in the 5-fluorouracil mass spectrum and is $C_3H_2NOF^+$ due to HNCO loss. The 87 u fragments may be produced following HNCO loss due different combinations of bond cleavages, such as: N1-C2 and N3-C4, C6-N1 and C2-N3, and C2-N3 and C4-C5 bond cleavages. Figure 5.39 shows the possible HNCO cleavages that form the 87 u fragment. The 86 u could form following HNCO + H loss, see Figure 5.39 which is indicated by its appearance energy, which is much higher than the appearance energies of the 87 u and 88 u.

Figure 5.8 shows the ion yield curves of the 86 - 88 u fragments. The ion yield of the 88 u has the same shape over the full energy range as the 87 u, and also has the same appearance energy (11.5 $\pm$ 0.2 eV and 11.4 $\pm$ 0.2 eV, respectively). The 86 u ion yield curve has a similar shape as the 87 u ion yield curve above 50 eV pointing towards tautomerization during the fragmentation. Interestingly, the ion yield ratio 86 u:87 u = 0.059 whereas the ion yield ratio of the 68 u:69 u = 0.45 in uracil, [Diskin, 2005]. The fragmentation reactions are:

$$C_4H_3N_2O_2F^+ \ [130u] \longmapsto C_3H_3NOF^+ \ [88u] + NCO \ [42u] \tag{5.1}$$

$$C_4H_3N_2O_2F^+ \ [130u] \longmapsto C_3H_2NOF^+ \ [87u] + HNCO \ [43u] \tag{5.2}$$

$$C_4H_3N_2O_2F^+ \ [130u] \longmapsto C_3HNOF^+ \ [86u] + CH_2NO \ [44u] \tag{5.3}$$

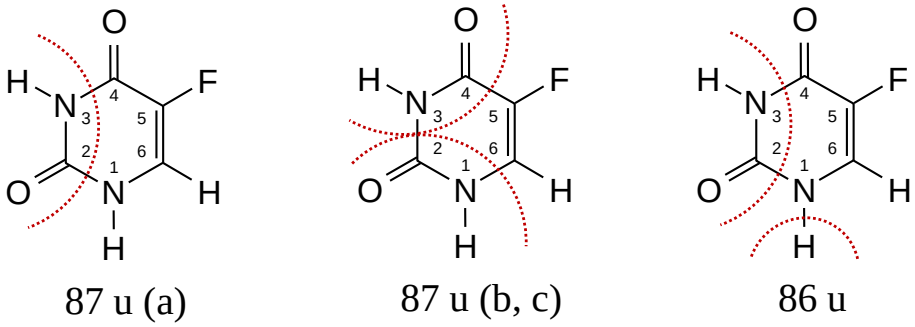

Figure 5.39: Fragmentation processes producing the 87 u and 86 u fragments.

5.5.3 73 - 74 u fragmentation processes

The 74 u ion may be produced following a C_2H_2NO loss caused by C5-C6 and C2-N3 bond breakages. The 74 u is a small but distinct fragment, which is not present in the uracil mass spectra (see Figure 5.3), but a possible corresponding fragment appears at 56 u in the mass spectra for uracil. Based on this, it is suggested that the 74 u fragment may contain the fluorine atom, and the proposed reaction for its formation is:

$$C_4H_3N_2O_2F\ [130u] \longmapsto C_2HNOF\ [74u] + C_2H_2NO\ [56u] \tag{5.4}$$

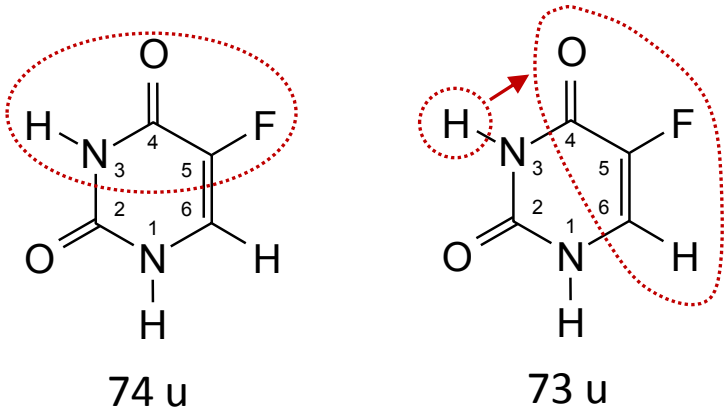

Figure 5.40: Possible configurations of the 74 u and 73 u fragments.

The 73 u fragment, which has a very low abundance and a 1.8 eV lower appearance energy than the 74 u fragment so therefore not formed by hydrogen loss from the 74 u. A possible configuration is shown in Figure 5.40.

5.5.4 64 - 71 u fragmentation processes

The 70 u ion is the most abundant fragment in this group and is possibly due to an energetic fragmentation, (see Section 5.3.4). Possible configurations for this fragment are shown in Figure 5.41. van der Burgt et al. [2014] have suggested the same configurations for the 70 u fragment of thymine ($OCNCO^+$ or $C_2H_2N_2O^+$). It is proposed that the 70 u does not contain the fluorine atom as it is also present in uracil. The two possible fragmentations leading to the configurations in Figure 5.41, both involving the rearrangement of a hydrogen atom, are:

$$C_4H_3N_2O_2F^+ \ [130u] \longmapsto C_2H_2N_2O^+ \ [70u] + C_2HOF \ [60u] \tag{5.5}$$

$$C_4H_3N_2O_2F^+ \ [130u] \longmapsto C_2NO_2^+ \ [70u] + C_2H_3NF \ [60u] \tag{5.6}$$

A possible configuration for the very weak 68 u fragment is also shown in Figure 5.41.

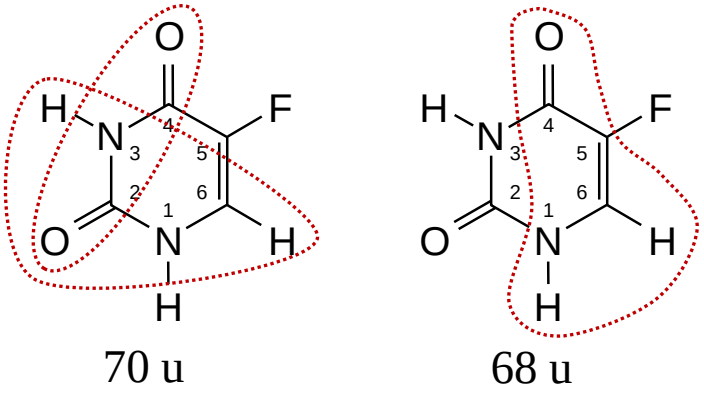

Figure 5.41: Possible configurations of the 70 u and 68 u fragments.

5.5.5 57 - 61 u fragmentation processes

The 58, 59, and 60 u ions are three fragments with high abundance in this group. The 61 u ion could be due to a 5-fluorouracil isotope, although the 61 u:60 u ratio is less than the 131 u:130 u ratio. The 60 u may have derived from a HCN loss from the 87 u ion through C5-C6 bond breakage or alternatively, it may have been formed directly from the parent ion through N3-C4 and C5-C6 bond breakages. For this process, the hydrogen atom would

migrate to bond with the oxygen atom through tautomerization. The loss of a hydrogen atom from the 60 u could give rise to the 59 u fragment. Alternative fragmentation processes that may have formed the 59 u would be: a NH loss to the 74 u, and a C_2O_2NH loss to the 130 u through C4-C5 and N1-C2 bond breakages. The processes are:

$$C_3H_2NOF^+ \ [87u] \longmapsto C_2HOF^+ \ [60u] + HNC \ [27u] \tag{5.7}$$

$$\downarrow$$

$$C_2OF \ [59u] + H \ [1u] \tag{5.8}$$

$$C_3H_2NOF^+ \ [87u] \longmapsto C_2H_2NF^+ \ [59u] + CO \ [28u] \tag{5.9}$$

$$\downarrow$$

$$C_2HNF^+ \ [58u] + H \ [1u] \tag{5.10}$$

$$\downarrow$$

$$C_2NF^+ \ [57u] + H \ [1u] \tag{5.11}$$

Another possible pathway for the production of the 59 u ion is:

$$C_2HNOF \ [74u] \longmapsto C_2OF \ [59u] + HN \ [15u] \tag{5.12}$$

Equation 5.7 shows the loss of a HNC from the 87 u fragment. Equivalent fragmentation pathways for uracil producing the 39 - 41 u ions have been proposed by Jochims et al. [2005] and Rice et al. [1965]. Possible configurations for these fragments are shown in Figure 5.42.

The ion yield curves for this group can be seen in Figure 5.15. The yield ratio between the 59 u:60 u:61 u = 0.42:1:0.032. This is possibly caused by hydrogen rearrangement during fragmentation and/or tautomerization. The appearance energies for the 57 u - 60 u

ions all lie within 1.5 eV of each other, which seems to rule out successive hydrogen loss. These possible fragmentations leading to 59 u are equations 5.8, 5.9 and 5.12, and if all these are relevant then it is not clear why the 59 u:60 u ratio is constant. The 39 - 42 u ions are the equivalent fragments in uracil but the 41 u:42 u ion yield ratio is not constant and the ion yield curves for the 41 u and 42 u have different shapes.

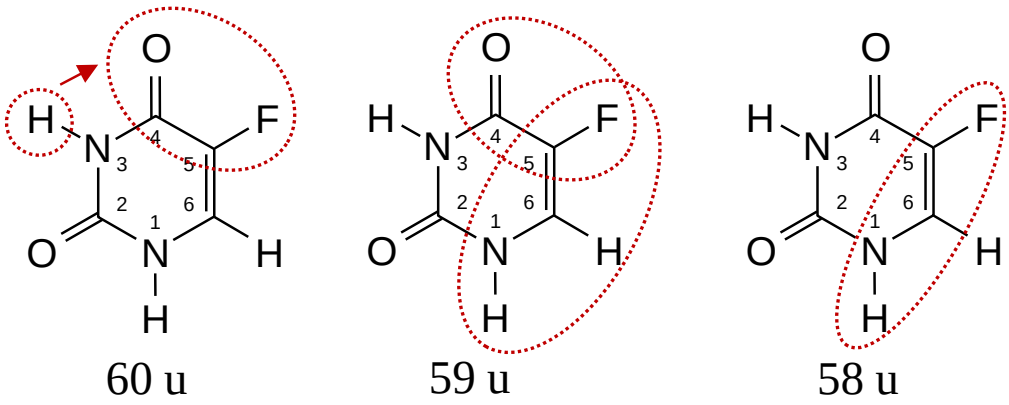

Figure 5.42: Possible configurations of the 60 u, 59 u and 58 u fragments.

5.5.6 50 - 56 u fragmentation processes

The 50 - 56 u fragments create one of the smaller groups in the mass spectrum. The 50 - 56 u fragments all have a very low yield, but the peaks are clearly resolved in the mass spectrum. Figure 5.3 shows that the 50 - 55 u of uracil have very similar yields. This group was not considered by Diskin [2005]. The 56 u fragment in uracil has a higher abundance than the corresponding fragment in 5-fluorouracil. Based on this, we assume that the 50 - 55 u fragments do not contain the fluorine atom, but the 56 u fragment of 5-fluorouracil may contain the fluorine atom. The lower mass fragments have increasingly higher appearance energies, see Figure 5.28. Possible configurations are:

50 u: C_3N^+

51 u: C_3HN^+

52 u: $C_3H_2N^+$, $C_2N_2^+$, C_3O^+

53 u: $C_2HN_2^+$, C_3HO^+

54 u: $C_2H_2N_2^+$, C_2NO^+, $C_3H_2O^+$

55 u: $C_2H_3N_2^+$, C_2HNO^+, $C_3H_3O^+$

56 u: $C_2H_2NO^+$, CN_2O^+ or C_3HF^+

5.5.7 43 - 47 u fragmentation processes

The 43 u peak is broadened due to an energetic fragmentation, and is similar in shape to the 43 u peak in the uracil mass spectrum. The 44 u peak has a higher yield for 5-fluorouracil, indicating that this peak is partly due to a fragment containing the fluorine atom. Fragments 45 - 47 u are present in 5-fluorouracil but not present in uracil. Figure 5.20 shows that the ion yield curves for the 45 - 47 u ions are very similar in shape. The possible configurations are:

43 u: $HNCO^+$

44 u: C_2HF^+, CH_2NO^+

45 u: CNF^+, $C_2H_2F^+$

46 u: $HNCF^+$

47 u: COF^+

$$C_2HNOF^+\ [74u] \longmapsto HCNF^+\ [46u] + CO\ [28u] \tag{5.13}$$

The 44 u is the strongest peak in this group and is may be formed by a HNCO loss from the 87 u through C2-N3 and C4-C5 bond breakages, as seen in Equation 5.14 below. Figure 5.3 shows a peak at 44 u in uracil that is roughly a third of the size of the 44 u of 5-fluorouracil. This may be due to CH_2NO^+ contribution.

$$C_3H_2NOF^+\ [87u] \longmapsto HC_2F^+\ [44u] + HNCO\ [43u] \tag{5.14}$$

The $HNCO^+$ ion (43 u) is present in 5-fluorouracil and uracil with a broadened peak. Equation 5.15 shows HC_2F from to the 87 u ion may be a possible fragmentation pathway producing the 43 u ion.

$$C_3H_2NOF^+\ [87u] \longmapsto HNCO^+\ [43u] + HC_2F\ [44u] \tag{5.15}$$

Other possible fragmentation pathways are:

$$C_2HNOF^+ \ [74u] \longmapsto HNCO^+ \ [43u] + CF \ [31u] \tag{5.16}$$

$$C_2OF^+ \ [59u] \longmapsto C_2F^+ \ [43u] + O \ [16u] \tag{5.17}$$

$$C_2HF^+ \ [44u] \longmapsto C_2F^+ \ [43u] + H \ [1u] \tag{5.18}$$

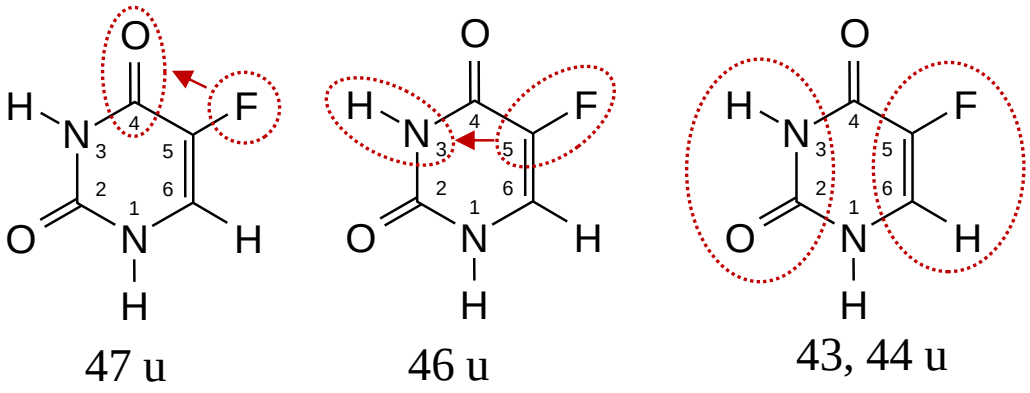

Figure 5.43: Possible configurations of the 47 u, 46 u, 44 u and 43 u fragments.

5.5.8 36 - 41 u fragmentation processes

The 38 - 42 u ions cannot contain the fluorine atom. The 40 u could have derived from N1-C2 and C4-C5 bond breakages accompanied by loss of the fluorine atom. The 38 and 39 u ions may have formed by successive hydrogen loss from the 40 u ion, as seen in Figure 5.44.

Fragments 38 - 42 u have appearance energies of 24.4 ± 0.7 eV, 22.0 ± 0.9 eV, 18.8 ± 0.7 eV, 22.0 ± 0.4 eV and 17.0 ± 0.6 eV respectively. This increase in appearance energies of the smaller fragments implies that the fragmentation processes may involve successive hydrogen loss. Below is a list of possible fragments:

38 u: C_2N^+

39 u: C_2HN^+

40 u: $C_2H_2N^+$, CN_2^+

41 u: $C_2H_3N^+$, CHN_2^+

42 u: $CH_2N_2^+$, CNO^+

Some possible fragmentation pathways are:

$$C_2OF^+ \ [59u] \longmapsto C_2O \ [40u] + F \ [19u] \tag{5.19}$$

$$C_2H_2NF^+ \ [59u] \longmapsto C_2H_2N \ [40u] + F \ [19u] \tag{5.20}$$

$$C_2HNF^+ \ [58u] \longmapsto C_2HN \ [39u] + F \ [19u] \tag{5.21}$$

$$C_2NF^+ \ [57u] \longmapsto C_2N \ [38u] + F \ [19u] \tag{5.22}$$

An alternative fragmentation producing the 38 u ion is:

$$C_3H_2NF^+ \ [87u] \longmapsto C_3H_2^+ \ [38u] + NOF \ [42u] \tag{5.23}$$

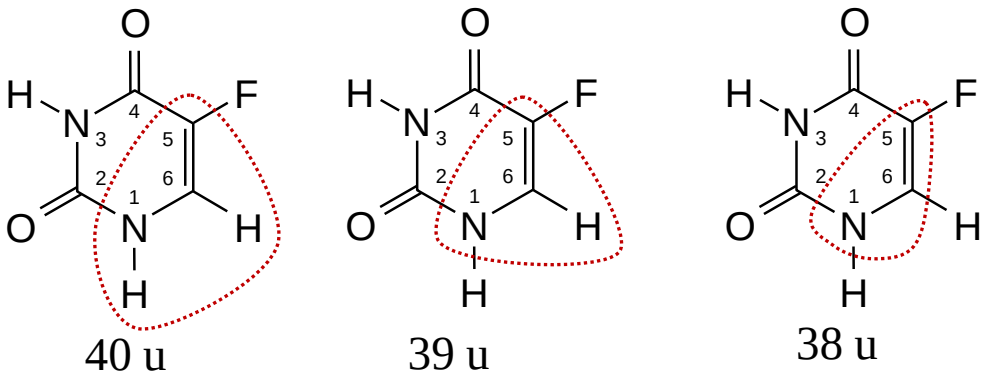

Figure 5.44: Possible configurations of the 40 u, 39 u and 38 u fragments.

5.5.9 24 - 34 u fragmentation processes

None of these fragments can contain the fluorine atom, and the only possible assignments are:

24 u: C_2^+

25 u: C_2H^+

26 u: $C_2H_2^+$, CN^+

27 u: HCN^+

28 u: $HNCH^+$, CO^+

29 u: $HNCH_2^+$

The 32 u fragment may have formed from the carbon atom in the 5^{th} position and the fluorine atom, with a hydrogen atom migrating and bonding to the carbon atom. The 31 u and 32 u ions are likely CF^+ and CHF^+ respectively. The 31 u peak is broader than the 32 u peak, indicating that a more energetic fragmentation is responsible for the production of the 31 u ion.

The appearance energies for the 31 u and 32 u ions are 18.0 $\pm$ 1.4 eV and 16.6 $\pm$ 0.4 eV respectively. The 31 u indicates a prominent fragmentation, its appearance energy is lower than the corresponding 13 u fragment in uracil (both of low abundance). Fragments 27 - 24 u have progressively higher appearance energies. Equations 5.24 and 5.25 show two possible configurations of the 28 u ion. The 28 u ion has the lowest appearance energy in this group at 13.8 $\pm$ 0.7 eV (in uracil, the 29 u ion has a lower appearance energy than the 28 u ion). Possible fragmentation pathways producing the 28 u ion are:

$$C_3H_2NOF\ [87u] \longmapsto HNCH^+\ [28u] + FC_2O\ [59u] \tag{5.24}$$

$$C_2HNOF\ [74u] \longmapsto CO^+\ [28u] + HNCF\ [46u] \tag{5.25}$$

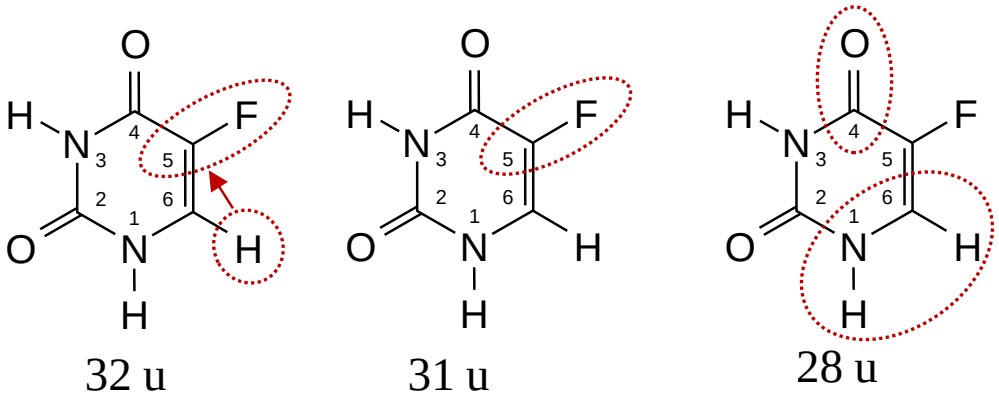

Figure 5.45: Possible configurations of the 32 u, 31 u and 28 u fragments.

5.5.10 12 - 15 u fragmentation processes

None of these fragments can contain the fluorine atom and the only possible assignments are:

12 u: C^+

13 u: CH^+

14 u: CH_2^+, N^+

15 u: NH^+

Multiple possible fragmentation pathways are expected to exist for these fragments, but we only observe a second onset for the 15 u ion.

Chapter 6

Conclusion

The main objective of this experiment was to study low-energy electron impact induced ionisation and fragmentation of 5-fluorouracil. We have measured mass spectra of positive ions for electron impact on 5-fluorouracil, with electron energies ranging from 5.71 to 101.01 eV in steps of 0.25 eV. A beam of 5-fluorouracil was generated by a resistively heated oven mounted in an expansion chamber, and the forward section of the beam effusing from a capillary in the oven passed through a skimmer into the collision chamber, where the beam was crossed by a pulsed electron beam (0.5 μs, 8 kHz). Ions have been mass resolved and detected using a reflectron time-of-flight mass spectrometer. LabVIEW based data acquisition techniques have been used to accumulate mass spectra as a function of electron impact energy.

By fitting groups of adjacent peaks in the mass spectra with sequences of normalized Gaussians, we have obtained ion yield curves, and have determined appearance energies for most positive fragment ions of 5-fluorouracil.

Some of the main fragmentation pathways of 5-fluorouracil are similar to uracil. The 87 u ion is $C_3H_2NOF^+$ formed by HNCO loss. This fragmentation is similar to the loss of HNCO from uracil producing $C_3H_3NO^+$ (69 u). Comparison of the mass spectra of 5-fluorouracil and uracil strongly suggest that the fragmentations producing the 57 - 60 u group of peaks in 5-fluorouracil are the same as those producing the 39 - 42 u group of peaks in uracil. Based on this, we attribute the 57 - 60 u ions to HCN loss from 87 u and to CO loss from 87 u, accompanied by the possible loss of one or two additional hydrogen atoms. In the mass spectra of both 5-fluorouracil and uracil 28 u is the most prominent

peak, attributed to both $HCNH^+$ and CO^+. In 5-fluorouracil, one of the possible pathways producing $HCNH^+$ is FCCO loss from 87 u.

We have identified several fragmentations that are unique to 5-fluorouracil. The most prominent fragmentation produces CF^+ at 31 u. Because this fragmentation becomes prominent above 40 eV we do not think that this fragmentation is relevant for explaining the radiosensitizing properties of 5-fluorouracil. DEA with production of radicals is the more likely explanation. Other fragmentations that are unique to 5-fluorouracil produce peaks at 74 u (C_2HNOF^+), 47 u (COF^+), 46 u ($HCNF^+$), and 32 u (CHF^+).

There are several small groups of peaks for which we have obtained ion yield curves and appearance energies. The 50-56 u group of fragments have similar relative yields in the mass spectra of 5-fluorouracil and of uracil, suggesting that these fragments do not contain the fluorine atom, and that the fragmentation pathways are similar for 5-fluorouracil and uracil. The 38 - 44 u group of fragments is likely produced by several different fragmentation processes.

We have observed several half-integer peaks in two groups in the mass spectra. The 64 - 72 u group contain half integer peaks at 69.5 u and 70.5 u. The 41 - 47 u group contain half-integer peaks at 41.5 u, 42.5 u, 43.5 u and 44.5 u. The half-integer peaks at 69.5 u and 70.5 u have been interpreted as broadening of the 70 u peak due to an energetic fragmentation. It is unlikely that these peaks are due to doubly-charged fragments because these are above m/q = 65 u, of the doubly-charged parent. The half-integer peaks at 41.5 u, 42.5 u, 43.5 u and 44.5 could be due to doubly-ionised fragments, but could also possibly be attributed to broadening of the integer peaks related to energetic fragmentations.

The appearance energies of a number of 5-fluorouracil fragments obtained in this experiment were compared with appearance energies of fragments from similar molecules (uracil, 5-chlorouracil, 6-chlorouracil and 5-bromouracil) obtained by other research groups. Our results are in good agreement (see Table 5.1) with the uracil results of Diskin [2015] and the results for 5- and 6-chlorouracil of Denifl et al. [2004b].

Understanding the appearance energies gives information regarding the fragmentation processes of 5-fluorouracil induced by electron impact. Understanding of dissociation

mechanisms on the microscopic scale are of vital importance to the enhancement of radiosensitizers, as the risks involved with biological tissue interacting with high-energy radiation are great and need to be comprehensively understood in order to make radiation therapy safer. The results obtained in this experiment give new insight into the fragmentation pathways for 5-fluorouracil that are initiated by electron impact.

Bibliography

H. Abdoul-Carime, M. A. Huels, F. Brüning, E. Illenberger, and L. Sanche. "dissociative electron attachment to gas-phase 5-bromouracil". *The Journal of Chemical Physics*, 113(7):2517–2521, 2000.

H. Abdoul-Carime, M. A. Huels, E. Illenberger, and L. Sanche. "formation of negative ions from gas phase halo-uracils by low-energy (0–18 ev) electron impact". *International Journal of Mass Spectrometry*, 228(2):703–716, 2003.

R. Abouaf, J. Pommier, and H. Dunet. "negative ions in thymine and 5-bromouracil produced by low energy electrons". *International Journal of Mass Spectrometry*, 226 (3):397–403, 2003a.

R. Abouaf, J. Pommier, and H. Dunet. "electronic and vibrational excitation in gas phase thymine and 5-bromouracil by electron impact". *Chemical Physics Letters*, 381(3): 486–494, 2003b.

R. Abouafa and H. Dunet. "structures in dissociative electron attachment cross-sections in thymine, uracil and halouracils". *The European Physical Journal*, 35:405–410, 2005.

V. V. Afrosimov, A. A. Basalaev, O. S. Vasyutinskii, M. N. Panov, and O. V. Smirnov. "fragmentation of uracil after electron capture by doubly charged ions". *The European Physical Journal D*, 69(1):3, 2015.

A. N. Agnihotri, S. Kasthurirangan, S. Nandi, A. Kumar, C. Champion, H. Lekadir, J. Hanssen, P. F. Weck, M. E. Galassi, R. D. Rivarola, O. Fojón, and L. C. Tribedi. "absolute total ionization cross sections of uracil (c 4 h 4 n 2 o 2) in collisions with mev energy highly charged carbon, oxygen and fluorine ions". *Journal of Physics B: Atomic, Molecular and Optical Physics*, 46(18):185201, 2013.

E. Alizadeh, T. M. Orlando, and L. Sanche. "biomolecular damage induced by ionizing radiation: The direct and indirect effects of low-energy electrons on dna". *Annual Review of Physical Chemistry*, 66(1):379–398, 2015.

. Arian Kriesch Akriesch. "penning trap". URL <https://commons.wikimedia.org/wiki/File:PenningTrap.svg>.

I. Baccarelli, I. Bald, F. A. Gianturco, E. Illenberger, and J. Kopyra. "electron-induced damage of dna and its components: Experiments and theoretical models". *Physics Reports*, 508(1):1–44, 2011a.

I. Baccarelli, I. Bald, F. A. Gianturco, E. Illenberger, and J. Kopyra. "electron-induced damage of dna and its components: Experiments and theoretical models". *Physics Reports*, 508(1):1–44, 2011b.

J. Ball, A. Moore, and S. Turner. *"Ball and Moore's Essential Physics for Radiographers"*. Wiley, 2012.

R. Balog, J. Langer, S. Gohlke, M. Stano, H. Abdoul-Carime, and E. Illenberger. "low energy electron driven reactions in free and bound molecules: from unimolecular processes in the gas phase to complex reactions in a condensed environment". *International Journal of Mass Spectrometry*, 233(1):267–291, 2004.

B. Barc, M. Ryszka, J. Spurrell, M. Dampc, P. Limão-Vieira, R. Parajuli, N. J. Mason, and S. Eden. "multi-photon ionization and fragmentation of uracil: Neutral excited-state ring opening and hydration effects". *The Journal of Chemical Physics*, 139(24):244311, 2013.

G. Barrett. "development of an apparatus for the study of electron impact fragmentation of molecular clusters", 2008.

Bio. "dna sructure versus rna structure". URL <http://ib.bioninja.com.au/-Media/dna-vs-rna-structure-med.jpeg>.

U. Boesl. "time-of-flight mass spectrometry: Introduction to the basics". *Mass Spectrometry Reviews*, 36(1):86–109, 2016.

C. Dass. *"Fundamentals of Contemporary Mass Spectrometry"*. Wiley Series on Mass Spectrometry. Wiley, 2007. ISBN 9780470118481.

E. de Hoffmann and V. Stroobant. *"Mass Spectrometry: Principles and Applications"*. Wiley, 2013.

S. Denifl, S. Matejcik, B. Gstir, G. Hanel, M. Probst, P. Scheier, and T. Mark. "electron attachment to 5-chloro uracil". *Journal of Chemical Physics*, 118:4107–4114, 2003.

S. Denifl, S. Matejcik, S. Ptasinska, B. Gstir, M. Probst, P. Scheier, E. Illenberger, and T. D. Mark. "electron attachment to chlorouracil: A comparison between 6-clu and 5-clu". *The Journal of Chemical Physics*, 120(2):704–709, 2004a.

S. Denifl, S. Ptasińska, B. Gstir, P. Scheier, and T. Märk. "electron impact ionization of 5- and 6-chlorouracil: appearance energies". *International Journal of Mass Spectrometry*, 232(2):99–105, 2004b.

S. Denifl, B. Sonnweber, G. Hanel, P. Scheier, and T. D. Märk. "threshold electron impact ionization studies of uracil". *International Journal of Mass Spectrometry*, 238:47–53, 2004c.

O. Desouky and G. Zhou. "biophysical and radiobiological aspects of heavy charged particles". *Journal of Taibah University for Science*, 10(2):187–194, 2016. The First International Conference on Radiation Physics and Its Applications.

S. Diskin. "study of low energy electron-impact induced ionization and fragmentation of uracil", 2015.

H. Ehrhardt and L. Morgan. *"Electron Collisions with Molecules, Clusters, and Surfaces"*. Physics of Atoms and Molecules. Springer US, 2013.

G. Eitel, M. Block, A. Czasch, M. Dworschak, S. George, O. Jagutzki, J. Ketelaer, J. Ketter, S. Nagy, D. Rodriguez, C. Smorra, and K. Blaum. "position-sensitive ion detection in precision penning trap mass spectrometry". *Nuclear Instruments and Methods in Physics Research*, pages 475–483, 2008.

F. Ferreira da Silva, D. Almeida, R. Antunes, G. Martins, Y. Nunes, S. Eden, G. Garcia, and P. Limao-Vieira. "electron transfer processes in potassium collisions with 5-fluorouracil and 5-chlorouracil". *Phys. Chem. Chem. Phys.*, 13:21621–21629, 2011.

G. García Gómez-Tejedor and M. Fuss. *"Radiation Damage in Biomolecular Systems"*. Biological and Medical Physics, Biomedical Engineering. Springer Netherlands, 2012.

J. Gross and P. Roepstorff. *"Mass Spectrometry: A Textbook"*. Springer Berlin Heidelberg, 2nd edition, 2011.

R. Hassan. "mass spectrometry (importance and uses)". *Pharmaceutica Analytica Acta*, 3(10), 2012.

M. Herve du Penhoat, M. Huels, P. Cloutier, J. Jay-Gerin, and L. Sanche. "anion fragment formation in 5-halouracil films induced by 1-20 ev electron impact". *J. Phys. Chem. B*, 108:17251–17260, 2004.

D. Holland, A. Potts, L. Karlsson, I. Zaytseva, A. Trofimov, and J. Schirmer. A study of the valence shell electronic structure of the 5-halouracils. *Chemical Physics*, 352(1): 205 – 216, 2008.

H. Hotop, M.-W. Rul, and I. I. Fabrikant. "resonance and threshold phenomena in low-energy electron collisions with molecules and clusters". *Physica Scripta*, 2004(T110): 22, 2004.

M. Imhoff, Z. Deng, and M. A. Huels. "ionizing fragmentation of uracil and 5-bromouracil by electron impact in gas phase and hyperthermal ar+ ion irradiation in condensed phase". *International Journal of Mass Spectrometry*, 262(1):154–160, 2007.

Y. Itikawa and N. Mason. "cross sections for electron collisions with water molecules". *Journal of Physical and Chemical reference data*, 34(1):1–22, 2005.

E. Itälä, D. Ha, K. Kooser, E. Rachlew, M. Huels, and E. Kukk. "fragmentation patterns of core-ionized thymine and 5-bromouracil". *The Journal of Chemical Physics*, 133, 2010.

E. Itälä, D. Ha, K. Kooser, E. Rachlew, E. Nõmmiste, U. Joost, and E. Kukk. "molecular fragmentation of pyrimidine derivatives following site-selective carbon core ionization". *Journal of Electron Spectroscopy and Related Phenomena*, 184:119–124, 2011.

H. Jochims, M. Schwell, H. Baumgartel, and S. Leach. "photoion mass spectrometry of adenine, thymine and uracil in the 6–22 ev photon energy range". *Chemical Physics*, 314:263–282, 2005.

S. Maclot, D. G. Piekarski, R. Delaunay, A. Domaracka, A. Méry, V. Vizcaino, J.-Y. Chesnel, F. Martín, M. Alcamí, B. A. Huber, L. Adoui, P. Rousseau, and S. Díaz-Tendero. "stability of the glycine cation in the gas phase after interaction with multiply charged ions". *The European Physical Journal D*, 68(6):149, 2014.

B. Mamyrin. "time-of-flight mass spectrometry (concepts, achievements, and prospects)". *International Journal of Mass Spectrometry*, 206:251–266, 2001.

R. March and J. Todd. *"Practical Aspects of Ion Trap Mass Spectrometry: Chemical, Environmental, and Biomedical Applications"*. Number v. 3. Taylor & Francis, 1995.

R. March and J. Todd. *"Quadrupole Ion Trap Mass Spectrometry"*, volume 165. Wiley-Interscience, 2005.

N. Markova, V. Enchev, and I. Timtcheva. "oxo-hydroxy tautomerism of 5-fluorouracil: Water-assisted proton transfer". *J. Phys. Chem.*, 109 (9):1981–1988, 2005.

P. Markush, P. Bolognesi, A. Cartoni, P. Rousseau, S. Maclot, R. Delaunay, A. Domaracka, J. Kocisek, M. C. Castrovilli, B. A. Huber, and L. Avaldi. "the role of the environment in the ion induced fragmentation of uracil". *Phys. Chem. Chem. Phys.*, 18:16721–16729, 2016.

J. McConkey, C. Malone, P. Johnson, C. Winstead, V. McKoy, and I. Kanik. "electron impact dissociation of oxygen-containing molecules–a critical review". *Physics Reports*, 466(1–3):1–103, 2008.

U. National Human Genome Research Institute. "the structure of a biological cell". URL <http://www.accessexcellence.org/RC/VL/GG/nhgri_PDFs/chromosome.pdf>.

Pinimg. "three-dimensional quadrupole ion trap". URL <https://s-media-cache-ak0.pinimg.com/736x/87/82/4e/87824e3d5342071e9ee94213d1591bcb--mass-spectrometry-chemistry.jpg>.

T. C. H. Project. "nude bayard-alpert ion gauges covering the vacuum range 1x10^{-3}mbar to 3x10^{-11}mbar", a. URL <http://arunmicro.com/abd//wp-content/gallery/uhv-gauges/AIG17GR1.jpg>.

T. C. H. Project. “quadrupole mass spectrometer”, b. URL <http://www.tissuegroup.chem.vt.edu/chem-ed/ms/graphics/quad-sch.gif>.

D. Radisic, Y. J. Ko, J. M. Nilles, S. T. Stokes, M. D. Sevilla, J. Rak, and K. H. Bowen. “photoelectron spectroscopic studies of 5-halouracil anions”. *The Journal of Chemical Physics*, 134(1):015101, 2011.

M. Rahman and E. Krishnakumar. “absolute partial and total electron ionization cross sections of uracil”. *International Journal of Mass Spectrometry*, 392:145–153, 2015.

J. M. Rice, G. O. Dudek, and M. Barber. “mass spectra of nucleic acid derivatives. pyrimidines”. *Journal of the American Chemical Society*, 87(20):4569–4576, 1965.

L. Sanche. “low energy electron-driven damage in biomolecules”. *The European Physical Journal D*, 35:367–390, 2005.

L. Sanche, B. Boudaiffa, P. Cloutier, D. Hunting, and M. Huels. “resonant formation of dna strand breaks by low-energy (3 to 20 ev) electrons”. *Science*, 287:1658–1660, 2000.

A. M. Scheer, K. Aflatooni, G. A. Gallup, and P. D. Burrow. “bond breaking and temporary anion states in uracil and halouracils: Implications for the dna bases”. *Phys. Rev. Lett.*, 92:068102, Feb 2004.

D. Skoog, F. Holler, and S. Crouch. *“Principles of Instrumental Analysis”*. Cengage Learning, 2017.

R. E. Smalley. “discovering the fullerenes”. *Rev. Mod. Phys.*, 69:723–730, 1997.

G. Stein and A. Pardee. *“Cell Cycle and Growth Control: Biomolecular Regulation and Cancer”*. Wiley, 2004.

J. Ulrich, R. Teoule, R. Massot, and A. Cornu. “etude de la fragmentation de derives de l’uracile et de la thymine par spectrometrie de masse”. *Organic Mass Spectrometry*, 2 (12):1183–1199, 1969.

P. J. van der Burgt, F. Mahon, G. Barrett, and M. L. Gradziel. “electron impact fragmentation of thymine: partial ionization cross sections for positive fragments”. *The European Physical Journal D*, 68(6):151, 2014.

P. J. M. van der Burgt. “electron impact fragmentation of cytosine: partial ionization cross sections for positive fragments”. *The European Physical Journal D*, 68(5):135, 2014.

P. J. M. van der Burgt, S. Finnegan, and S. Eden. “electron impact fragmentation of adenine: partial ionization cross sections for positive fragments”. *The European Physical Journal D*, 69(7):173, 2015.

W. C. Wiley and I. H. McLaren. Time-of-flight mass spectrometer with improved resolution. *Review of Scientific Instruments*, 26(12):1150–1157, 1955.

C. Winstead and V. McKoy. “low-energy electron collisions with gas-phase uracil”. *The Journal of Chemical Physics*, 125(17):174304, 2006.

F. Xiao, Y. Zheng, P. Cloutier, Y. He, D. Hunting, and L. Sanche. “on the role of low-energy electrons in radiosensitization of dna by gold nanoparticles”. *Nanotechnology*, 22, 2011.

Appendix A

Image of the code used in python to generate Figure 5.4.

```
import matplotlib.pyplot as plt
from matplotlib import cm
import numpy as np
from mpl_toolkits.mplot3d import Axes3D
import matplotlib.colors as colors
import pandas as pd

def ionYield():

    f= 'C:\\Users\\Administrator\\Desktop\\ION YIELD\\zvals2.txt'

    zvals2 = pd.read_csv(f,delimiter='\t',header=None)
    zvals2 = zvals2.as_matrix()
    np.shape(zvals2)

    f= 'C:\\Users\\Administrator\\Desktop\\ION YIELD\\data2.txt'
    data2 = pd.read_csv(f,delimiter='\t',header=None)
    data2 = data2.as_matrix()
    colvals = data2[:,0]
    rowvals = data2[0,:]
    rowvals = rowvals[1:]
    colvals = colvals[1:]

    X,Y = np.meshgrid(colvals,rowvals)

    fig = plt.figure()

    plt.title('Airy Pattern Scan')
    ax1 = fig.gca(projection='3d')

    ax1.set_xlabel('m/q [u]')
    ax1.set_ylabel('Electron Energy [eV]')
```